공학박사학위논문

Fabrication of Pt-Based Electro-Catalyst for Polymer Electrolyte Membrane Fuel Cell via Electroless Deposition and Sonochemical Method

무전해 도금 및 초음파 방법을 이용한

고분자 전해질 막 연료 전지용 백금계 촉매의 제작

2013년 2월

서울대학교 대학원

화학생물공학부

최 인 수

Fabrication of Pt-Based Electro-Catalyst for Polymer Electrolyte Membrane Fuel Cell via Electroless Deposition and Sonochemical Method

무전해 도금 및 초음파 방법을 이용한 고분자 전해질 막 연료 전지용 백금계 촉매의 제작

지도교수 김 재 정

이 논문을 공학박사 학위논문으로 제출함
2012 년 11 월

서울대학교 대학원
화학생물공학부
최 인 수

최인수의 공학박사 학위논문을 인준함
2012 년 12 월

위 원 장 _____ (인)

부위원장 _____ (인)

위 원 _____ (인)

위 원 _____ (인)

위 원 _____ (인)

Abstract

Insoo Choi

School of Chemical and Biological Engineering

The Graduate School of Engineering

Seoul National University

High over-potential, induced by the irreversibility of oxygen reduction reaction (ORR) in polymer electrolyte membrane fuel cell (PEMFC), causes low cell performance. In order to increase the kinetics of ORR, Pt_{shell}-Pd_{core}/C electro-catalyst was synthesized with a consecutive procedure; electroless deposition (ELD) and galvanic displacement reaction. Cu ELD was applied to form Cu ad-layer on carbon-supported Pd catalyst, which was followed by the displacement of Cu by Pt. The spectroscopic methods, such as XRD and XPS were used to characterize as-prepared Pt_{shell}-Pd_{core}/C catalyst. ICP mass analysis showed that the catalyst contained 7% and 15% of Pt and Pd in atomic weight, respectively. The core-shell structure was confirmed by the intense analysis with HR-TEM and STEM-HAADF, equipped with EDS. The three-electrode electrochemical analysis revealed that the four-electron oxygen reduction occurred on Pt_{shell}-Pd_{core}/C with higher kinetic current than conventional Pt/C. The enhanced kinetic of ORR was closely related to the surface-binding property of Pt over-layer in Pt_{shell}-Pd_{core}/C. The local density of state in d-band of Pt over-layer at

adsorbate state was up-shifted compared to Pt/C with respect to the Fermi level. The d-band center, ε_d of Pt_{shell}-Pd_{core}/C was measured by XPS, higher than Pt/C by 0.33 eV. The high-lying ε_d tended to bind OH less strongly, and consequently the oxygen-containing species (Pt-O) was hydrogenated and easily desorbed out of surface. Moreover, the mass-specific activity of Pt_{shell}-Pd_{core}/C was about five times higher than Pt/C toward ORR. The method helped the synthesis of highly dispersed Pt-based electro-catalyst with small Pt content.

Speaking of the anodic reaction in direct methanol fuel cell (DMFC), a type of PEMFC, stable and CO_{ad}-tolerant anode catalyst has been in a great need. For the sense, Pt_{shell}-Pd_{core}/C catalyst was applied for the MeOH oxidation reaction (MOR). Both Pt_{shell}-Pd_{core}/C and Pt/C were active for the MOR, but showed different behavior according to the reaction potential. The apparent activation energy (E_{app}) was calculated from the Arrhenius plots to compare the kinetics of MOR on both Pt_{shell}-Pd_{core}/C and Pt/C. At lower potential, the E_{app} of Pt_{shell}-Pd_{core}/C was greater than the E_{app} of Pt/C. The result indicated that Pt_{shell}-Pd_{core}/C was less active in dissociating MeOH than Pt/C. At more positive potential region, however, Pt_{shell}-Pd_{core}/C showed smaller E_{app} than Pt/C. The decrease in E_{app} in this region meant that the kinetic in the formation of OH_{ad} and in the combination reaction were improved by Pt_{shell}-Pd_{core}/C. The enhanced kinetic of OH_{ad} formation on Pt_{shell}-Pd_{core}/C critically contributed to the overall reaction with more extent, since the rate-determining step (RDS) in MOR was

not the adsorption of MeOH, but rather the electro-oxidation of adsorbed species. The electrochemical oxidation of adsorbed CO on Pt_{shell}-Pd_{core}/C and Pt/C was performed by CO_{ad}-stripping experiment. On-set potential for CO_{ad} desorption on Pt_{shell}-Pd_{core}/C was more negative than on Pt/C, indicating that that OH_{ad} was more readily formed on Pt_{shell}-Pd_{core}/C surface than on Pt/C. From the measured current density, it was concluded that the commercial Pt was more susceptible to adsorption of CO, leading to easy CO_{ad}-poisoning and deactivation compared to Pt_{shell}-Pd_{core}/C.

The ultrasound was applied to fabricate the electro-catalyst for fuel cell. The direct deposition of Pt nanoparticles on the surface of SiO_2 without surface modification was attempted by irradiating ultrasound (Pt-SiO_2). This method enabled the formation of Pt nanoparticles with a narrow-sized distribution. The composites were blended with conducting carbon (Pt-SiO_2/C), and applied as an anode catalyst for PEMFC. With various anode relative humidity, the membrane fabricated with Pt-SiO_2/C exhibited a tolerance toward water-deficient condition showing sustainable performance, while the membrane with Pt/C degraded sharply. This was attributed to the hydrophilic property of SiO_2, which retained the moderate hydration level in the membrane even under low humidity.

keywords: Pt-based electro-catalyst, electroless deposition, ultrasound, silica, oxygen reduction, methanol electro-oxidation, low humidity

Student Number: 2009-30251

Contents

List of Tables

List of Figures

CHAPTER I

Introduction

1-1. Fuel Cell Basics

Continued reliance on the limited fossil fuels poses serious environmental and energy-supply challenges. Globally, a direct combustion of the fossil fuels for generating electric powers and heats releases significant amount of greenhouse gases (CO_2, NO_x), and holds a remarkable portion of atmospheric pollution [1-3]. Moreover, as being said, the deposit of the fossil fuels is limited and their shortage in the near future has been warned. Even with the advanced technology for reducing the emission of pollutant and for increasing fuel-to-energy conversion efficiency, the energy use and relevant problems will last. For this sense, there needs to be more principal resolution; the development of alternative fuel and a new power system. A variety of alternative fuels and devices has been proposed to help future environmental and energy crisis. Among them, fuel cell is viewed as a near-term-use power source.

Fuel cell is considered as a continuous energy conversion device with input of fuel, and output of reaction product with electric current. In common H_2-O_2 fuel cell system, hydrogen gas is fed into anode and oxygen gas to cathode (Fig. 1-1). The electric current is generated by the electron transfer through the oxidation of hydrogen gas, and the reduction of oxygen gas along with formation of water. Since bonding configuration of water molecule is lower than the

boding energy of the reactants, the energy difference is released as heat and current, but mostly current (Fig. 1-2) [4-6].

Fuel cell possesses lots of advantages over the conventional combustion engines. First of all, fuel cell produces electricity directly from chemical energy, and thus its theoretical efficiency approaches to 60%, which is far above than the combustion engines' (< 30%, Fig. 1-3) [3,4,7,8]. Secondly, fuel cell operates via electro-oxidation of hydrogen gas from anode and produces only water [9]. Therefore, undesirable products and emissions are almost zero. Lastly, it produces electricity as long as it is supplied with hydrogen. The hydrogen gas can be produced by the electrolysis of water, or by reforming hydrocarbons, which means fuel cell has more fuel availability than the combustion engines. On the other hand, fuel cell has some serious disadvantages [4]. High cost in production is a major barrier of the commercialization of the fuel cell. Fuel storage is another issue of fuel cell. Hydrogen gas is combustible and difficult to handle. In addition to those, operational temperature compatibility and durability under stop-and-start cycling are the limitations of the fuel cell.

There are various types of fuel cells as shown in Fig. 1-4 [3,4,8-11]. The fuel cells are divided into the six categories; alkaline fuel cell (AFC), polymer electrolyte membrane or proton exchange membrane fuel cell (PEMFC), direct methanol fuel cell (DMFC), phosphoric acid fuel cell (PAFC), molten carbonate fuel cell (MCFC), and solid oxide fuel cell (SOFC). They are classified according to the charge carriers, the type of electrolyte, and the operating temperature. Each fuel cell can also be distinguished by the purpose of use and their specifications, such as

the volumetric/gravimetric power density demand, and the operating temperature. MCFC and SOFC are suitable to industry and power plant. AFC and PAFC can be used in stationary power for house and buildings. PEMFC and DMFC are suitable for transportation and mobile applications.

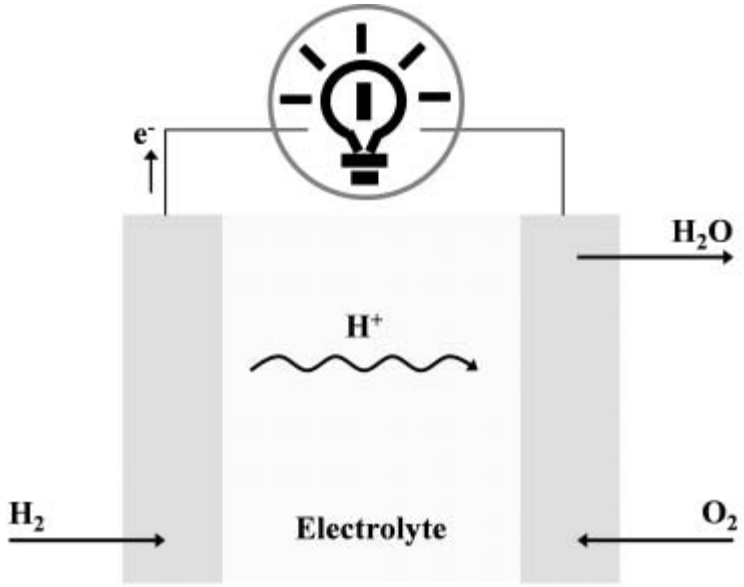

Fig. 1-1. A simple structure of fuel cell in H_2-O_2 system.

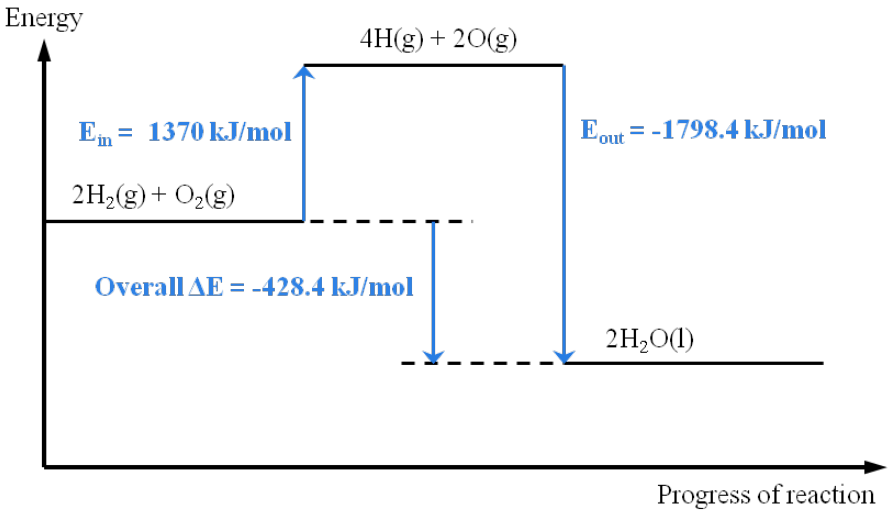

Fig. 1-2. Energy diagram of H_2-O_2 combustion reaction (adapted from [5]).

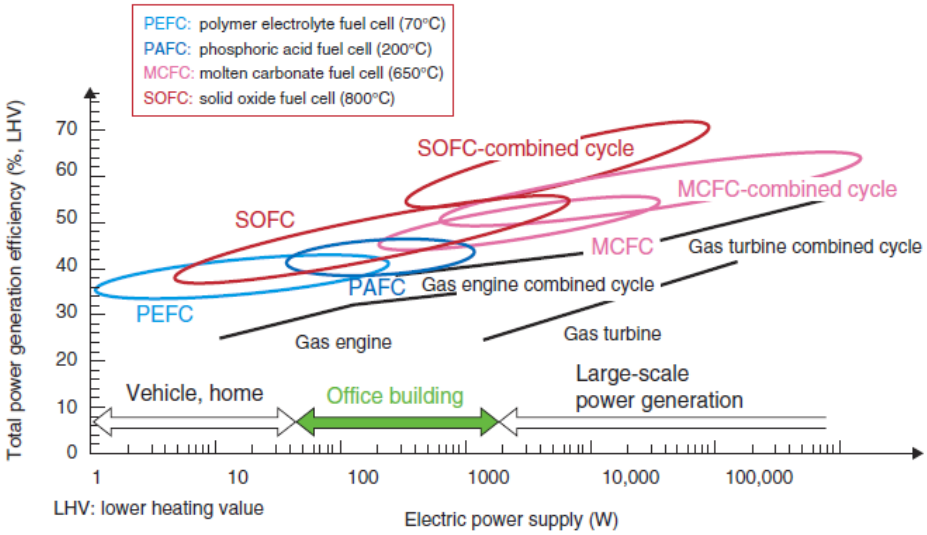

Fig. 1-3. Comparison of the fuel efficiency of various types of fuel cells and other power devices [7].

Fuel Cell Technologies

Fuel Cell Type		Electrolyte	Operating Temperature	Electrical Efficiency	Fuel Oxidant	Energy Output
AFC	Alkaline Fuel Cell	Potassium hydroxide solution	Room temperature to 90°C	60-to-70%	H^2 O^2	300W-to-5KW
PEMFC	Proton Exchange Membrane Fuel Cell	Proton Exchange Membrane	Room temperature to 80°C	40-to-60%	H^2 O^2, Air	1KW
DMFC	Direct Methanol Fuel Cell	Proton Exchange Membrane	Room temperature to 130°C	20-to-30%	CH^3 OH , O^2 Air	1KW
PAFC	Phosphoric Acid Fuel Cell	Phosphoric Acid	160-to-220°C	55%	Natural gas, bio gas, H^2 O^2, Air	200KW
MCFC	Molten Carbonate Fuel Cell	Molten mixture of alkali metal carbonates	6200-to-660°C	65%	Natural gas, bio gas, coal gas, H^2 O^2, Air	2MW-to-100MW
SOFC	Solid Oxide Fuel Cell	Oxide ion conducting ceramic	800-to-1000°C	60-to-65%	Natural gas, bio gas, coal gas, H^2 O^2, Air	100KW

Source: h-tec, SAE International

Fig. 1-4. The detailed specification of various types of fuel cells in terms of electrolyte, operating condition, electrical efficiency, fuel oxidant, and energy output [10].

1-2. Polymer Electrolyte Membrane Fuel Cell (PEMFC)

PEMFC, also known as proton exchange membrane fuel cell, has received a great attention because of its availability as a power source for various applications [4,12]. One of the unique features of PEMFC is that it uses a solid membrane through which proton moves. Such membrane is highly proton-conductive, so that it is able to run PEMFC at quite low temperature. The operating potential of PEMFC is comprised by the difference in thermodynamic redox potential of anode and cathode, electro-oxidation of hydrogen (0.0 V *vs*. standard hydrogen electrode, SHE) and reduction of oxygen (1.2 V *vs*. SHE), respectively. Therefore, theoretically PEMFC can generate 1.2 V of operating potential at most. The value is relatively high compared to other types of fuel cell. The precise electrode reaction of PEMFC will be discussed later in this chapter. Another feature of PEMFC is its compactness, which, in turns, makes it applicable to the power source for portable electronic devices. The compactness is regarded as the most powerful potential of PEMFC, because other types of fuel cell mainly function for massive industrial purposes, such as combined heat and power (CHP) system [9]. Recent years have witnessed lots of progression in developing the performance of PEMFC. However, there are still many drawbacks to be corrected and resolved. Specifically, high cost of production and durability problem are the prime barriers for PEMFC to get into commercial market entry. In that sense, current fuel cell technology covers highly varied fields, which extends from the available materials and their fabrication, particularly electro-catalysts, to the expensive new

concepts to sustain and even further renovate previous achievement.

Fig. 1-5 shows a structure of PEMFC in detail [13]. PEMFC consists of two separators, one for anode and the other for cathode. Between each separator, there is a membrane electrode assembly (MEA). The MEA is made up of a gas diffusion layer (GDL), a catalyst layer, and a polymer membrane. The GDL is porous material, which distributes reactant gases (H_2, O_2) and removes product gases (H_2O). The electrochemical reactions occur on the surface of the catalyst, and electric current is produced. The polymer membrane in PEMFC is sulphonated polytetrafluoroethylene (PTFE) which has hydrophilic side chain within hydrophobic backbone. The polymer membrane is subject to conduct protons, and to transport water molecule. The commonly available polymer membrane is Nafion™ from Dupont. Both electrodes are suppressed by metal bipolar plates for a close packing.

The fuel cell is an electrochemical cell and each electrochemical reaction is characterized by the Nernst equation (Eq. 1-A). When current flows, a deviation of the potential from the equilibrium occurs, where the deviation is called over-potential, η. The relationship between the over-potential and the subsequent change of current density of a redox reaction is given by the Butler-Volmer relation (Eq. 1-B).

(Eq. 1-A) $$For\ O + ne^- \rightleftharpoons R, \quad E = E^0 + \frac{RT}{nF}\ ln\frac{C_O^*}{C_R^*}$$

(Eq. 1-B) $$j = j_0[exp\left(\frac{\alpha_a nF\eta}{RT}\right) - exp\left(-\frac{\alpha_c nF\eta}{RT}\right)]$$

There are several types over-potentials according to which limiting factors are involved. Generally, charge transfer over-potential (or activation over-potential, η_{act}), mass transfer over-potential (η_{mt}) and ohmic over-potential (η_{ohm}) exist in real system. Slow charge transfer steps in electro-catalytic reactions contribute to the activation over-potential. The reactants with slow feed rate or low solubility are limited by diffusion, migration, and convection, thus they cannot reach the electrode. This type of limitation causes mass transfer over-potential. At last, the ohmic over-potential arises from the ionic resistance of electrolyte membrane. During the operation of fuel cell, the over-potentials were applied to both anode and cathode. Therefore, each half-cell potential was always lower than their thermodynamic equilibrium potentials (Eq. 1-C). The open circuit potential (OCP) of single-cell can be expressed by following equation (Eq. 1-D).

(Eq. 1-C) $$E_a = E_a^0 - \eta_{act,a} - \eta_{mt,a}$$

$$E_c = E_c^0 - \eta_{act,c} - \eta_{mt,c}$$

(Eq. 1-D) $$E_{OCP} = E_a + E_c - E_{electrolyte}$$

$$= (E_a^0 + E_c^0) - (\eta_{act,a} + \eta_{act,c}) - (\eta_{mt,a} + \eta_{mt,c}) - \eta_{ohm}$$

For PEMFC, where H_2-O_2 system is adopted, the cell potential is comprised of the sum of half-cell potentials from hydrogen oxidation reaction (HOR) and oxygen reduction reaction (ORR) of anode and cathode, respectively. The kinetics of HOR is very fast, and it is normally

controlled by mass transfer. The oxidation of hydrogen involves the adsorption of hydrogen gas on the surface of catalyst, which is followed by the dissociation reaction (Eq. 1-E). Once the hydrogen molecule is split to hydrogen atom, the proton is formed via electrochemical reaction over the catalyst (Eq. 1-F).

(Reaction on Platinum, Pt)

(Eq. 1-E) $2Pt^{o} + H_2 \rightarrow Pt - H_{ad} + Pt - H_{ad}$

(Eq. 1-F) $Pt - H_{ad} \rightarrow H^+ + e^- + Pt^{o}$

(Eq. 1-G) $2H^+ + 2e^- \rightarrow H_2 \qquad E^0 = 0.0\ \mathrm{V}\ vs.\ \mathrm{NHE}$

ORR proceeds generally by two pathways in aqueous electrolyte; direct four-electron reduction and two-electron reduction or peroxide intermediate reduction [15-17]. The detail reaction pathways are given below (Eq. 1-H ~ Eq. 1-K). Compared to hydrogen oxidation, the oxygen reduction is more complex and sluggish owing to strong O-O bonding (D^{o}_{298} = 498 kJ/mol) [18]. For this reason, the direct reduction of molecular oxygen to water readily takes place over only highly active metal, like Pt. While, on Pd which is less active than Pt, peroxide is the final reduction product via two-electron reduction (D^{o}_{298} = 213 kJ/mol).

Direct four-electron pathway (acid and alkaline solutions)

(Eq. 1-H) $O_2 + 4H^+ + 4e^- \rightarrow 2H_2O \qquad E^0 = 1.229\ \mathrm{V}\ vs.\ \mathrm{NHE}$

(Eq. 1-I) $O_2 + 2H_2O + 4e^- \rightarrow 4OH^-$ $E^0 = 0.401\ \text{V}\ vs.\ \text{NHE}$

Peroxide pathway (in acid solutions)

(Eq. 1-J) $O_2 + 2H^+ + 2e^- \rightarrow H_2O_2$ $E^0 = 0.67\ \text{V}\ vs.\ \text{NHE}$

$H_2O_2 + 2H^+ + 2e^- \rightarrow 2H_2O$ $E^0 = 1.77\ \text{V}\ vs.\ \text{NHE}$

Peroxide pathway (in alkaline solutions)

(Eq. 1-K) $O_2 + H_2O + 2e^- \rightarrow HO_2^- + OH^-$ $E^0 = -0.065\ \text{V}\ vs.\ \text{NHE}$

$HO_2^- + H_2O + 2e^- \rightarrow 3OH^-$ $E^0 = 0.867\ vs.\ \text{NHE}$

The sluggish kinetics of ORR is represented by small exchange current density and high over-potential on cathode. As seen in Table 1-1 [4,19,20], the exchange current density for ORR is about 10^{-11}~10^{-10} A/cm^2. However, the oxidation of hydrogen is facile with relatively large exchange current density. The kinetic parameter given in the table shows up to five orders of magnitude between for HOR and ORR. The ORR over-potential is in the range of 300 ~ 400 mV, while the HOR over-potential is only tenth of mV. Therefore, the departure of operating potential of PEMFC from the thermodynamically reversible value is mainly due to the ORR rather than HOR. The ORR is irreversible even on Pt surface, because the oxygen reduction takes place at high anodic potential under extremely corrosive environment (pH < 1). Therefore, there has been a great need to develop the more efficient and durable electro-catalysts to accelerate ORR. The most promising way was to make the electro-catalyst in bi-metallic system.

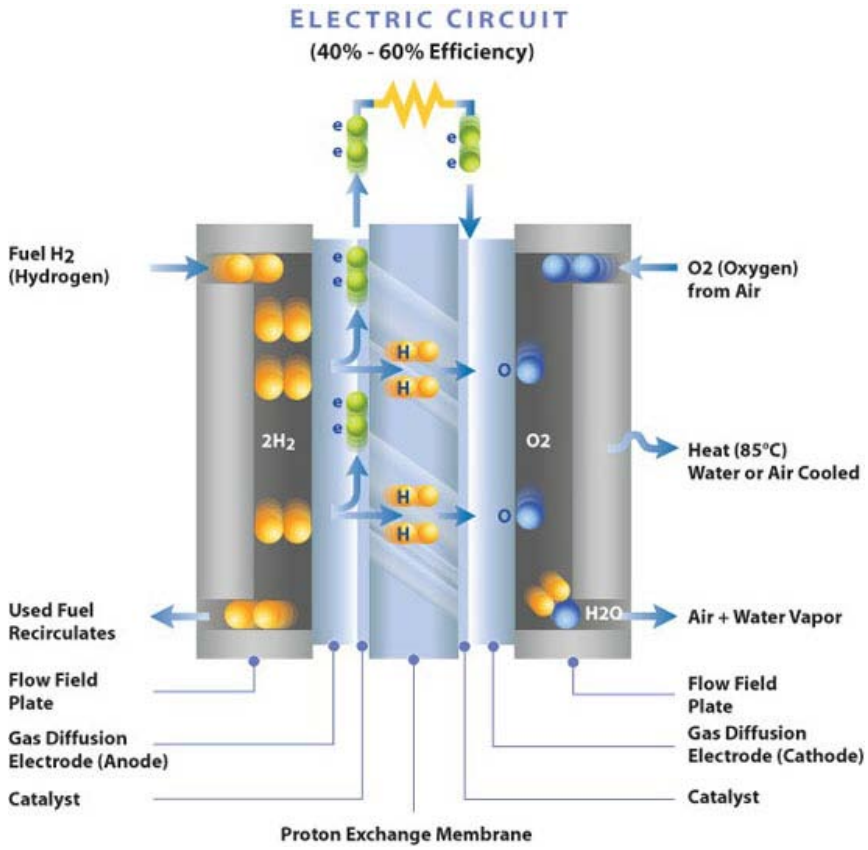

Fig. 1-5. Detail structure and operation of PEMFC [14].

.

Table 1-1 Exchange Current Densities for (a) HOR and (b) ORR on Various Metal Surfaces (values are normalized per real unit surface area of metal) [4,19,20]

(a)

Surface	Electrolyte	j_0(A/cm^2)
Pt	Acid	10^{-3}
Pt	Alkaline	10^{-4}
Pd	Acid	10^{-4}
Rh	Alkaline	10^{-4}
Ir	Acid	10^{-4}
Ni	Alkaline	10^{-4}
Ni	Acid	10^{-5}
Ag	Acid	10^{-5}
W	Acid	10^{-5}
Au	Acid	10^{-6}
Fe	Acid	10^{-6}
Mo	Acid	10^{-7}
Ta	Acid	10^{-7}
Sn	Acid	10^{-8}
Al	Acid	10^{-10}
Cd	Acid	10^{-12}
Hg	Acid	10^{-12}

(b)

Surface	Electrolyte	j_0(A/cm^2)
Metal surfaces in acid electrolyte		
Pt	Acid	10^{-9}
Pd	Acid	10^{-10}
Ir	Acid	10^{-11}
Rh	Acid	10^{-11}
Au	Alkaline	10^{-11}
Pt Alloy in PEMFC		
Pt-C	Nafion	3×10^{-9}
PtMn-C	Nafion	6×10^{-9}
PtCr-C	Nafion	9×10^{-9}
PtFe-C	Nafion	7×10^{-9}
PtCo-C	Nafion	6×10^{-9}
PtNi-C	Nafion	5×10^{-9}

1-3. Electro-Catalyst in Bi-Metallic Systems for ORR

To the present, pure Pt is regarded as the most efficient catalyst for the fuel cell reaction. However, high price and low abundance of Pt allow its limited use. Pt-based alloy catalysts are, therefore, designated as promising catalyst for the fuel cell application. These alloys can provide electrochemical stability and reduce Pt content simultaneously [1,21]. Generally one (bi-metallic) or more (ternary-metallic) 3d-/4d- transition metals are alloyed with Pt. Especially in bi-metallic catalyst, the foreign transition metal gives a promoting effect such as by catalyzing one of the elemental reactions or by prohibiting unwanted reaction. The nature of the surface metal-metal bond in bi-metallic alloys has been previously studied by J.A. Rodriguez [22]. The perturbation in the electronic structure of the alloys could be induced by the charge transfer from one metal (foreign metal) to the other metal (host metal). It leads to the changes in the chemical properties of the alloys, especially from the host metal perspective. Besides, the change in metal-metal bond length is derived by alloying (lattice contraction), thus it affects the binding property of the host metal with reactants. This behavior is completely different with what has been observed in bulk metal [23-25].

When Pt is alloyed with foreign transition metal, such as Ni, Co via co-reduction of corresponding precursor solution, we observe low surface composition of Pt. It is attributed to the high reduction potential of Pt compared to the other transition metals. Indeed, the discrepancy between surface and bulk compositions in alloys are closely related to the reduction

priority of metal precursors [26], the surface energy of each metal component [27], and the interaction with various adsorbing species [28]. Low Pt surface concentration results in low catalytic activity because of reduced electrochemical surface area (ECSA). Therefore, it is required to segregate Pt to the surface. Since this segregation behavior was caused by the interaction between two metals, it was believed that the segregation could enhance or suppress electro-catalytic activity of bi-metal electro-catalysts. Numerous theoretical studies have been carried out to elucidate the tendency of Pt-based alloys toward surface segregation [27,29-36]. Along with the density functional theory (DFT), the first-principle calculation was used to investigate the trend in segregation energies in transition metals including Pt. By doing so, the surface phase diagram, from surface energy as a function of the surface composition and the calculated heat of segregation, was constructed [32]. Surface segregation of metal is significantly important in catalysis in fuel cell, because it rules catalytic activity of electro-catalysts, especially fuel oxidation on anode and ORR on cathode [37,38].

A variety method was used to achieve this; high temperature annealing [30,35-38] or chemical leaching of less noble metal [39-43]. However, even with the heat treatment, complete Pt coverage of alloy metal was not easily fulfilled. For this reason, the electrochemical deposition technique; i.e. under-potential deposition, has been suggested and applied to the synthesis of Pt-based alloy with high Pt surface concentration [44-54]. These catalysts consisted of monolayer of Pt on carbon-supported metal or metal-alloy nanoparticles. We could expect the highest utilization of Pt, since most Pt located in the outer surface, and participated in the catalytic

reactions. Because of their unique structure, these catalysts were referred as Pt monolayer (Pt_{ML}) electro-catalyst [50]. Pt_{ML} electro-catalyst with various cores were designed and synthesized for the fuel cell reaction, and most of them exhibited excellent activities and stabilities [44-54]. The interaction between surface Pt and the substrate became a hot issue and draw lots of attentions. The relevant studies were performed accordingly, and demonstrated the synergetic effect of the interaction in Pt_{ML} electro-catalyst for ORR.

The change in the catalytic activity of the transition metals with periodic order, and bi-metallic catalyst with respect to the surface catalysis was explained by Norskov and co-workers [55-61]. Norskov proposed that the d-band center (ε_d), an indicator of density of states (DOS) from Fermi level (ε_F), could represent the reactivity of metal. In bi-metallic catalyst, the surface Pt atom experiences a strain; compressive or tensile, when it contacts with foreign metal due to the difference in atomic radius. Because of the strain, ε_d shifts upward or downward with respect to ε_F. The movement of ε_d reflects the change in the catalytic activity. DFT calculations have shown that the binding energies and the reactivity of small adsorbates have a great correlation with the position of ε_d on the strained surface and the metal over-layers [59-62]. In Norskov's d-band model, the simplest quantum-mechanical one-electron description was assumed to explain the interaction of adsorbed molecule with the metal surface [61]. Fig. 1-6 depicts a typical DOS for a transition metal [61]. It shows a broad s-band with half-filled (all transition metal has one s electron), and a much narrower d-band. The occupancy of d-bands varies according to the transition metals as they shift through the ε_F. The narrow d-band is a result of a small coupling

matrix element (V_{dd}) between localized d states. What is more important is that the band width is proportional to the V_{dd} [63]. Since the d-bands are narrow, the interaction of the d-band state with the adsorbates generates a bonding and anti-bonding. Fig. 1-7 describes the local DOS at an adsorbate in two limiting cases [61]. The case 'a' corresponds to the interaction of adsorbate with a broad s band of metal, and the case 'b' is representative of the interaction with the d-electrons of metal (d band). The broad band limit with a single resonance is often called 'weak chemisorption', whereas the split of bonding and anti-bonding state is called 'strong chemisorption' [64]. If the total volume of d-band is fixed, d-band becomes narrow and thus, ε_d shifts upward above the ε_F to maintain the filling status. In this case, the anti-bonding level appears above ε_F. The empty anti-bonding state binds the adsorbate strongly, and the bond strength becomes large with a degree of un-filled status of anti-bonding. Inversely, if ε_d moves downward below the ε_F, and the anti-bonding state becomes filled with decreased bond strength. This general principle is well illustrated in Fig. 1-8 [61].

The ORR can occur only when dissolved oxygen molecules diffuse and adsorb on metal surfaces whether it is dissociative or associative adsorption. Therefore, the reactivity of metal for ORR is closely related with the adsorption state of oxygen-containing species such as O, OH, and OOH. Fig. 1-9 is the typical DOS projected to one of the O_2 2p for chemisorbed oxygen on metal [61]. Valence 2p states of gas-phase atomic oxygen interact with the metal s electrons, giving rise to a broadening into a single resonance. All these 2p-projected DOS of oxygen are well below ε_F and hence, completely filled. The coupling of these normalized states with the d-

band of metal gives rise to a splitting of the oxygen resonance in two as discussed; bonding of the adsorbate and the metal d-states, and anti-bonding above ε_F. The coupling behavior and its extent are different with surface metals, therefore, d-states and surface reactivity toward oxygen adsorption change. As already explained the strained metal over-layer shows different d-states with bulk metal. The strain gives a rise to a change in orbital overlap. The over-layer metal contacting with larger lattice experiences a tensile strain and the overlapping of d-band decreases, leading to up-shift of ε_d (high-lying ε_d). Accordingly, the un-filled state of d-band increases, thus the surface metal binds oxygen-containing species strongly during ORR (high chemisorptions energy, Fig. 1-10) [61]. With smaller lattice, however, there exists a compressive strain between over-layer metal and the substrate. Under compressive strain, the overlapping increases resulting in down-shift of ε_d (low-lying ε_d) and weak binding (weak chemisorptions energy). The ε_d shift induced by surface strain is described in Fig. 1-11. In ORR kinetics, the reaction is limited either by the dissociation of O_2 for the metal surface that binds oxygen too strongly, or by the proton transfer to adsorbed O for the metal weakly binding with oxygen. Therefore, the kinetic model of ORR has volcano-shape dependence (Sabatier's principle) as seen in Fig. 1-12 [65]. The measured kinetic current density from ORR was plotted as a function of the calculated oxygen adsorption energy, ΔE_O (all data were shown relative to Pt). The experimental data were marked by circles (Pt_{ML} supported on single-crystal metal electrodes), diamonds (polycrystalline alloys annealed in ultrahigh vacuum before immersion in the electrochemical cell), and crosses (bulk $Pt_3Ni(111)$ alloys annealed in ultrahigh vacuum before

immersion). The dashed lines were the theoretical predictions. It shows that the most active electro-catalyst for ORR should be designed to have a moderate binding ability with adsorbed oxygen. By the way, it was predicted that the Pt over-layers, binding atomic oxygen little too stronger than bulk Pt does, would exhibit the highest reactivity (Fig. 1-13) [46,66,67]. Table 1-2 shows the shifts in ε_d of the surface impurities and the over-layers (including Pt) relative to the clean bulk metals in bi-metallic electro-catalyst system [55]. The impurity/over-layer atoms are listed horizontally and the host entries are listed vertically. Two numbers are listed for each combination. The first is for the isolated surface impurity and the second is for the over-layer. The surfaces are assumed to be the most closely packed and the over-layer structures are pseudomorphic. The trend in a d-band shift is well presented, and it provides the combinations in designing electro-catalyst not only for ORR but other fuel cell reactions.

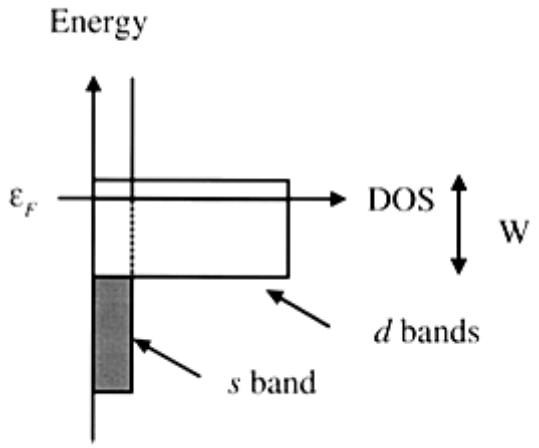

Fig. 1-6. Schematic illustration of the density of states (DOS) of a transition metal, showing the broad s band and the narrow d bands (width W) around ε_F [61].

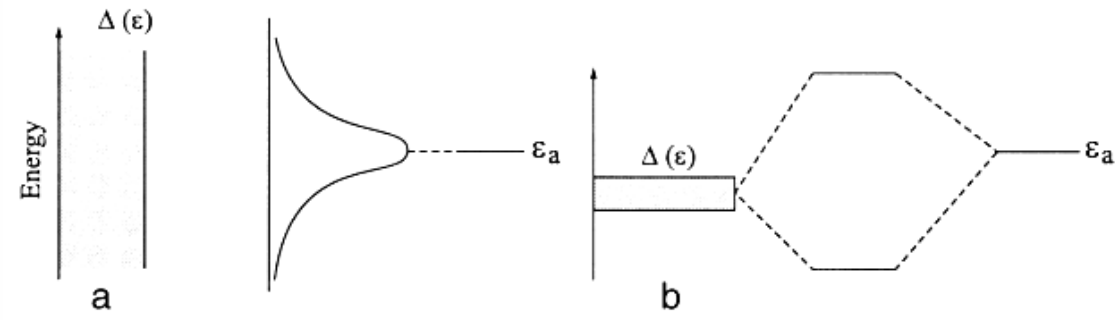

Fig. 1-7. The local DOS at an adsorbate in two limiting cases; (a) for a broad surface band (s band) and (b) for a narrow metal band (d band), where ε_a refers the energy state of adsorbate [61].

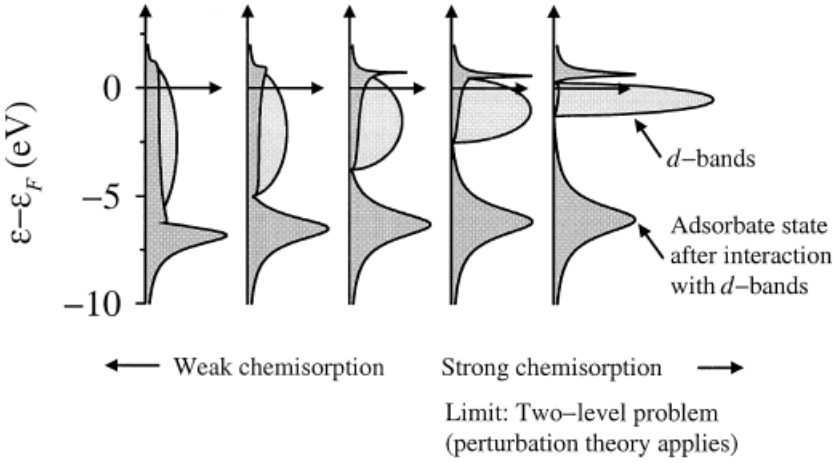

Fig. 1-8. The local DOS projected onto an adsorbate state interacting with the d bands at a surface [61].

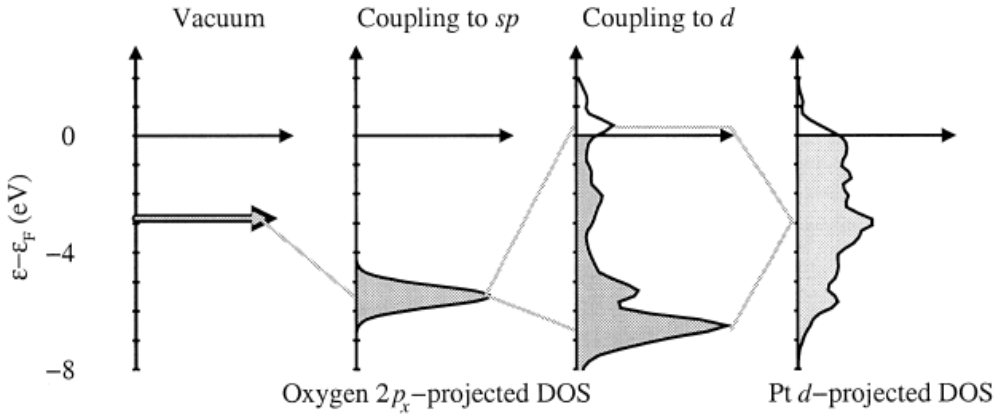

Fig. 1-9. Schematic illustration of the change in local electronic structure at an oxygen atom upon adsorption on simple and transition/noble metal surfaces [61].

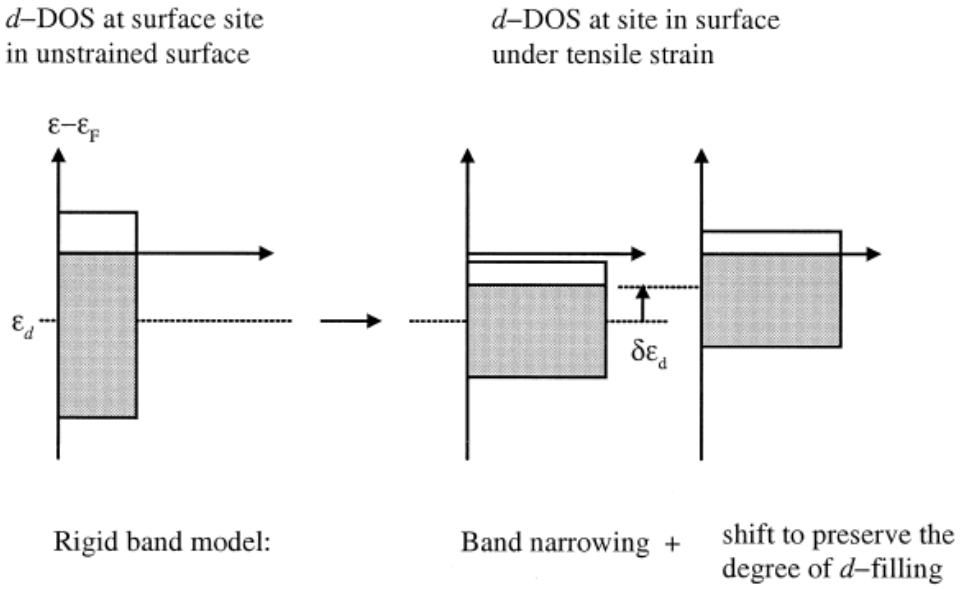

Fig. 1-10. Illustration of the effect of tensile strain on ε_d, where $\delta\varepsilon_d$ is the shift of ε_d [61].

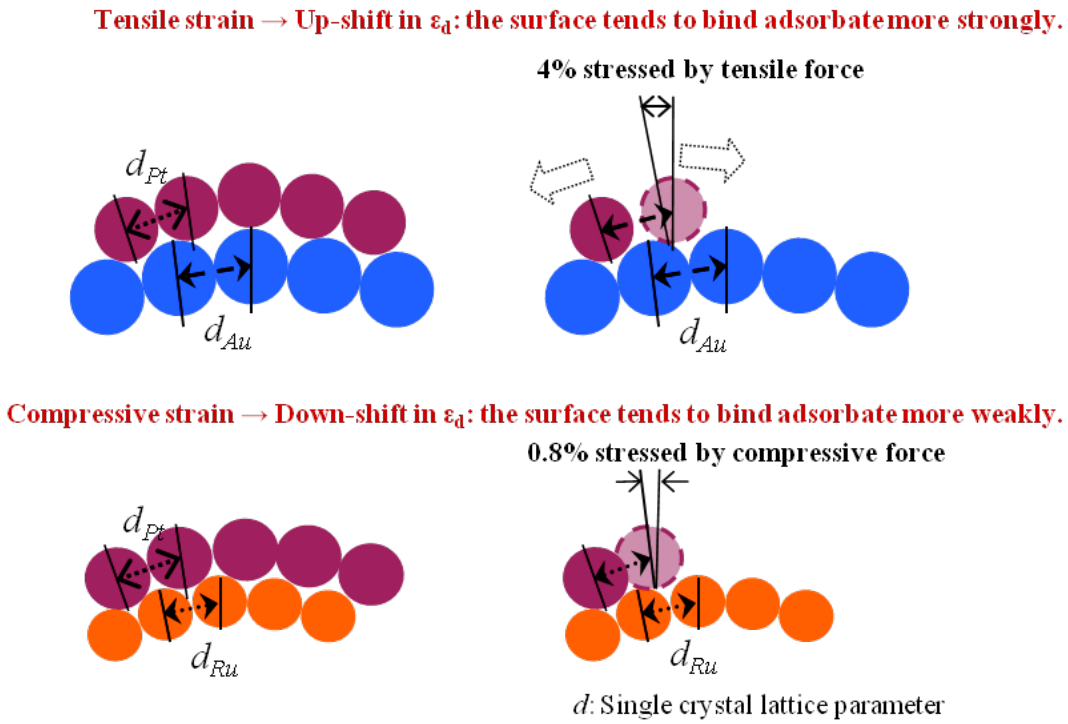

Fig. 1-11. Strain effect on catalytic activity of noble metal in Pt-based transition metal alloys.

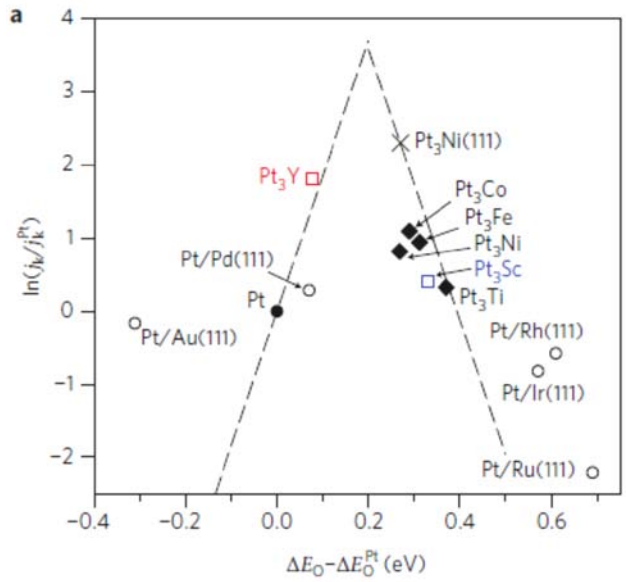

Fig. 1-12. Volcano plots and free-energy diagrams for the ORR on Pt-based transition metal alloys [65].

(a)

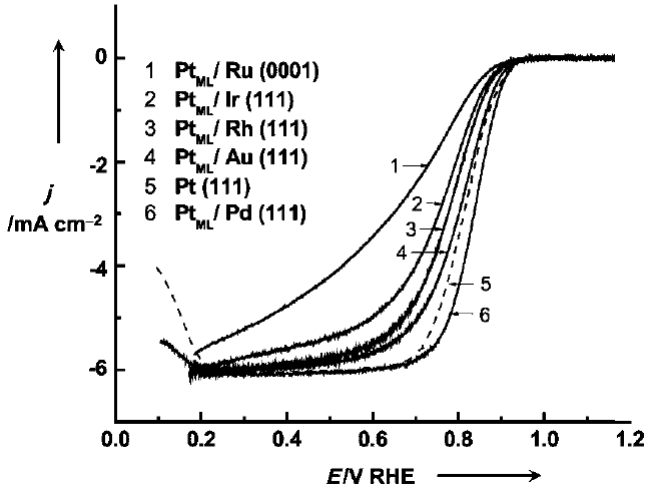

(b)

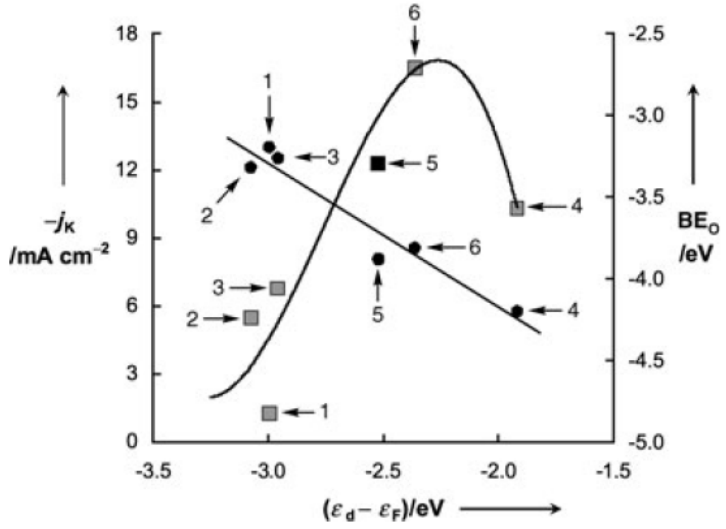

Fig. 1-13. (a) polarization curves for ORR on Pt_{ML} on various transition metals, and (b) the kinetic currents (j_k) from (a) and the calculated binding energies of atomic oxygen (BE_O) plotted as a function of ($\varepsilon_d - \varepsilon_F$)

Table 1-2. Shifts in d-band Centers of Surface Impurities and Over-layers (horizontal array) Relative to the Clean Metal (vertical array) Values (all values are in eV) [55]

	Fe	Co	Ni	Cu	Ru	Rh	Pd	Ag	Ir	Pt	Au
Fe	*−0.92*	0.05	−0.20	−0.13	−0.29	−0.54	−1.24	−0.83	−0.36	−1.09	−1.42
		0.14	−0.04	−0.05	−0.73	−0.72	−1.32	−1.25	−0.95	−1.48	−2.19
Co	0.01	*−1.17*	−0.28	−0.16	−0.24	−0.58	−1.37	−0.91	−0.36	−1.19	−1.56
	−0.01		−0.20	−0.06	−0.70	−0.95	−1.65	−1.36	−1.09	−1.89	−2.39
Ni	0.09	0.19	*−1.29*	0.19	−0.14	−0.31	−0.97	−0.53	−0.14	−0.80	−1.13
	0.96	0.11		0.12	−0.63	−0.74	−1.32	−1.14	−0.86	−1.53	−2.10
Cu	0.56	0.60	0.27	*−2.67*	0.58	0.32	−0.64	−0.70	0.58	−0.33	−1.09
	0.25	0.38	0.18		−0.22	−0.27	−1.04	−1.21	−0.32	−1.15	−1.96
Ru	0.21	0.26	0.01	0.12	*−1.41*	−0.17	−0.82	−0.27	0.02	−0.62	−0.84
	0.30	0.37	0.29	0.30		−0.12	−0.47	−0.40	−0.13	−0.61	−0.86
Rh	0.24	0.34	0.16	0.44	0.04	*−1.73*	−0.54	0.07	0.17	−0.35	−0.49
	0.31	0.41	0.34	0.22	0.03		−0.39	−0.08	0.03	−0.45	−0.57
Pd	0.37	0.54	0.50	0.94	0.24	0.36	*−1.83*	0.59	0.53	0.19	0.17
	0.36	0.54	0.54	0.80	−0.11	0.25		0.15	0.31	0.04	−0.14
Ag	0.72	0.84	0.67	0.47	0.84	0.86	0.14	*−4.30*	1.14	0.50	−0.15
	0.55	0.74	0.68	0.62	0.50	0.67	0.27		0.80	0.37	−0.21
Ir	0.21	0.27	0.05	0.21	0.09	−0.15	−0.73	−0.13	*−2.11*	−0.56	−0.74
	0.33	0.40	0.33	0.56	−0.01	−0.03	−0.42	−0.09		−0.49	−0.59
Pt	0.33	0.48	0.40	0.72	0.14	0.23	−0.17	0.44	0.38	*−2.25*	−0.05
	0.35	0.53	0.54	0.78	0.12	0.24	0.02	0.19	0.29		−0.08
Au	0.63	0.77	0.63	0.55	0.70	0.75	0.17	0.21	0.98	0.46	*−3.56*
	0.53	0.74	0.71	0.70	0.47	0.67	0.35	0.12	0.79	0.43	

1-4. Electroless Deposition of Metal

Electroless deposition (ELD) is defined as the formation of thin metal film on the substrate by the exchange of electrons between metal ion and reducing agent through electrochemical reduction and oxidation process [68]. In general, the electrolyte for ELD contains a metal precursor, a reducing agent, a complexing agent, and a pH adjuster. The mechanism of ELD is expressed with the following equations (from Eq. 1-L to Eq. 1-N), and depicted in Fig. 1-14.

Anode reaction: $R^{o} \rightarrow R^{n+} + ne^{-}$ (Eq. 1-L)

Cathode reaction: $ML_{m}^{n+} + ne^{-} \rightarrow M + mL$ (Eq. 1-M)

Overall reaction: $R^{o} + ML_{m}^{n+} \rightarrow M + mL + R^{n+}$ (Eq. 1-N)

The anodic process corresponds to the oxidation of reducing agent on the surface of catalyst, and the cathode reaction is the reduction of metal ions. Palladium (Pd) is the most widely used catalyst in the ELD. Once Pd is adsorbed the substrate, it oxidizes a reducing agent providing electrons to the metal ion. Ultimately metal film is formed on the substrate. Even though the reaction of ELD of metal can be equated above, the principle of such process has not been fully understood. The theoretical basis for the ELD stems from the mixed potential theory [69-71], which is described in Fig. 1-15. The mixed potential is the potential of the electrode, where the total anodic current balances with the total cathodic current. In other word, the potential results

from the simultaneous occurrence of oxidation and reduction process with zero net current.

Since the reaction is triggered by the oxidation of reducing agent, no external current supply is required. Unfortunately, the existence of reducing agent with metal precursor delivered a negative effect, which is the homogeneous formation of metal particle. If the homogeneous reaction is dominant, the electrolyte becomes unstable. Therefore, the stability of the electrolyte should be prioritized by controlling the composition of the electrolyte precisely, such as pH and the concentration of reducing agent. ELD takes place on the catalyzed surface as mentioned previously. Therefore, it is also called an autocatalytic chemical reaction, in which the deposited metal on the substrate acts as a catalyst or an activator. There are a few metals that fit into this category, such as Cu, Ag, Pd, and Pt. However, the autocatalytic reaction is governed by the combination of metal and reducing agent. For example, in hypophosphate-based electrolyte, Cu does not catalyze the reaction. Hydrazine or formaldehyde is more suitable for ELD of Cu. Some common reducing agent for ELD is given in Table 1-3.

ELD has been investigated mostly in semiconductor process, such as the formation of thin seed layer for subsequent metal film growth or trench filling, and the corrosion prevention. However, people recently applied this technique for preparing electro-catalyst [72-76]. Beard et al. [72] synthesized Pt-Rh/C catalyst for fuel cell application by ELD of Pt on the Rh-seeded carbon surface using dimethylamine borane (DMAB) as a reducing agent. Using this method, the preparation of highly dispersed metal catalyst was fulfilled. Schaal et al. [73] prepared Ag-Pt/SiO_2 by ELD of Ag using HCHO as a reducing agent. The reduction did not occur on bare

SiO_2 surface, while it was catalyzed on Pt/SiO_2. Therefore, ELD could be a viable method to prepare electro-catalyst for fuel cell.

In this study, the ELD was applied along with galvanic displacement reaction for preparing Pt-based electro-catalyst with a core-shell structure. Instead of electrodeposition, electroless deposition of Cu was attempted to make Cu ad-layer on core metal. Cu ad-layer was displaced by Pt afterward. Pd was chosen to be a core metal because of the two reasons. First, Pd is one of the activators for ELD of Cu, and formaldehyde is catalyzed by Pd and Cu. Therefore, it is possible to make Cu ad-layer on the surface of Pd nanoparticle selectively via ELD. Upon the process Pt_{shell}-Pd_{core} combination was achieved. Secondly, it was already reported that Pt over-layer on Pd exhibited higher activity toward ORR than pure Pt catalyst [46]. For these reasons, ELD of Cu was selected as an intermediate step of the overall process. Pt-Pd shell-core structure could also be accomplished by direct ELD of Pt over Pd core. However, ELD of Pt may induce homogeneous reduction of Pt on the carbon support as well as on Pd, which is not a desired process.

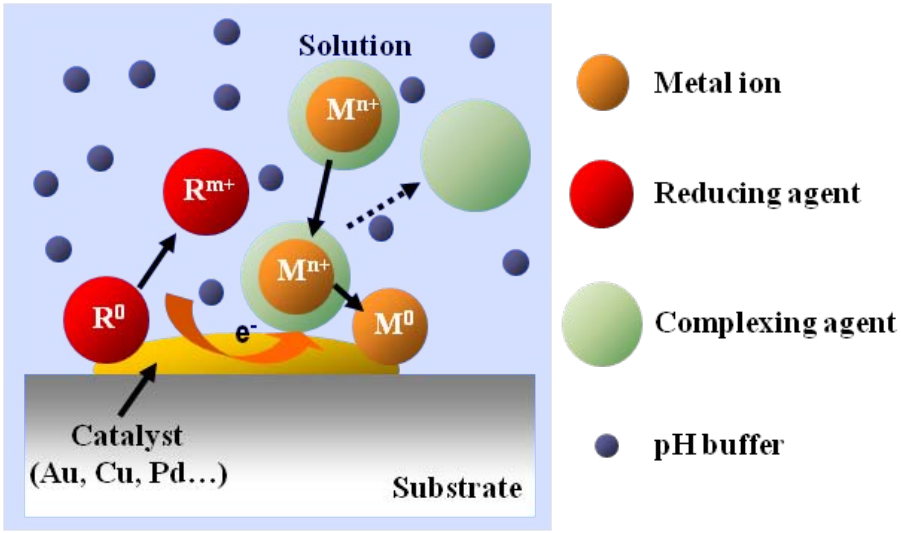

Fig. 1-14. Schematic diagram of electroless deposition of metals.

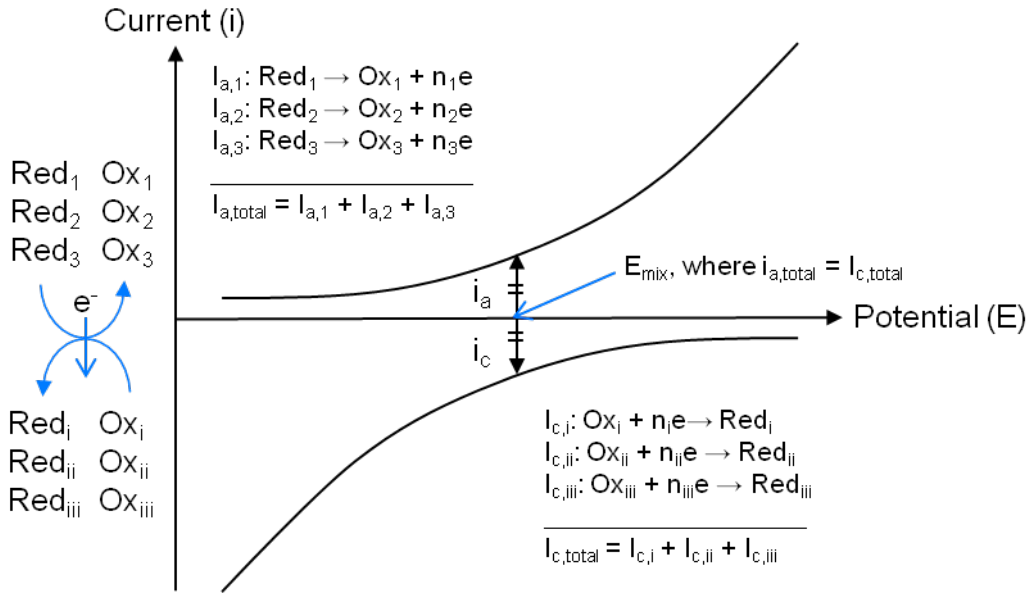

Fig. 1-15. Schematic diagram of mixed potential theory (adapted from [71])

Table 1-3. Oxidation Reactions of the Reducing Agents for Electroless Deposition

Name	Structure	Reaction
Hydrazine	N_2H_4	$N_2H_4 + 4OH^- \rightarrow N_2 + 4H_2O + 4e^-$
Dimethylamine borane	$(CH_3)_2NHBH_3$	$(CH_3)_2NHBH_3 + H_2O \rightarrow (CH_3)_2NH_2^+ + BH_3OH^-$ $BH_3OH^- + 8OH^- \rightarrow BO_3^{3-} + 6H_2O + 6e^-$
Sodium borohydride	$NaBH_4$	$BH_4^- + 8OH^- \rightarrow BO_2^- + 6H_2O + 8e^-$
Sodium hypophosphite	NaH_2PO_2	$H_2PO_2^- + 3OH^- \rightarrow HPO_3^{2-} + 2H_2O + 2e^-$
Formaldehyde	HCHO	$HCHO + H_2O \rightarrow HCOOH + 2H^+ + 2e^-$

1-5. Sonochemistry in Fuel Cell

Ultrasound is a sound wave with a frequency ranging from 16 kHz to 5 MHz for gases, and to 500 MHz for liquids and solids [77]. The ultrasound has been used in a variety field such as physics, chemistry, and biology. Specifically, the use of ultrasound has found various applications in the chemical and processing industries, since it enhances both synthetic and catalytic processes. This area of research is named sonochemistry [77,78]. Sonochemistry mainly deals with the reactions involving liquid by increasing the reaction rates [77]. However, most of the observed effects of ultrasound on surfaces and the chemical reactions, derived from ultrasound irradiation, is not by ultrasound itself, but by the secondary effect, called ‘cavitation effect’. Cavitation is a phenomenon where micro-bubbles are formed and collapse violently on the surface, leading to generation of high energy. Indeed, ultrasound consists of alternating compression and rarefaction cycles when it passes through the liquid medium (Fig. 1-16) [79]. During rarefaction cycles, negative pressures developed by the high power ultrasound are strong enough to overcome the intermolecular forces binding the fluid. The succeeding compression cycles can cause the micro-bubbles to collapse almost instantaneously with release of large amount of energy (5000 K, 2000 atm). This energy is transferred to the system and chemical reactions proceed.

There have been a few reports on using ultrasound for fabricating noble metals and catalysis, and preparing materials for fuel cell application. In 1992, Nagata et al. prepared stable colloidal

silver by ultrasonic irradiation of aqueous silver precursor solution in the presence of surfactant [80]. Okitsu et al. [81] and Mizukoshi et al. [82] also attempted to prepare mono-metallic nanoparticles via ultrasound irradiation. Okitsu et al. synthesized Ag, Pd, Au, and Pt of nanometer size with a relatively narrow distribution. Mizukoshi et al. reduced the size of Pt nanoparticle as small as 2.6 nm using sodium dodecyl sulfate (SDS) as a surfactant. From both studies, the researchers attributed the formation of metal nanoparticle to the reduction of metal ions by reducing species, generated by water sonolysis. Not only mono-metallic nanoparticle, but bi-metallic nanoparticles were synthesized, and applied in electrochemical reaction of fuel cell. Kim et al. [83] produced Pd-Sn bi-metallic nanoparticles and showed their electro-catalytic activity for oxygen reduction in alkaline electrolyte. It was from 1997 that ultrasound was used to fabricate carbon-supported metal catalyst [84,85]. Bianchi et al. [84] induced heterogeneous reduction of metal ion in the presence of highly conductive carbon black (CB), and increased metal dispersion. Furthermore, it was able to synthesize supported non-noble metal catalyst [86] and metal carbides [87] by using ultrasound. Other than CB, non-carbonaceous support was used, such as tin oxide, titanium oxide, and indium tin oxide (ITO), which exhibited good corrosion resistance, and strong metal-support interaction [88,89]. The application of ultrasound was extended to the direct fabrication of fuel cell electrode. Normally, the electro-catalysts were mixed with ionomer and solvent by ultrasound agitation, and spread on the GDL (catalyst-coated substrate, CCS) or the polymer membrane (catalyst-coated membrane, CCM). Not only in mixing, but in spraying process, the ultrasound could be adopted. It was reported that

PEMFC electrodes prepared by ultrasonic spray system showed better performance compared to the electrode, made by normal spray system [90].

Application of ultrasonic in preparation of dispersed nanoparticles, supported catalysts, and fuel cell electrode has provided many advantages over other candidate methods. Since, fuel cells strongly depend on the use of effective catalyst whether it is mono-metallic or bi-metallic. Therefore, ultrasound is definitely a promising method in fuel cell technologies. In this study, ultrasound was applied to deposit Pt over the uniform-sized colloidal silica particle (SiO_2). The Pt-SiO_2 composite was utilized as an anode catalyst for PEMFC, and its activity was tested through electrochemical analysis. Moreover, the catalyst was loaded on the fuel cell electrode and the performance of the membrane assembly with the composite was tested via single-cell experiment. By the virtue of hydrophilic property of SiO_2, the catalyst layer was expected to possess a self-humidifying ability, and the MEA would operate well even under low-humidity condition. Since the dehydration of normal MEA is severe with low-humidity, specifically at high current density region, as-prepared MEA may overwhelm the conventional MEA.

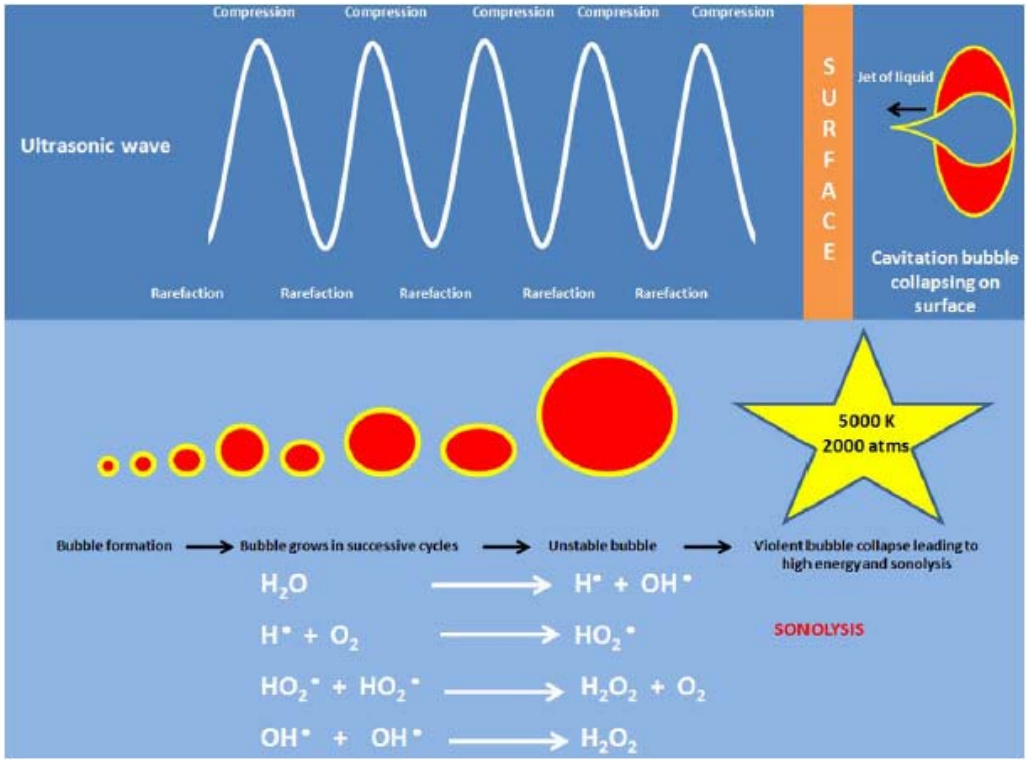

Fig. 1-16. Cavitation formation by ultrasonic wave [79].

CHAPTER II

Experimental

2-1. Synthesis of Carbon-Supported Pt_{shell}-Pd_{core} Nanoparticle

Carbon-supported Pd catalyst (Pd/C) was synthesized via novel colloidal method [91]. 44.51 mg of $PdCl_2$ (Sigma–Aldrich) was dissolved in 150 ml of de-ionized water with 1 ml of 1 M HCl(aq) solution. 47.3 mg of carbon black (VulcanXC-72, Cabot corp.) was dispersed in 50 ml of de-ionized water with 50 ml of IPA (isopropyl alcohol, JUNSEI) by ultrasonic. Both solutions were mixed and stirred vigorously. 24.6 mg of Na_2WO_4 was added in the mixed solution to achieve colloidal process. 20 ml of 0.1M $NaBH_4$ solution was added drop-wise into the solution to finalize the synthesis of Pd/C. Pd/C was washed and filtered with de-ionized water until no chloride was detected. Finally, the catalyst was dried in vacuum at 60^{o}C for 8 h.

The solution for Cu ELD was prepared with the following composition; 3.6 mM $CuSO_4 \cdot 5H_2O$, 7.7 mM ethylenediaminetetraacetic acid (EDTA), and 7 mM para-formaldehyde $(CH_2O)_n$ in 200 ml of de-ionized water. The pH of the solution was adjusted up to 12 by adding 0.052 M KOH. 20 mg of Pd/C was ultrasonically dispersed in 5 ml of IPA and 5 ml of de-ionized water. Then, the suspension was added into the Cu ELD electrolyte. The reaction occurred at 75^{o}C for 5 min. The temperature was chosen, because the formation of Cu oxide during the electroless deposition was least probable, and the electrolyte was stable at the temperature above 70^{o}C. The

solid powder (Cu ad-layer on Pd/C) was filtered, and placed into 1 mM H_2PtCl_6 (hexachloroplatinic acid, Sigma-Aldrich) in 0.05 M H_2SO_4 solution for 30 min to replace Cu ad-layer with Pt deposit. During the displacement reaction, the temperature was maintained at 75^{o}C. The synthesized catalyst, Pt_{shell}-Pd_{core}/C, was filtered and dried at 50^{o}C in vacuum. At last, in order to reduce Pt that was deposited on Pd, H_2-reduction (pure H_2, 100 ccm) was performed in a closed vessel at 120^{o}C for 1 h. The schematic diagram for the overall process was given in Fig. 2-1.

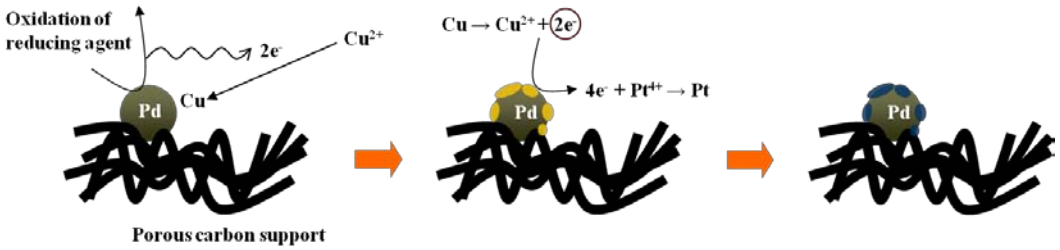

Fig. 2-1. Description of synthetic process of Pt_{shell}-Pd_{core}/C; electroless deposition of Cu on carbon-supported Pd, and successive displacement of Cu by Pt via galvanic displacement reaction.

.

2-2. Sonochemical Synthesis of Pt-Deposited SiO_2/C

The SiO_2 nanoparticles were synthesized by water-in-oil (W/O) micro-emulsion method [92]. In detail, 180 ml of cyclohexane (Sigma-Aldrich), 43.2 g of triton X-100 (Sigma-Aldrich), 13.45 ml of de-ionized water, and 32.8 ml of n-hexanol (Sigma-Aldrich) were mixed for 10 min. 2.4 ml of tetraethylorthosilicate (TEOS, Sigma-Aldrich) was added into the mixture solution. Addition of 1.44 ml of ammonium hydroxide (NH_4OH, Sigma-Aldrich) initiated the synthesis of colloidal SiO_2 nanoparticles. After 24 h, the nanoparticles were separated by ethanol and centrifugation.

SiO_2 nanoparticles were re-dispersed in 30 ml of de-ionized water by sonication for 30 min. Then, 6 ml of 0.488 M of hexachloroplatinic acid hydrate ($H_2PtCl_6 \cdot xH_2O$, Sigma-Aldrich) was added to the solution, and sonicated with power of 80 W/cm^2 for 15 min. 4 ml of sodium hydroxide (NH_4OH, Sigma-Aldrich) was dropped into the mixture solution before the ultrasound was applied. Pt-deposited SiO_2 NPs (Pt-SiO_2) were washed with de-ionized water over times, centrifuged, and dried at 60^{o}C for overnight. The overall synthetic process of Pt-SiO_2 was demonstrated in Fig. 2-2. 4 mg of carbon black was added to 10 mg of Pt-SiO_2. The mixture was then thermally treated under the given atmospheric condition (H_2/Ar = 1:9) for 3 h. After cooled down, Pt-SiO_2 with conducting carbon (Pt-SiO_2/C) was collected.

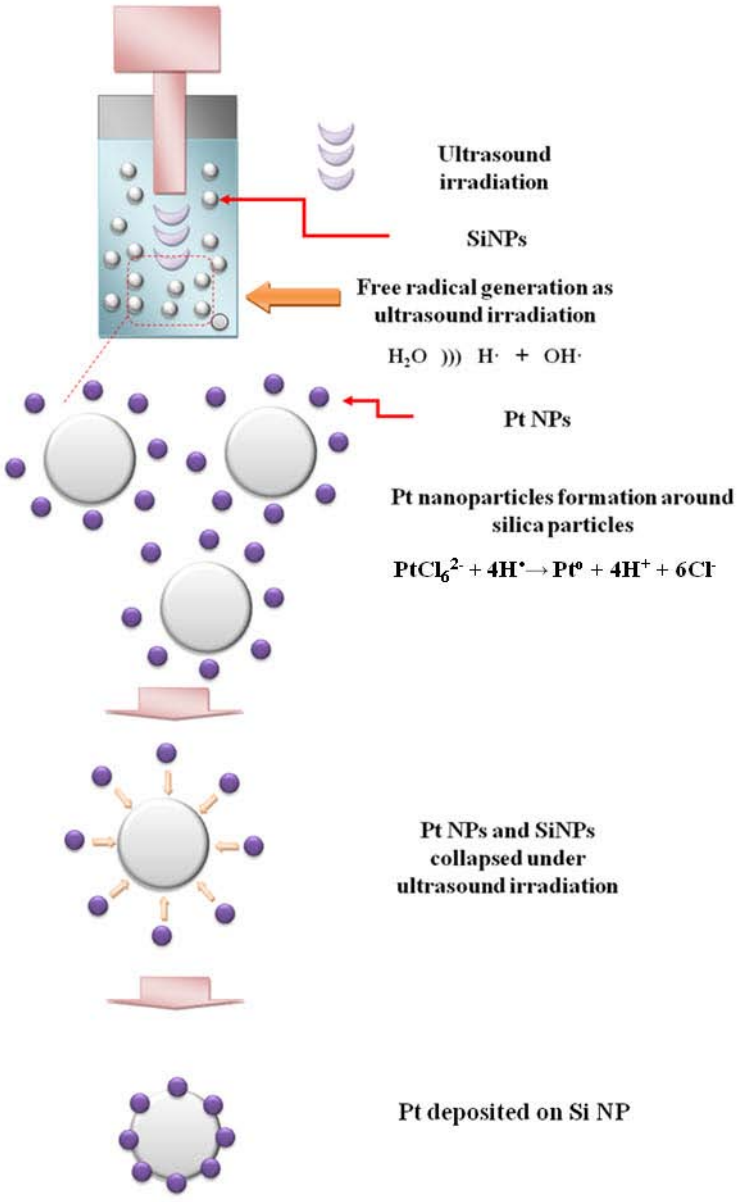

Fig. 2-2. Illustration of synthetic process of Pt-SiO_2 composite via ultrasonic irradiation.

2-3. Physical Characterization of Electro-Catalysts

The high power X-ray diffractometer (XRD, Rigaku Corp.) was used to detect metals such as Cu, Pd, and Pt for preparation of Pt_{shell}-Pd_{core}/C. The elemental compositions of the catalysts were investigated using X-ray photoelectron spectroscopy (XPS, Thermo) with an Al K source type. XPS revealed the oxidation state of metals as well as their existence. Furthermore, the electronic structure of selected metal could be obtained from XPS analysis. All spectrums were referenced to C_{1s} (284.6 eV) and fitted by XPSPEAK41 software for deconvolution. High resolution transmission electron microscope (HR-TEM, Technai-F20, FEI and JEM-3010, JEOL) was used to image electro-catalyst. Even though the electron accelerating voltage of Technai-F20 was 200 kV (~930kx), it was specialized to perform atomic analysis. It was equipped with high angle annular dark filed (HAADF) detector in scanning transmission electron microscope (STEM, ~230Mx) mode. Thus Technai-F20 was capable of obtaining dark field image as well as bright field image, and differentiating heavy and light elements by Z-contrast. Energy dispersive X-ray spectroscopy (EDS) line scanning could monitor geometric distribution of metals in Pt_{shell}-Pd_{core} /C, and prove shell-core structure by their position. JEM-3010 had 300 kV of electron acceleration, therefore it could visualize the sample with high magnification up to 150xM. It was useful to confirm the crystallinity of small Pt nanoparticles on the surface of SiO_2.

Thermogravimetric analysis (TGA) could measure the amount of Pd loaded in the carbon

support after colloidal preparation, and total metal amount in Pt_{shell}-Pd_{core}/C. The relative amount of each metal in Pt_{shell}-Pd_{core}/C and Pt amount in Pt-SiO_2 composite were calculated either from inductively-coupled plasma mass spectroscopy (ICP-MS, SHIMADZU, ICPS-7500) or ICP Auger electron spectroscopy (ICP-AES, Perkin-Elmer, Optima-4300 DV) analysis.

2-4. Electrochemical Analysis of Electro-Catalysts

The electrochemical analyses were performed in a standard three-electrode electrochemical cell. Using a glassy carbon rotating disk electrode (RDE, 0.126cm^2) connected to Versastat^{TM} II (EG&G, Princeton Applied Research Corporation), the cell potential was recorded with respect to Ag/AgCl (KCl, 3.5M) reference electrode (−0.205V vs. normal hydrogen electrode, NHE). The Pt spring wire was chosen as a counter electrode. In ORR the potentials were re-scaled with respect to real hydrogen electrode (RHE) referring the solution pH.

For Pt_{shell}-Pd_{core}/C electro-catalyst, the electrode was prepared by coating the catalyst ink suspension on the glassy carbon working electrode. In detail, the uniform Pt_{shell}-Pd_{core}/C suspension was made by mixing 10mg of Pt_{shell}-Pd_{core}/C with 66 ul of perfluorosulfonic acid (PFSA) polymer dispersion (5 wt% polymer content, D520, Dupont^{TM}), also known as Nafion^{TM} solution, and 1 ml of IPA in order. The mixture was stirred by ultrasonic agitation for 1 hr. 27 ul of the Pt_{shell}-Pd_{core}/C suspension was placed on the polished glassy carbon electrode with micropipette and dried in air for 10 min. The suspension was in ultrasonic again for 5 min before each measurement. The commercial carbon-supported Pt catalyst (Pt/C, Johnson Matthey, 40 wt%) was also prepared by exactly the same method and the composition. For Pt-SiO_2/C composite catalyst, however, 33 ul of Nafion^{TM} solution and 1 ml of IPA solution were mixed with 10 mg of the composite.

The cyclic voltammetry (CV) over Pt_{shell}-Pd_{core}/C catalyst was performed in the 0.05 M H_2SO_4.

The electrolyte was de-aerated with N_2 prior to the measurement, and was being purged during the measurement (0.0 ~ 1.2 V vs. NHE). For ORR experiment, however, O_2-saturated 0.2 M perchloric acid ($HClO_4$, JUNSEI, 70%) was used, and the sweep range was 0.0 ~ 1.05 V vs. NHE. The temperature was maintained at 293 K by thermostat. The kinetics of ORR over Pt_{shell}-Pd_{core}/C could be obtained from the measured current density over the potential range (0.2V～1.05 V vs. NHE). The kinetics of oxygen reduction by Pt/C was also evaluated, and was compared to Pt_{shell}-Pd_{core}/C. Methanol (MeOH) electro-oxidation was performed in 0.5 M H_2SO_4 + 0.5 MeOH (0.0 ~ 1.2 V vs. NHE). The electrolyte was purged with N_2 before and during the measurement. Both catalysts were pre-treated in MeOH-free H_2SO_4 prior to the real measurement by sweeping multiple times until the constant voltammogram was obtained. After the pre-treatment was done, MeOH was added in H_2SO_4. The catalytic activity of Pt/C and Pt_{shell}-Pd_{core}/C for methanol oxidation was measured by chronoamperommetry at 0.50 V vs. NHE. The kinetics and mechanisms of methanol oxidation for both catalysts were investigated with comparison. CO was flown into H_2SO_4 for 15 min while holding the working electrode potential at 0.2 V (vs. NHE) to adsorb CO on Pt_{shell}-Pd_{core}/C and Pt/C. In order to remove trace of CO from the gas phase, N_2 was fed above the electrolyte. CO_{ad}-stripping was performed by sweeping potential from 0.2 V to 1.2 V, and back to 0.2 V (vs. NHE) with 10 mV/s. The apparatus for the electrochemical analysis is given in Fig. 2-4. The electro-catalytic activity of Pt-SiO_2/C was investigated with the same experimental condition and apparatus, but in 0.2 M $HClO_4$ for CV measurement.

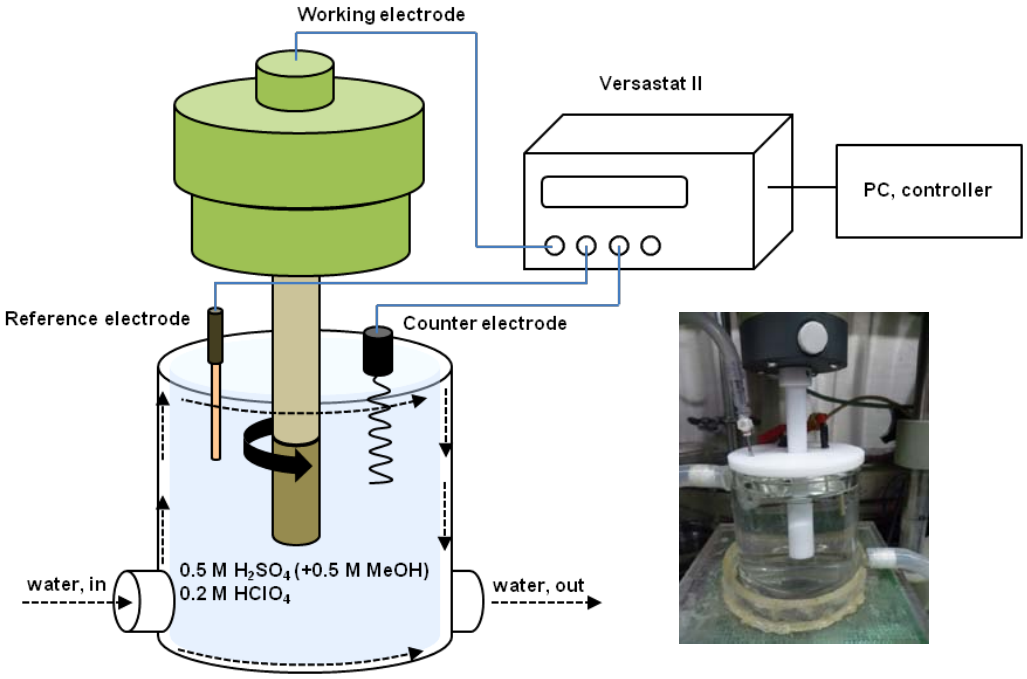

Fig. 2-3 Apparatus for electrochemical analysis of electro-catalyst; three-electrode cell in which counter and reference electrode were inserted.

2-5. Single-Cell Experiment

The MEA with Pt-SiO_2/C (MEA-PSC) was fabricated by catalyst-coated substrate (CCM) method. For anode, Pt-SiO_2/C ink was prepared by ultrasonic mixing of 10 mg of the composite with 0.1 ml of de-ionized water and 0.6 ml of IPA with 55 $\mu\ell$ of Nafion^{TM} solution. The ratio of the polymer ionomer to the catalyst was fixed approximately to 15 wt% for avoiding ionomer effect, and Pt loading was 0.1 mg_{Pt}/cm^2. The catalyst ink was sprayed on the porous GDL (35BC from SGL, active surface area of 5 cm^2), and the catalyst-loaded GDL was dried in mini-furnace at 70 °C for 10 min. For cathode GDL, commercial Pt/C (40 wt% Pt, Johnson Matthey) was used with same preparation procedure, but 0.2 mg_{Pt}/cm^2 of Pt loading. Then, both cathode and anode GDLs were pressed (125^{o}C, 300 psi, 2 min) with the polymer membrane (Nafion 212, Dupont^{TM}) placed between them. The MEA, fabricated with commercial Pt/C on both anode and cathode (MEA-PC) was also prepared with corresponding Pt loading to the MEA-PSC for anode and cathode, respectively. The MEA with Pt_{shell}-Pd_{core}/C was made by same procedure as MEA-PSC was prepared, with the only exception that the as-prepared catalyst was sprayed on the cathodic GDL.

The performance of the MEA-PSC, MEA-PC, and MEA with Pt_{shell}-Pd_{core}/C were evaluated by integrated fuel cell station (custom-made, CNL). The experiment was performed in galvanostatic mode with current ranging from 0 A/cm^2 to 3 A/cm^2. The reactant gases were pure H_2 (100 ccm) and O_2 (200 ccm) for anode and cathode, respectively, and fed through humidifier.

For Pt-SiO_2/C composite experiment, the relative humidity was controlled by humidifying the reactant gases with different temperature (70, 65, 55, 50, and 45^{o}C). In this study, only temperature of anode humidifier was altered and that of cathode was maintained. Each MEA was activated prior to the measurement at 70^{o}C. The schematic diagram, which depicts the fabrication of MEA-PSC and the single-cell experiment, was given in Fig. 2.5.

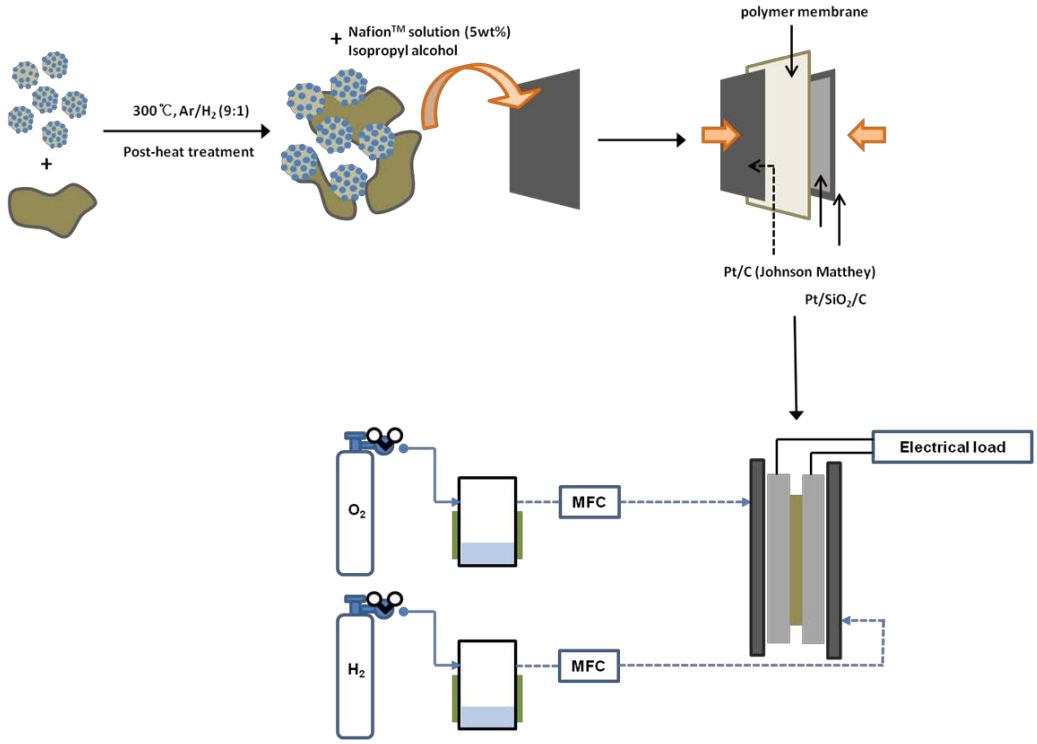

Fig. 2-4. Illustration of preparing the MEA embedded with Pt-SiO_2/C composite in the anode GDL (MEA-PSC), and single-cell experiment in H_2-O_2 system.

CHAPTER III

Pt_{shell}-Pd_{core}/C Electro-Catalyst for Oxygen Reduction Reaction

3-1. Preparation of Pt_{shell}-Pd_{core}/C

The primary object of this experiment is to cover Pd nanoparticle with Cu ad-layer, because the surface coverage of Cu determines the following uniform deposition of Pt. Therefore, the feasibility of Cu ELD on Pd nanoparticle was investigated with concentrated ELD solution. As-prepared Pd/C catalyst was added in Cu ELD solution consisting of 0.025 M $CuSO_4 \cdot 5H_2O$, 0.054 M EDTA, 0.097 M CH_2O, and 0.481 M KOH. Few minutes later, the catalyst precipitated on the bottom, indicating ELD of Cu on the catalyst (Cu-deposited Pd/C). As confirmed by X-ray diffraction Cu was deposited on the catalyst with high amount (Fig. 3-1). The deposited Cu was highly crystalline, and some oxide was also formed. The oxide formation during Cu ELD was somewhat inevitable as it was supported by Pourbaix diagram of Cu (Fig. 3-2). It has been reported that the Cu oxide formation during reaction could be inhibited by elevating the reaction temperature, or by purging the electrolyte with N_2 prior to the reaction. In this study, however, the amount of Cu oxide seemed to be insignificant and the oxide did not impede synthetic process, which will be confirmed in chapter 3-2. Therefore, most of Cu oxides in XRD were believed to be from the exposure to air prior to the analysis.

Cu-deposited Pd/C was filtered once and transferred to Pt precursor electrolyte. After 30 min

of displacement reaction, the catalyst (Pt-deposited Pd/C) was filtered and washed by de-ionized water and dried. Once again, X-ray diffraction analysis was performed to characterize the catalyst (Fig. 3-3). From X-ray diffraction, Cu characteristic peaks were not observed, which indicated that Cu deposited was completely removed by displacement. However, it was difficult to verify Pt was deposited as a result of displacement. There was no doubt that the characteristic peaks neat at 40^{o}, 46^{o}, and 68^{o} were for Pd. But they could also be assigned to Pt, since the diffraction angle of Pt and Pd were very close. Therefore, XRD was not suitable to differentiate Pt from Pd. What is more important is that the amount of Cu deposited should be minimized in order to from thin Pt layer. In other words, when the composition of Cu electrolyte was optimized and the amount of Cu was reduced, it would be far more difficult to detect Cu in Cu ad-layer on Pd/C from XRD, and in return, to separate Pt from Pd. As seen in Fig. 3-4, Cu was not detected when the optimized concentration of Cu ELD solution was used. Therefore, the detection limit of analysis should be as small as possible. For this reason, spectroscopic method was used with reduced amount of Cu in Cu ad-layer on Pd/C.

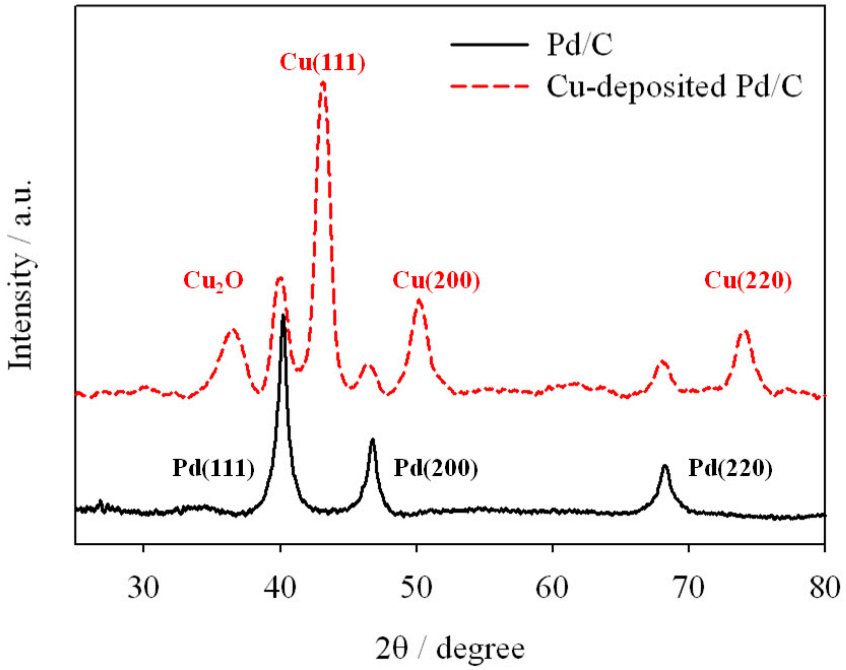

Fig. 3-1. X-ray diffraction results of Pd/C (solid line, black) and Cu-deposited Pd/C (dotted line, red), prepared with concentrated Cu ELD solution.

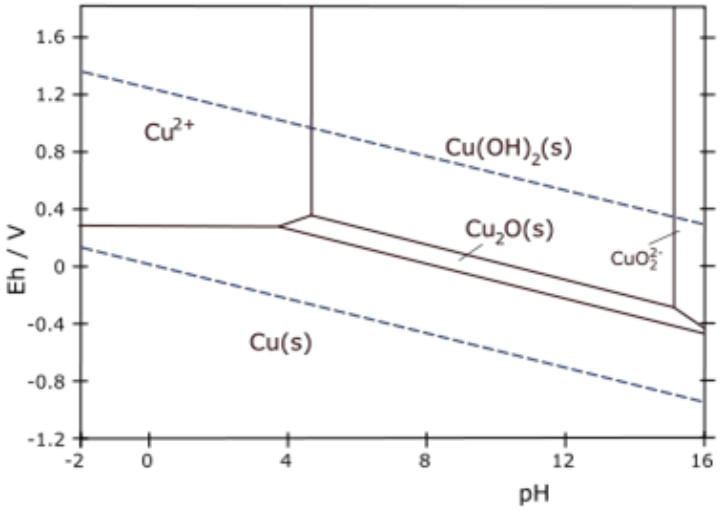

Fig. 3-2 Pourbaix diagram of Cu [93]

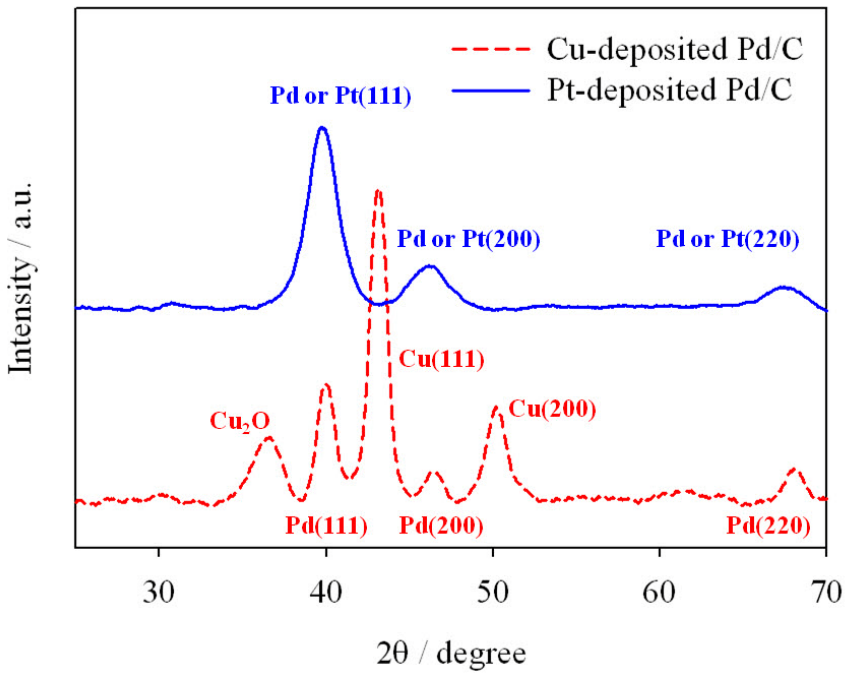

Fig. 3-3. X-ray diffraction results of Cu-deposited Pd/C (dotted line, red) and Pt-deposited Pd/C (solid line, blue) after galvanic displacement of Cu by Pt.

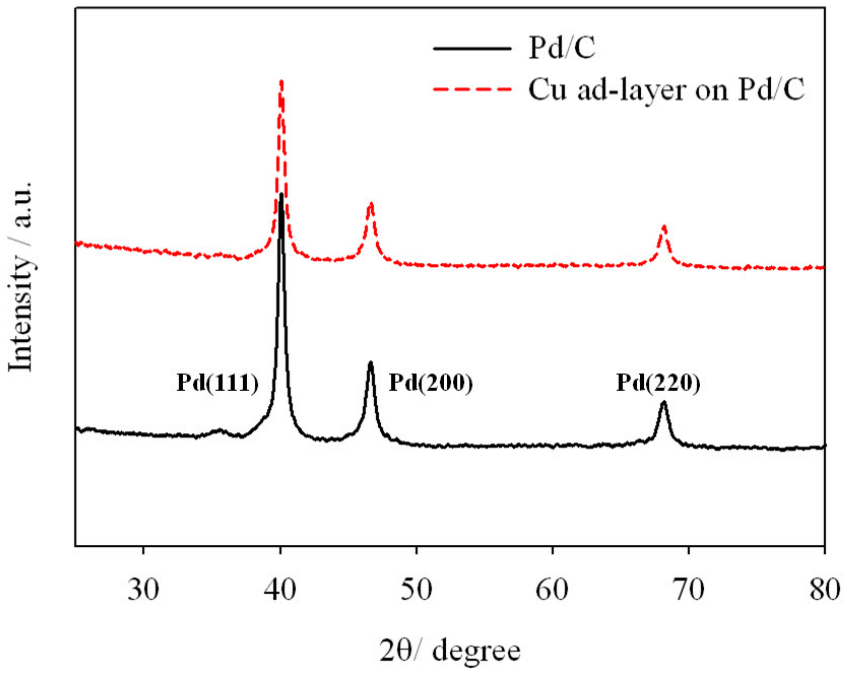

Fig. 3-4. X-ray diffraction results of Pd/C (solid line, black) and Cu ad-layer on Pd/C (dotted line, red), prepared by with optimized concentration of Cu ELD solution.

3-2. Characterization of Pt_{shell}-Pd_{core}/C

More diluted and optimized concentration of ELD solution (3.6 mM $CuSO_4 \cdot 5H_2O$, 7.7 mM EDTA, 7 mM CH_2O, and 52 mM KOH) was used for the actual preparation of Cu ad-layer on Pd/C nanoparticle. Then, Cu ad-layer on Pd/C was investigated using XPS (Fig. 3-5 and Fig. 3-6). The deposition of Cu was confirmed in XPS spectra in Fig. 3-6(a). Even in small amount of Cu deposit, Cu oxide was involved. Pd/C also possessed small portion of oxide as it was seen in Fig. 3-6(b). Fig. 3-7(a) is the image of Cu ad-layer on Pd/C from HAADF-STEM analysis. The different brightness indicated that there existed dissimilar elements on the carbon support. In addition to the deposition of Cu itself, the horizontal distribution of Cu on Pd should be considered. Thus, the supporting TEM analysis was carried out to achieve the intensity profiles of Cu and Pd along the scan line as shown in Fig. 3-7(b). Over the scan range of 40 nm, the distribution profile of Cu accorded with the profile of Pd. In conclusion, it seemed that Cu was selectively reduced on Pd via ELD process.

After depositing Cu on Pd, the displacement reaction by Pt was attempted for 30 min to synthesize Pt_{shell}-Pd_{core}/C. Once again, the removal of Cu and the subsequent displacement by Pt were confirmed by XPS. A survey scan for Pt_{shell}-Pd_{core}/C was given in Fig. 3-8. As evidenced in the spectrum of Fig. 3-9(a), neither Cu metallic nor Cu oxides peak was observed. Moreover, XPS measurement could distinguish Pt from Pd. The existence of Pt in the Pt_{shell}-Pd_{core}/C was confirmed by Pt characteristic peaks locating at $4f_{7/2}$ (71.7 eV) and $4f_{5/2}$ (74.6 eV) in Fig. 3-9(b).

Pd core maintained its metallic composition (Fig. 3-9(c)). The successful removal of Cu as a result of displacement was supported by ICP-MS analysis. The Cu content in Pt_{shell}-Pd_{core}/C was measured with various displacement periods as shown in Fig. 3-10. The longer the displacement time, the less Cu was present in Pt_{shell}-Pd_{core}/C. After 30 min of displacement reaction, the amount of Cu was negligible. The lateral distribution of Pt and Pd was confirmed by STEM-HAADF again (Fig. 3-11). It was revealed that the intensity profile of Pt took after the profile of Pd, indicating that the displacement reaction was effective. Some isolated Pt nanoparticles were observed from the EDS scanning. This was attributed to thermal migration of Pt deposit during post heat treatment. More direct evidence for core-shell configuration was provided by elemental mapping by EDS in Fig. 3-12. In STEM mode, point EDS analysis was conducted to search the Pt_{shell}-Pd_{core} nanoparticle, and the selected nanoparticle was scanned for a short time in order to avoid drift during the mapping. It was observed that the diameter of Pt was greater than the diameter of Pd, meaning that Pt covered Pd. Moreover the amount of deposit of Pt and Pd could be referred by their contrast. Especially, the center part of Pd showed the highest brightness compared to the boundary layer confirming that Pd was in a core position. There might be a concern that the Pt_{shell}-Pd_{core} configuration would not be preserved during steady state or electrochemical reaction due to the reconstruction, such as Pd segregating to the surface, or Pt incorporating Pd core. At equilibrium, the direction of segregation between metals is governed by the surface segregation energy (E_{segr}), which was determined by the difference in the surface energies of corresponding metals. The trend in E_{segr} with 3d, 4d, 5d-transition metals

was studied and summarized with a 24x24 matrix by J.K. Norskov (Fig. 3-13) [34]. When E_{segr} was negative the inner metal segregates to the surface, and the metals were separated. When E_{segr} was positive, however, it is hard for metals to segregate and remain mixed. As shown in Fig. 3-13, the structure with Pd core and Pt shell had very small positive E_{segr}, which meant that the reconstruction was unlikely to happen. The reconstruction could also happen in a reactive condition, such as in the state of oxygen adsorption. It was already revealed that the E_{segr} was slightly positive (0.02 eV), when 0.25 ML of oxygen was adsorbed on the surface of Pt/Pd slab catalyst, and thus the inner Pd did not move toward the surface [94].

The HR-TEM bright field image was given in Fig. 3-14(a). We concluded that as-prepared Pt_{shell}-Pd_{core}/C was highly dispersed on the carbon support with quite narrow particle size distribution. The average particle size Pt_{shell}-Pd_{core} was measured to be 3.8 nm ($\pm$0.8 nm) as shown in Fig. 3-14(b).

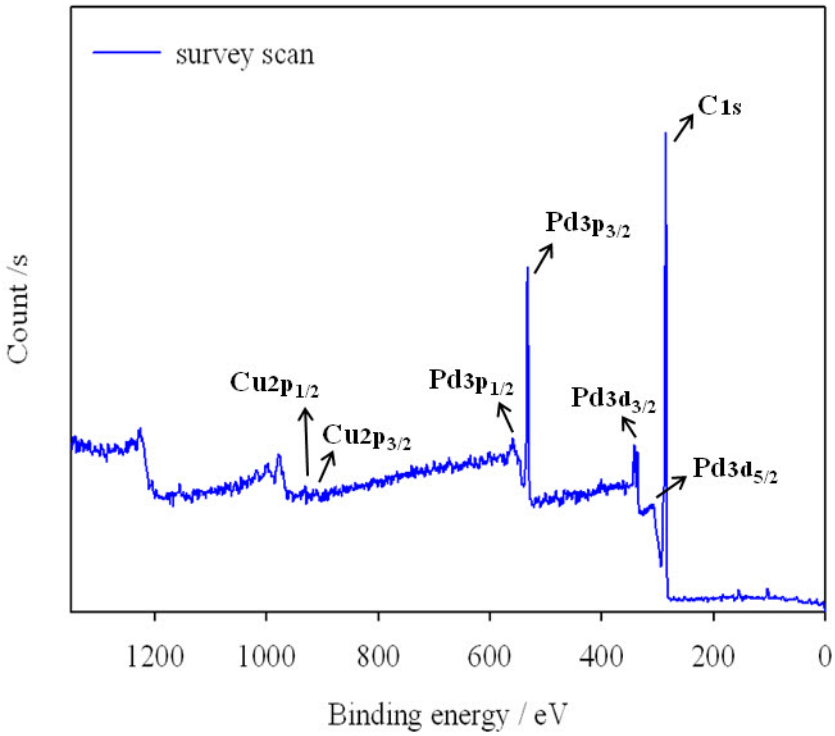

Fig. 3-5. X-ray photoelectron survey spectrum of Cu ad-layer on Pd/C (obtained from Fig. 3-4).

(a)

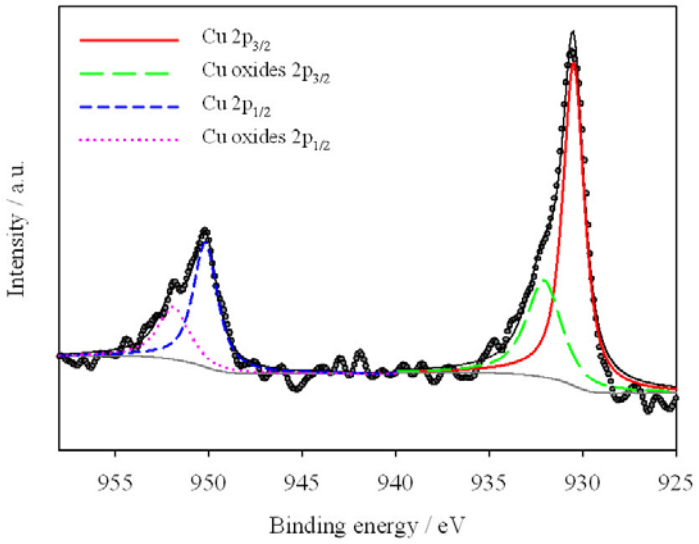

(b)

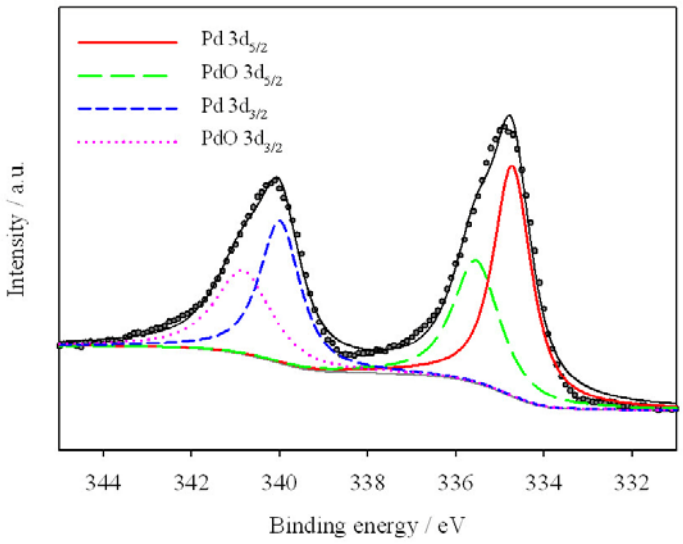

Fig. 3-6. X-ray photoelectron spectrum of (a) Cu and (b) Pd in Cu ad-layer on Pd/C (obtained from Fig. 3.4).

(a)

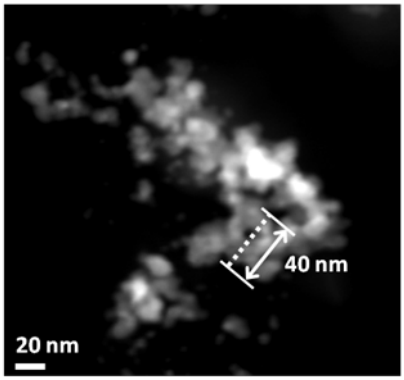

(b)

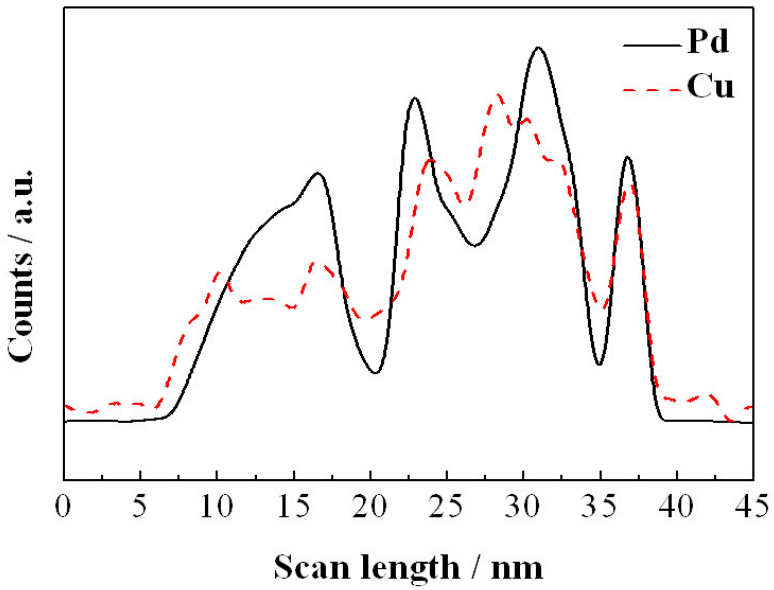

Fig. 3-7. (a) STEM-HAADF image of Cu ad-layer on Pd/C and (b) lateral distribution of Pd (solid line, black) and Cu (dotted line, red) in Cu ad-layer on Pd/C by EDS analysis.

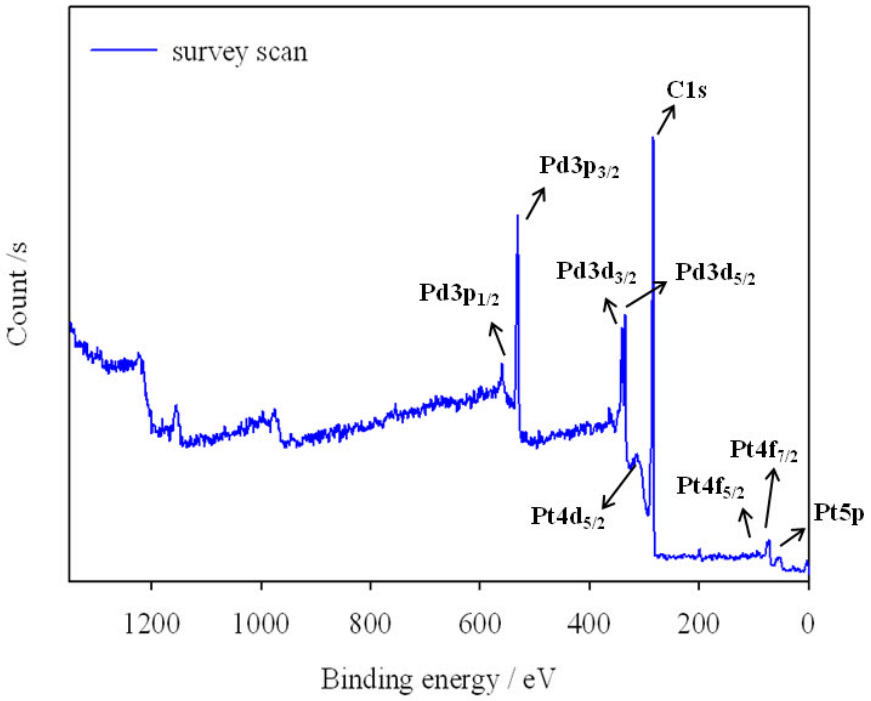

Fig. 3-8. X-ray photoelectron survey spectrum of Pt_{shell}-Pd_{core}/C.

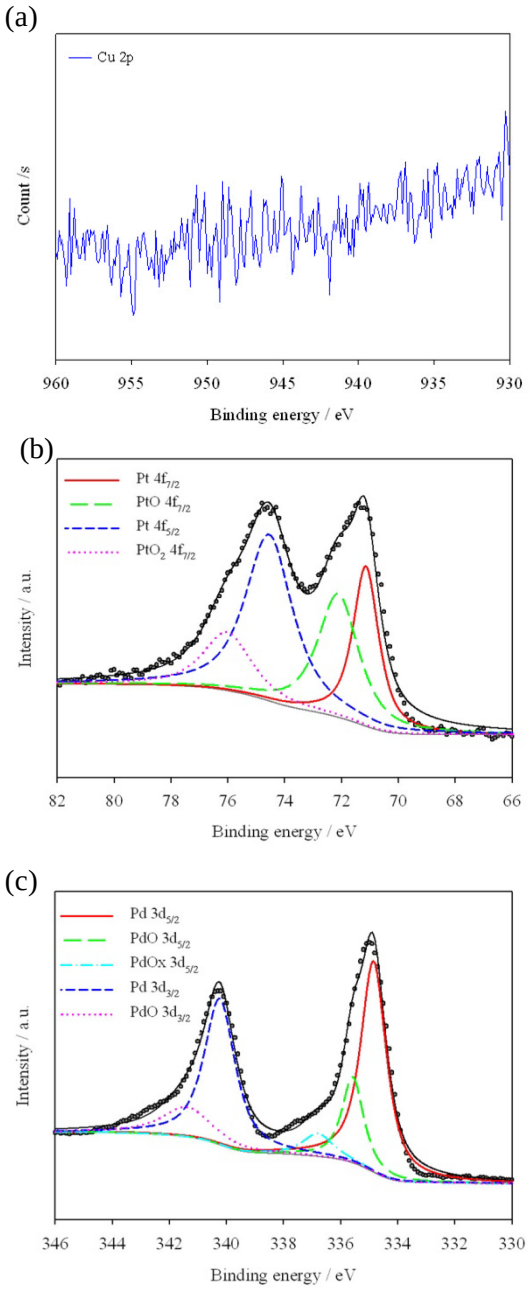

Fig. 3-9. X-ray photoelectron spectrum of (a) Cu, (b) Pt, and (c) Pd in Pt_{shell}-Pd_{core}/C; successful removal of Cu and deposition of Pt by galvanic displacement.

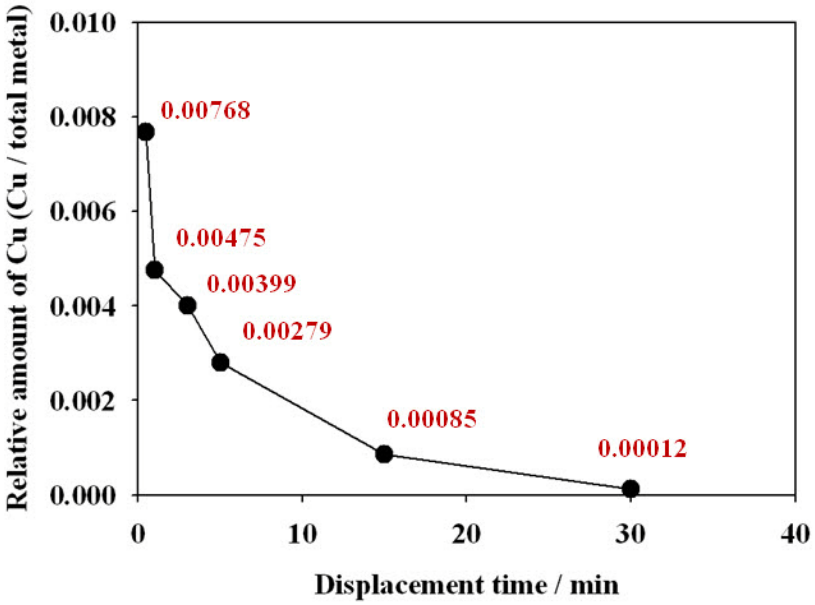

Fig. 3-10. The relative amount of Cu in Pt_{shell}-Pd_{core}/C by ICP-MS.

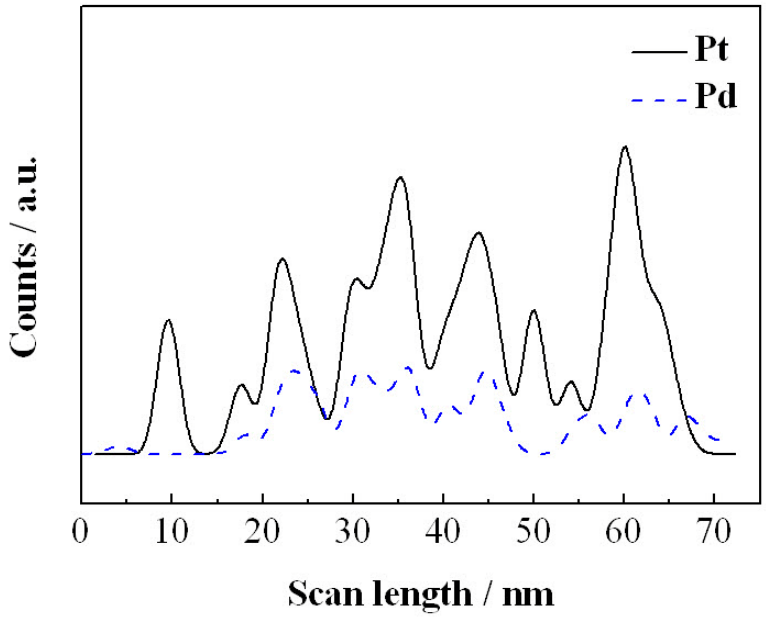

Fig. 3-11. Lateral distribution of Pd (dotted line, blue) and Pt (solid line, black) in Pt_{shell}-Pd_{core}/C by EDS analysis.

(a)

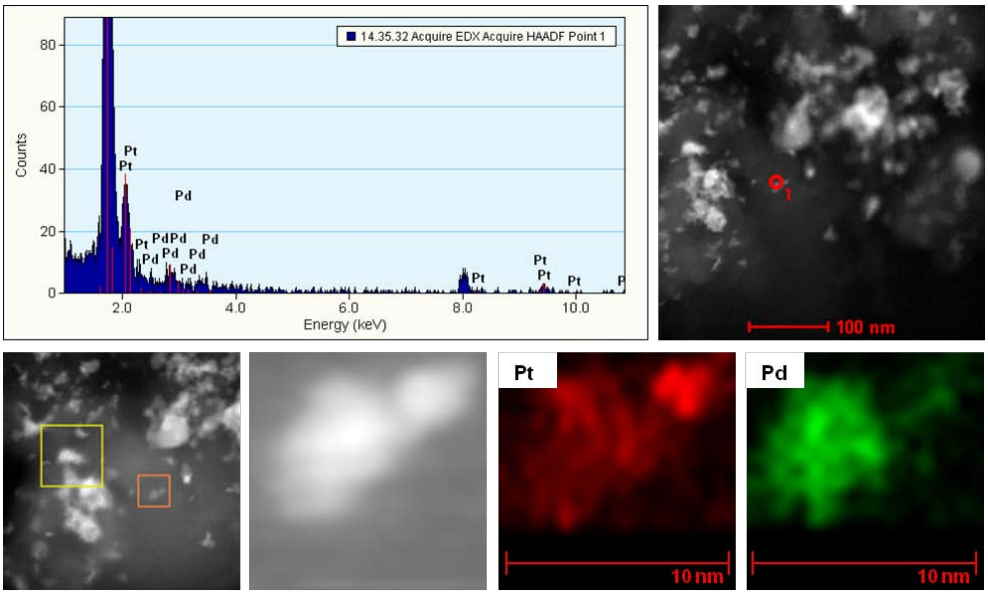

(b)

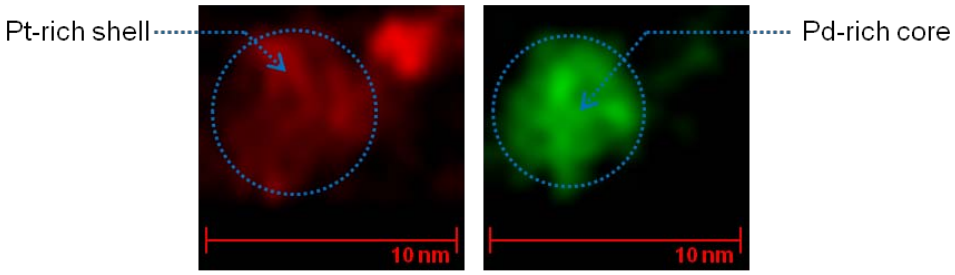

Fig. 3-12. (a) EDS result of Pt_{shell}-Pd_{core}/C (point analysis) and (b) the Pt-Pd shell-core structure confirmed by elemental mapping of Pt and Pd (contrast and size comparison).

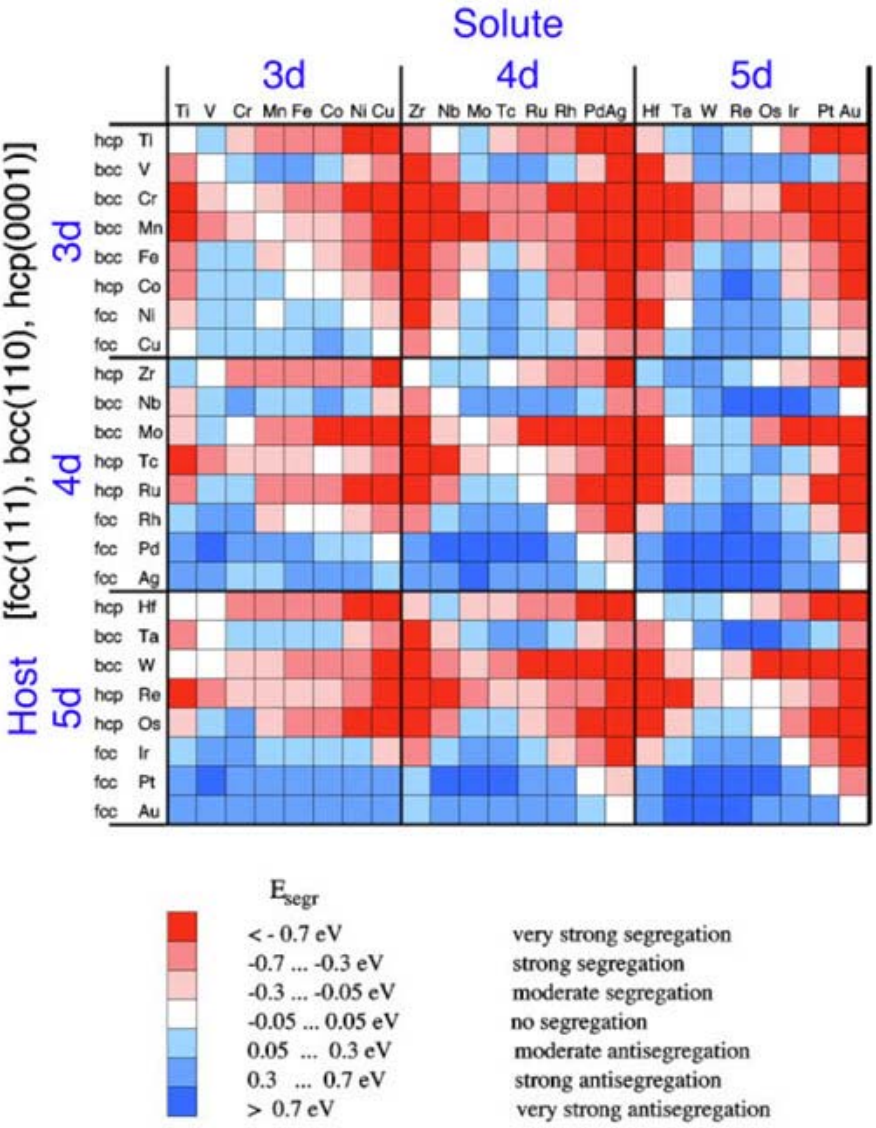

Fig. 3-13. Surface segregation energies of transition-metal impurities (solute) for the closed-packed surfaces of transition metal hosts [34].

(a)

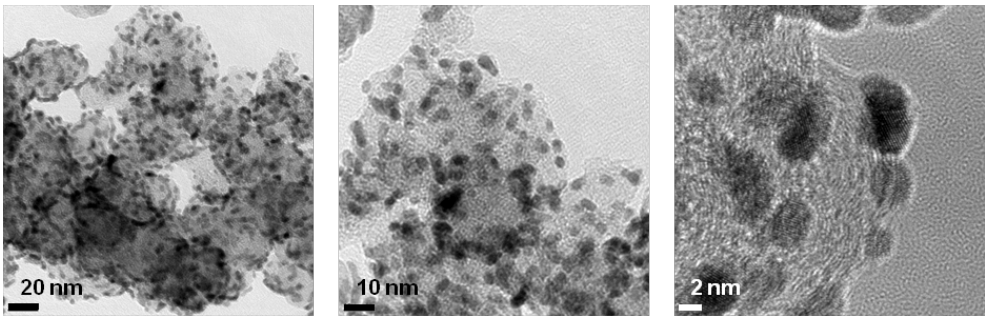

(b)

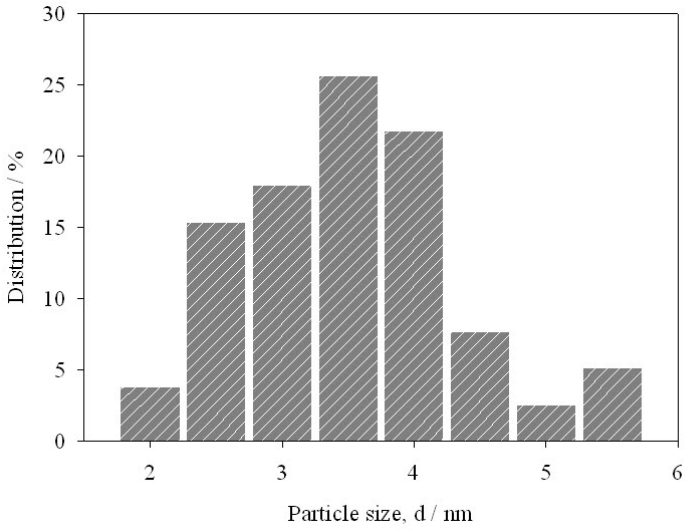

Fig. 3-14. (a) HR-TEM images of Pt_{shell}-Pd_{core}/C and (b) the histrogram for the particle size distribution of Pt_{shell}-Pd_{core}.

3-3. Catalytic Activity of Pt_{shell}-Pd_{core}/C

3-3-1. Oxygen Reduction Reaction by Half-Cell Experiment

The electrochemical analysis was done using RDE technique to investigate the catalytic activities of the synthesized catalysts. A thin-film RDE method has been known to be an effective way to calculate the accurate kinetic parameters of objective reaction in a specific limiting condition. Fig. 3-15 presented the rotating disk polarization curves for Pt_{shell}-Pd_{core}/C. The diffusion-controlled currents with different rotating rates were governed by Levich equation (Eq. 3-A) [95]. As equated above, the Levich equation predicted that the limiting current was proportional to the bulk concentration of reactant and the root of angular frequency, $\omega^{1/2}$. A high activity of Pt_{shell}-Pd_{core}/C was indicated by a half-wave potential ($E_{1/2}$) of 0.874 V when rotating rate was 1600 rpm. If the mass transfer of reactant near electrode was efficient and did not have any significant contribution to intrinsic kinetic of reaction, the current would flow in a kinetic limitation. Under this condition, Koutecky–Levich equation could be derived (Eq. 3-B). The Koutecky–Levich plots within potential range of 0.7–0.88 V were given in Fig. 3-16. The plots were obtained from the polarization curves in Fig. 3-15. A group of parallel straight lines were obtained, meaning that they have same value of slopes in the mixed kinetic-diffusion control region. The experimental value for the slope; i.e. inverse of Levich constant, was 18.35 $s^{1/2}$ mA^{-1}. It was close to the theoretical value, 17.58 $s^{1/2}$ mA^{-1}, calculated from the O_2 diffusivity

(1.97×10^{-5} cm^2 s^{-1}) [18], the kinematic viscosity of water (1.0×10^{-2} cm^2 s^{-1}) [18], and the solubility of O_2 (1.2×10^{-6} mol cm^{-3}) in the electrolyte at 20 ◦C. The theoretical value of Levich constant was obtained when the number of electron was assumed to be four. The close value of the slope in the experiment meant the total number of electron, having participated in the O_2 reduction, was comparable (experimental number of electron, nexp = 3.83).

(Eq. 3-A) $$i_{l,c} = 0.62nFAD_o^{2/3}\omega^{1/2}\nu^{-1/6}C_o^*$$

(Eq. 3-B) $$\frac{1}{i} = \frac{1}{i_k} + \frac{1}{i_{l,c}} = \frac{1}{i_k} + \frac{1}{0.62nFAD^{2/3}\omega^{1/2}\nu^{-1/6}C_o^*}$$

$i_{l,c}$ = limiting cathodic current / A cm^{-2}

i_k = kinetic current / A cm^{-2}

n = number of electron

F = Faraday constant / 96485 C

D_o = diffusion coefficient / cm^2 s^{-1}

ω = angular frequency / s^{-1}

ν = kinematic viscosity / cm^2 s^{-1}

C_o^* = bulk concentration of O in bulk / mol cm^{-3}

The kinetics of Pt_{shell}-Pd_{core}/C was also investigated with the Tafel plots for Pt/C and Pt_{shell}-Pd_{core}/C, which were obtained from the measured current density (log j_k) with respect to the reaction potential as seen in Fig. 3-17. Distinct Tafel slopes were observed at high-current

density (Pt_{shell}-Pd_{core}/C: -169.6 mV/dec, Pt/C: -170.1 mV/dec) and low-current density (Pt_{shell}-Pd_{core}/C: -57.1 mV/dec, Pt/C: -56.1 mV/dec), in agreement other studies [44,66,96,97]. Therefore, the values suggested that the first electron exchange reaction was the rate-determining step for ORR on both catalysts. Moreover, the kinetic current was slightly higher in Pt_{shell}-Pd_{core}/C than Pt/C, which meant the electron transfer was more facile on Pt_{shell}-Pd_{core}/C than on Pt/C. The increased kinetic current over Pt_{shell}-Pd_{core}/C catalyst was attributed to the electronic effect, which was driven by the second metal component, in this case Pd. As already addressed in the introduction, the catalytic activity of the strained Pt surface was tuned by forming Pt_{shell}-Pd_{core} structure. The change in the electronic structure of Pt over-layer can be estimated by ε_d shift, calculated by XPS analysis. The background-corrected XPS spectrum (-3.5 eV ~ 16.5 eV) of Pt_{shell}-Pd_{core}/C and Pt/C were obtained as seen in Fig. 3-18. In order to minimize the low-frequency noise, the scanning was performed multiple times (x100). Numerically, the ε_F of surface Pt was the binding energy, matched to the point of reflection in photoelectron spectrum. Then, we derived the weight ε_d of Pt, and speculated its position with respect to the defined ε_F. The total electron density of the valence band of Pt was calculated by integrating the spectrum ranging from -2 eV to 10 eV. ε_d was, therefore, the binding energy where the integrated DOS was in half. It was revealed that ε_d of Pt_{shell}-Pd_{core}/C shifted upward by 0.33 eV (Pt_{shell}-Pd_{core}/C: -2.32 eV, Pt/C: -2.65 eV vs. ε_F). The up-shifting of ε_d in Pt over-layer on Pd was previously reported by other groups [46,50]. Based on their calculation, Pt/Pd(111) possessed lower binding energy of atomic oxygen when it had high-lying ε_d; the trend in

catalytic activity as a function of d-band shift of Pt-based alloy and Pt_{ML} on noble metal has different behavior. In Pt_{ML} on Pd, the up-shift of ε_d reflected weak adsorption of adsorbate with feeling slight compressive strain. It ultimately indicated that the Pt over-layer experienced slight compressive strain. Accordingly Pt/Pd(111) showed higher kinetic current than other surface-modified Pt/M catalyst and pure Pt from the experiment. On Pt/Pd(111), the hydrogenation of OH (proton transfer) became easy, and OH could be readily desorbed from the surface. Our result is in agreement with above (ε_d up-shift $\rightarrow$ high activity). The increased kinetic current can be ascribed to the superior kinetics of Pt-O hydrogenation owing to up-shift of ε_d in Pt_{shell}-Pd_{core}/C. The up-shift of ε_d was also observed from XPS core-level binding energy analysis in Fig. 3-19. The core-level binding energy of Pt ($Pt4f_{7/2}$) in Pt_{shell}-Pd_{core}/C was shifted to negative direction, which assured the increased un-filled state of d-band with high-lying ε_d. The kinetics of O_2 reduction (OH desorption) for Pt/C and Pt_{shell}-Pd_{core}/C in acid electrolyte was illustrated in Fig. 3-20. More facile O_2 reduction on the surface of Pt_{shell}-Pd_{core}/C was observed than Pt/C. The improvement could be indicated by a shift of $E_{1/2}$, 13 mV, to positive direction. The faster O_2 reduction meant lower binding energy of atomic oxygen and activation energy for hydrogenation.

The ultimate purpose of this study was to adopt ELD to the synthesis of O_2 reduction reaction catalyst with less amount of Pt and to have comparable or enhanced activity over conventional platinum catalyst. Therefore, comparing mass-specific activity was necessary to confirm the reliability of the ELD method. From the result of ICP-MS, the Pt content was 7 wt% and the Pd

was 15 wt% in Pt_{shell}-Pd_{core}/C. Fig. 3-21 exhibited the mass-specific activity of Pt_{shell}-Pd_{core}/C compared to the activity of Pt/C. The mass-specific current from Pt_{shell}-Pd_{core}/C was twice greater than the current from Pt/C with respect to the total metal mass (Fig. 3-21(a)) and about five times greater when only Pt mass was counted (Fig. 3-21(b)). It was apparent that the enhancement of activity of Pt_{shell}-Pd_{core}/C for O_2 reduction was achieved even though platinum content was reduced to about one-sixth of Pt/C (40 wt% of Pt). In conclusion, the electro-catalyst, prepared by ELD of Cu and successive displacement by Pt, was kinetically superior for ORR to the conventional Pt/C due to faster kinetics of hydrogenation reaction of oxygen-containing species. The method enabled the synthesis of highly dispersed Pt catalyst with small content. The mass-specific activity also assured the enhancement of activity of Pt_{shell}-Pd_{core}/C.

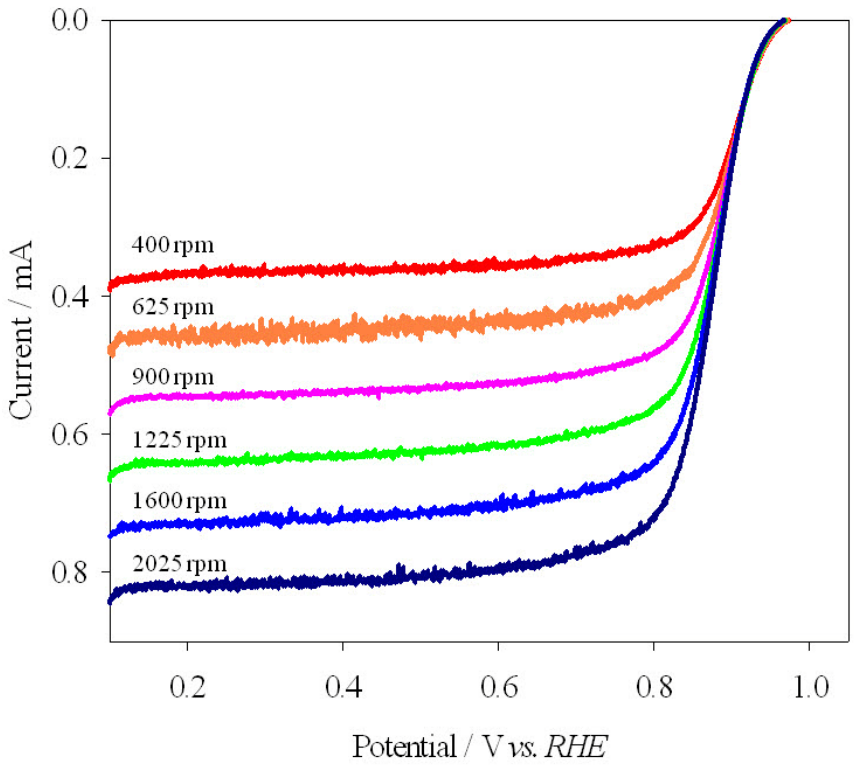

Fig. 3-15. Polarization curves for ORR with different rotating rates on Pt_{shell}-Pd_{core}/C in 0.2 M $HClO_4$ solution; sweep rate 0.5 mV/s; cathodic sweep.

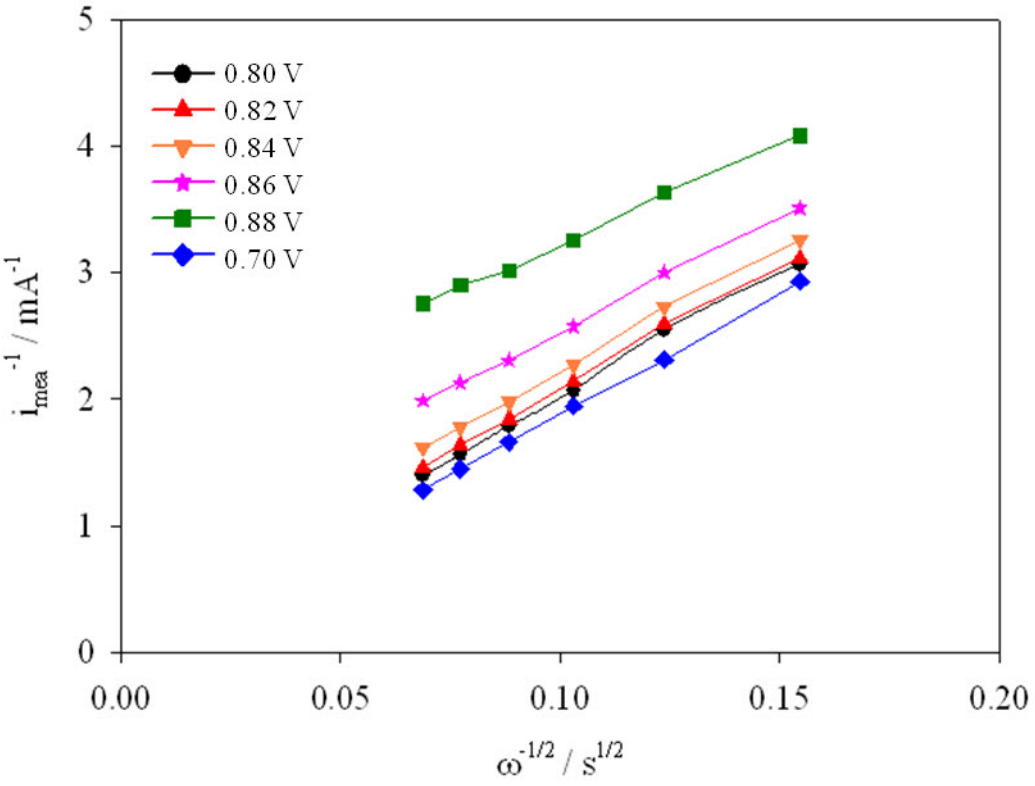

Fig. 3-16. Parallel straight lines seen in Koutecky-Levich plots at potentials in the mixed kinetic-diffusion region.

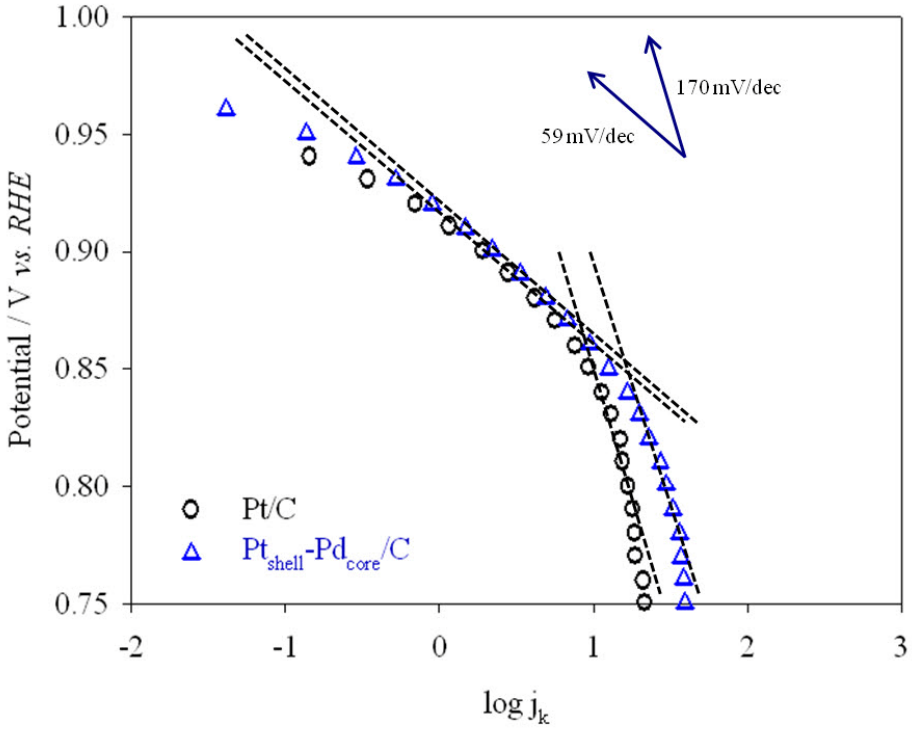

Fig. 3-17. Tafel plots obtained from kinetic current density (j_k) for commercial Pt/C (circle, black) and for Pt_{shell}-Pd_{core}/C (triangle up, blue).

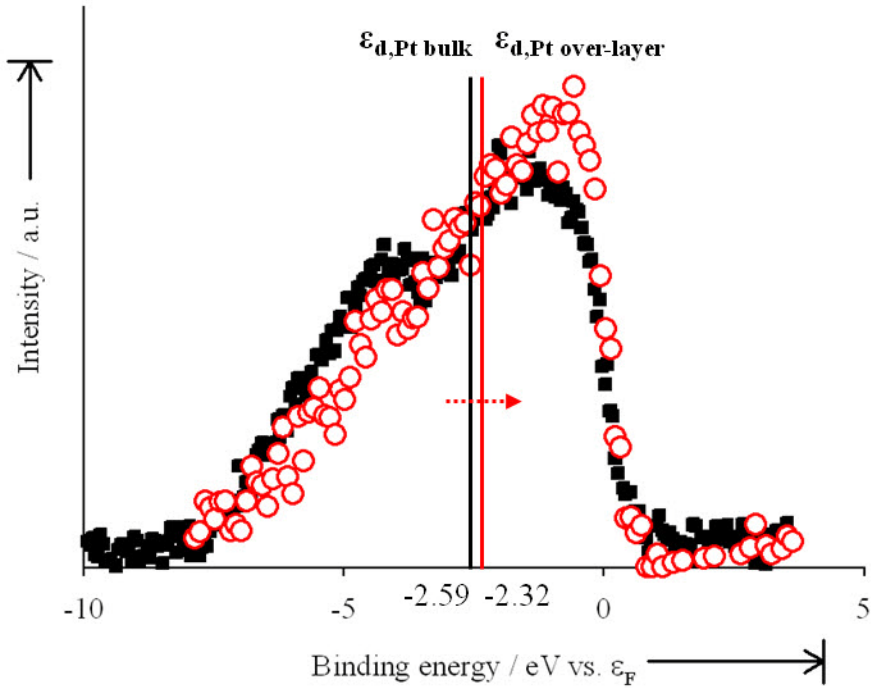

Fig. 3-18. The position of ε_d, d-band center with respect to ε_F of Pt over-layer in Pt/C (square, black) and Pt_{shell}-Pd_{core}/C (circle, red).

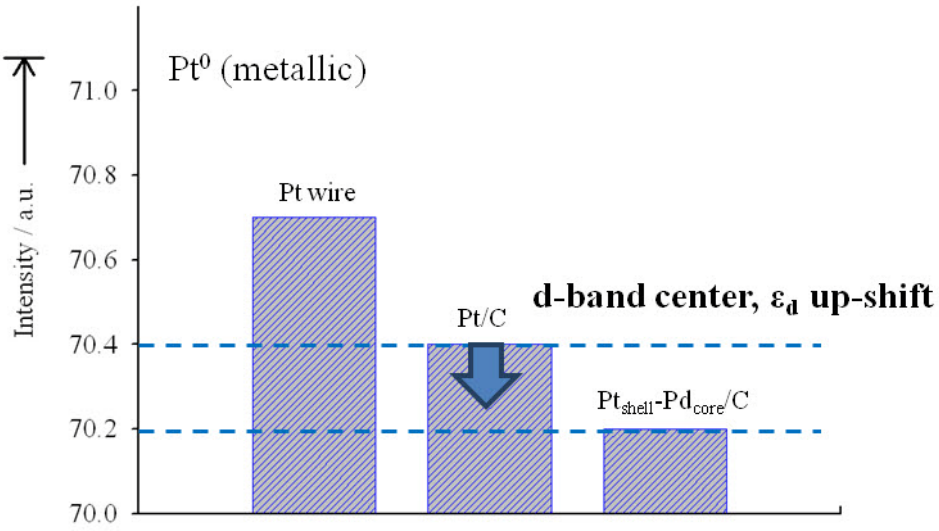

Fig. 3-19. The shift of core-level binding energy of Pt obtained from XPS $4f_{7/2}$ of Pt wire, commercial Pt/C, and Pt_{shell}-Pd_{core}/C.

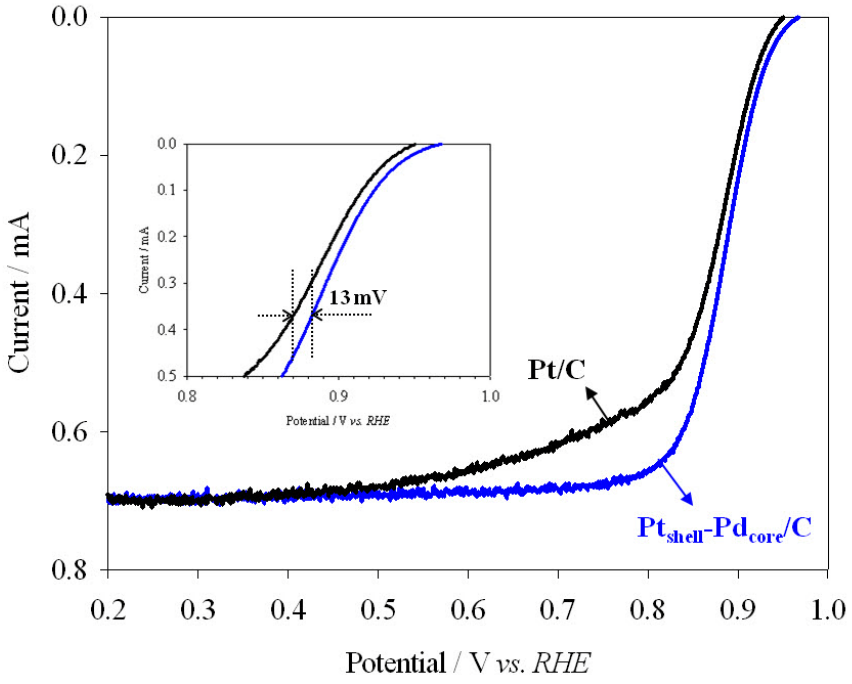

Fig. 3-20. Polarization curves for ORR on Pt/C and Pt_{shell}-Pd_{core}/C in 0.2 M $HClO_4$; sweep rate 0.5 mV/s; cathodic sweep; $E_{1/2}$ of Pt_{shell}-Pd_{core}/C is higher than $E_{1/2}$ of Pt/C by 13 mV (inset image).

(a)

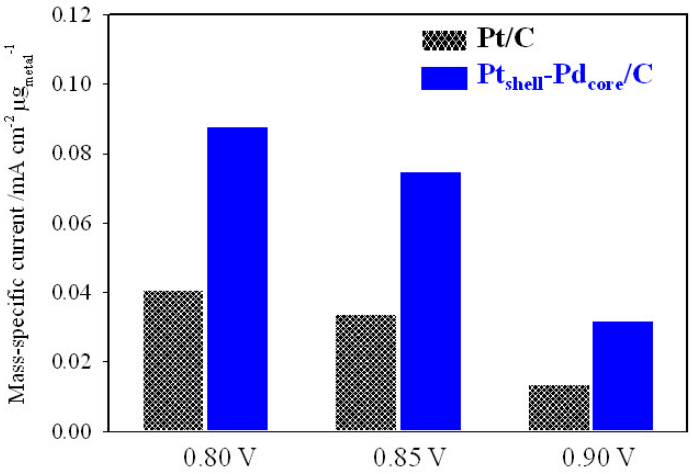

(b)

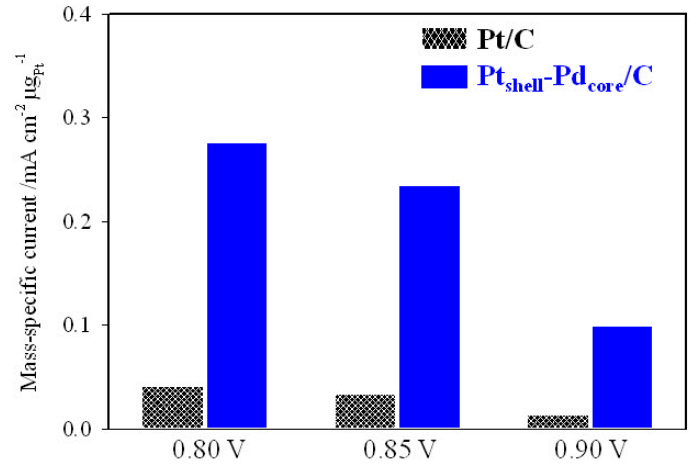

Fig. 3-21. The mass-specific activities of Pt/C and Pt_{shell}-Pd_{core}/C; current was divided by geometrical electrode area and (a) total metal mass and (b) Pt.

3-3-2. Single-Cell Experiment

The MEA, fabricated with Pt_{shell}-Pd_{core}/C catalyst on the cathode GDL, was tested by fuel cell station. The target metal loading was approximately 0.24 mg_{Pt+Pd}/cm^2 and 0.07 mg_{Pt}/cm^2 for cathode, and 0.2 mg_{Pt}/cm^2 for anode, respectively. Fig. 3-22 presented the polarization curves and the power density curves for MEA-Pt/C and MEA-Pt_{shell}-Pd_{core}/C. Open circuit voltage (OCV), 0.6 V- power density, and maximum power density of both MEAs were summarized in Table 3-1. Compared to the MEA with commercial Pt/C catalyst, MEA-Pt_{shell}-Pd_{core}/C possessed little lower OCV. Higher OCV and operating potential were expected from MEA-Pt_{shell}-Pd_{core}/C, because more facile oxygen reduction over Pt_{shell}-Pd_{core}/C catalyst was observed from previous half-cell experiment. Unfortunately, it turned out that the superior activity of Pt_{shell}-Pd_{core}/C was not realized by single-cell experiment. This discrepancy between half-cell and single-cell experiment must be resolved by further study (Appendix B.)

Table 3-1. OCV and Power Density of MEA-Pt/C and MEA-Pt_{shell}-Pd_{core}/C from Single-Cell Experiment

	MEA-Pt/C	MEA-Pt_{shell}-Pd_{core}/C
OCV / V	0.960	0.912
0.6 V-power density / W cm^{-2}	0.439	0.351
Max. power density / W cm^{-2}	0.590	0.585

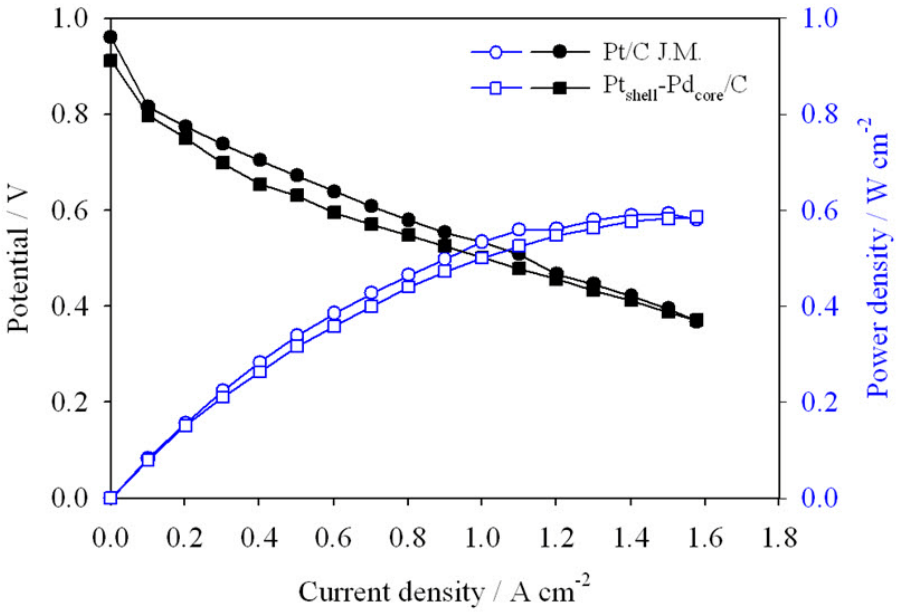

Fig. 3-22. I-V curves (black, filled) and power density (blue, vacant) curves for Pt/C (circle) and for Pt_{shell}-Pd_{core}/C (square) catalyst from single-cell experiment.

CHAPTER IV

Pt_{shell}-Pd_{core}/C for Electro-Oxidation of Methanol

4-1. Catalytic Activity of Pt_{shell}-Pd_{core}/C

The activity improvement of anode catalysts in DMFC, another type of fuel cell under the sub-category of PEMFC, is helpful to reduce fuel permeation through electrolyte [1,9]. Pt has been demonstrated as the only active and stable noble metal for alcohol oxidation, particularly in acid medium. However, it is well known that pure Pt is readily poisoned by CO-like intermediates of methanol (MOR) or ethanol electro-oxidation reaction (EOR) [1,9,98-101]. Methanol or ethanol oxidation on Pt is only possible at potentials where adsorbed CO and other poisoning intermediates are effectively oxidized, leading to a significant over-potential and hence loss in efficiency. A higher efficiency at more negative potentials was obtained for PtRu catalysts [98-101], which was generally attributed to their superior CO_{ad}-tolerance due to bi-functional effect. On PtRu catalyst, CO_{ad} was oxidized by OH_{ad} species, which was readily formed on Ru surface atoms by water splitting process. A number of other catalyst systems have been investigated for their suitability as MOR catalysts including Pt-based alloy catalysts other than PtRu; Pt–Sn [102–104], Pt–Pd [105,106], Pt–Rh [107], Pt–Mo [108]. The complete electro-oxidation of methanol involves letting 6 electrons out per methanol molecule. More active electro-catalysts are needed to promote methanol electro-oxidation with lower activation barrier, related to both

of C–C bond cleavage, and removal of adsorbed intermediates and products, formed during electro-oxidation of methanol. Pd has been a very good electro-catalyst for organic fuel electro-oxidation [109]. While voltammetry has indicated stronger CO_{ad} bonding on Pd_{4p} was predicted [110]. Another study [111] showed that the release of hydrogen, occluded in Pd, may provide a viable route for lowering the surface concentration of adsorbed CO. The Pt–Pd bimetallic system also exhibits a high resistance against CO_{ad}-poisoning from the oxidation of formic acid [112].

4-1-1. Methanol Oxidation by Half-Cell Experiment

The electro-oxidation of MeOH was attempted by using as-prepared Pt_{shell}-Pd_{core}/C catalyst at room temperature. Pt, of course, is the most active catalyst in ORR as well as in MOR. The promoting effect of Pd substrate, and electronic effect induced by strained Pt over-layer were expected from Pt_{shell}-Pd_{core}/C. The CV results in 0.5 M H_2SO_4 + 0.5 M MeOH for Pt_{shell}-Pd_{core}/C and commercial Pt/C were compared in Fig. 4-1. The measured currents were transformed into mass-specific current; Pt+Pd for Pt_{shell}-Pd_{core}/C and Pt for Pt/C. A broad peak near at 0.2 V corresponded to the desorption of adsorbed H atom on Pt surface (Pt-H + CH_3OH → Pt-CH_3OH_{ad} + H^+) and the dissociative adsorption of CH_3OH (Pt-$CH_{(3-n)}OH$ → $_nH^+$ + ne^+, Faradaic process). Since methanol was not able to displace adsorbed H atoms, adsorption could only begin at potentials where enough Pt sites became free from H [113]. That was why the oxidation current appeared at 0.2 V. The oxidation of adsorbed intermediate species ($CH_{(3-n)}OH_{ad}$ or CO_{ad}) to CO_2 started at 0.5 V and continued until 0.8 V. In this potential range, the dissociation of H_2O also took place ($H_2O(aq)$ → H_2O_{ad}, H_2O_{ad} → OH_{ad} + H^+ + e^-. At potential over than 1.0 V, methanol oxidation proceeded on the surface of Pt oxide. In this region, OH was strongly bonded to Pt leading to a decline of current density. Another oxidation current was observed during cathodic sweep. The peak was associated with the renewed oxidation on surface of the reduced Pt oxide, and re-oxidation of the intermediates species, still adsorbed on the catalyst surface. It should be noted that the oxidation of MeOH took place on $Pt_{shell}Pd_{core}$/C

at slightly higher potential than Pt/C, which reflected greater activation energy (E_a) for the reaction occurring at 0.4 V on $Pt_{shell}Pd_{core}$/C. However, the mass-specific current for MOR from $Pt_{shell}Pd_{core}$/C was higher than the current from Pt/C at potential above 0.7 V, which in turn showed faster kinetic of the reaction on the Pt over-layer in Pt_{shell}-Pd_{core}/C. In conclusion, the electro-oxidation of MeOH on Pt_{shell}-Pd_{core}/C and Pt/C showed different behavior according to the reaction potential. The details of potential-dependent reaction over Pt_{shell}-Pd_{core}/C and its comparison to Pt/C will be addressed in the later paragraph. When the activity was transformed with Pt-mass content, however, the catalytic activity of Pt_{shell}-Pd_{core}/C was higher by a factor of 3.5~4 (not shown here).

The long-term stability and catalytic activity of Pt_{shell}-Pd_{core}/C was observed by chronoamperommetry (CA) experiment carried out in 0.5 M H_2SO_4 + 0.5 M MeOH at 293 K. The oxidation current was recorded at 0.5 V (vs. NHE) for 1800 s as shown in Fig. 4-2. Pt/C showed rapid decrease in the current, while the current decay of Pt_{shell}-Pd_{core}/C was relatively small, and approached to slightly higher current. The decrease in mass-specific current is ascribed to CO_{ad}-poisoning on the active site of the catalyst surface. Therefore, the result indicated that Pt_{shell}-Pd_{core}/C was less vulnerable to CO_{ad}-poisoning than Pt/C. The stability of Pt_{shell}-Pd_{core}/C was also supported by multiple CV experiment as shown in Fig. 4-3. The MOR was conducted with Pt_{shell}-Pd_{core}/C and Pt/C over 100^{th} cycles with 50 mV/sec. The oxidation current of Pt/C continuously decreased, whereas the current from Pt_{shell}-Pd_{core}/C was maintained according to cycle numbers. The forward peak current was normalized in Fig. 4-4. Pt_{shell}-

Pd_{core}/C maintained its peak current as high as 95% of initial value, which was significantly greater than Pt/C (85%). Consequently, Pt_{shell}-Pd_{core}/C showed better performance than Pt/C in terms of electrochemical stability. The less CO_{ad}-poisoning of Pt_{shell}-Pd_{core}/C was caused by the modified surface activity of Pt over-layer toward adsorbate, which was already confirmed by previous chapter. Because of the up-shift in ε_d, the surface Pt had a tendency to bind less stronger than pure Pt. For that reason, the intermediate species were weakly adsorbed on Pt over-layer. This meant, in turn, that the dissociative adsorption was not readily accomplished over Pt over-layer, and the activation barrier for adsorption became high. Therefore, more active Pt site could be reserved at an expense of catalytic activity. It could explain why the catalytic activity of Pt_{shell}-Pd_{core}/C was lower at potential below 0.7 V, where dissociate adsorption of MeOH was dominant. The increased stability of Pt_{shell}-Pd_{core}/C could be also explained by the formation of OH_{ad} during MOR. The adsorbed CO_{ad} can be removed through the oxidation by OH_{ad} ($CO_{ad} + OH_{ad} \rightarrow COOH_{ad} \rightarrow CO_2 + H^+ + e^-$; combination reaction). Therefore, it was necessary to generate OH_{ad} to donate the second oxygen atom to CO_{ad} for the complete oxidation to CO_2. These OH_{ad} could be formed by splitting H_2O on the metal surface along with adsorption of MeOH, but at slightly higher potential. The formation of OH_{ad} on pure Pt was difficult, and relatively high positive potential ($E > 0.55$ V) was needed to activate H_2O_{ad}. On Pt_{shell}-Pd_{core}/C, however, the formation of OH_{ad} was more facile as evidenced by CV results in 0.5 M H_2SO_4. As seen in Fig. 4-5, the formation of OH_{ad} occurred at more negative potential (lower E_a) with higher anodic current. Though OH_{ad} was easily formed, the bond strength of Pt-

OH_{ad} was not high due to the tuned surface property of Pt over-layer. Therefore, loosely bounded CO_{ad} could diffuse to Pt-OH_{ad}, and final product could be easily desorbed from Pt surface after the combination reaction. The lower E_a for water splitting and lower combination energy in Pt-M electrode has been also reported from other studies [114]. The enhancement of MOR on Pt_{shell}-Pd_{core}/C was emphasized at potential over 0.7 V, because the rate determining step (RDS) in MOR was not the adsorption of MeOH, but rather the electro-oxidation of adsorbed species [115-117]. In other words, the modified Pt over-layer affected to the latter with more extent than the former process. In summary, the enhanced stability of Pt_{shell}-Pd_{core}/C was more influenced by the improved kinetics of OH_{ad} formation and the subsequent oxidation of CO_{ad} by OH_{ad} through the combination reaction.

The comparison of RDS and the reaction E_a was done by driving Tafel plots with different reaction temperature. The Tafel plots for methanol oxidation were obtained from quasi-steady polarization by performing potential sweeping with slow scan rate, 5 mV/s (Fig. 4-6). The oxidation current in a forward sweep rose by a factor of 2~3 as the temperature increased. It indicated that temperature had a positive effect on MOR, leading to faster reaction kinetics, and to the delayed deactivation of the catalyst surface by CO_{ad}-poisoning. To be specific, the CO_{ad} oxidation, either by electron transfer or the combination reaction, was accelerated on the thermally activated surface. In the case of MOR, Tafel plot does not carry its fundamental meaning as in the literature as a straight line in E vs. log j was hardly obtained [115]. It was ascribed to the mixed contribution of adsorption of different intermediate through multiple

oxidation reaction and electronic transfer as limiting steps. However, it has been reported that the Tafel slope for MOR was 180~195 mV/dec at bulk PtRu alloy [118] and carbon-supported PtRu [119]. Generally it ranged from 60 mV/dec to 200 mV/dec in acidic electrolyte. Tafel plots derived from the polarization curves for different temperatures were given in Fig. 4-7. As it was expected, the linear region is not wide, thus the Tafel slope in the potential of interest could be derived from approximation. It seemed reasonable to state the Tafel slope for MOR was about 103.4 mV/dec and 166.7 mV/dec on Pt_{shell}-Pd_{core}/C and Pt/C, respectively at 293 K. The variation of the Tafel slope of Pt_{shell}-Pd_{core}/C is from 78.1 mV/dec to 103.4 mV/dec, and from 100.3 mV/dec to 166.7 mV/dec for Pt/C. Fig. 4-8 showed the pseudo-Arrhenius plots for the current densities of the MOR on Pt_{shell}-Pd_{core}/C and Pt/C. Almost linear correlation between log j and 1/T was maintained at all potentials, indicating that reactions on both catalysts were governed by same mechanism. The apparent activation energy (E_{app}) was calculated from the slope of these plots. In E = 0.56 V ~ 0.62 V, the E_{app} was approximately 62.97 kJ/mol on Pt_{shell}-Pd_{core}/C and 45.00 kJ/mol on Pt/C. The values were close to what has been reported from other studies [120-122]. As explained, the dissociative adsorption of MeOH and its intermediate is dominant in this region. Therefore, the less activity of Pt_{shell}-Pd_{core}/C than Pt/C in this potential could be well understood. When we focus the potential range of E = 0.72 ~ 0.78 V, where water splitting and the combination reaction were dominant, E_{app} was reduced on Pt_{shell}-Pd_{core}/C (45.46 kJ/mol for Pt_{shell}-Pd_{core}/C and 48.61 kJ/mol for Pt/C). The decrease in E_{app} in this region indicated that the kinetic of the combination reaction was improved by Pt_{shell}-Pd_{core}/C.

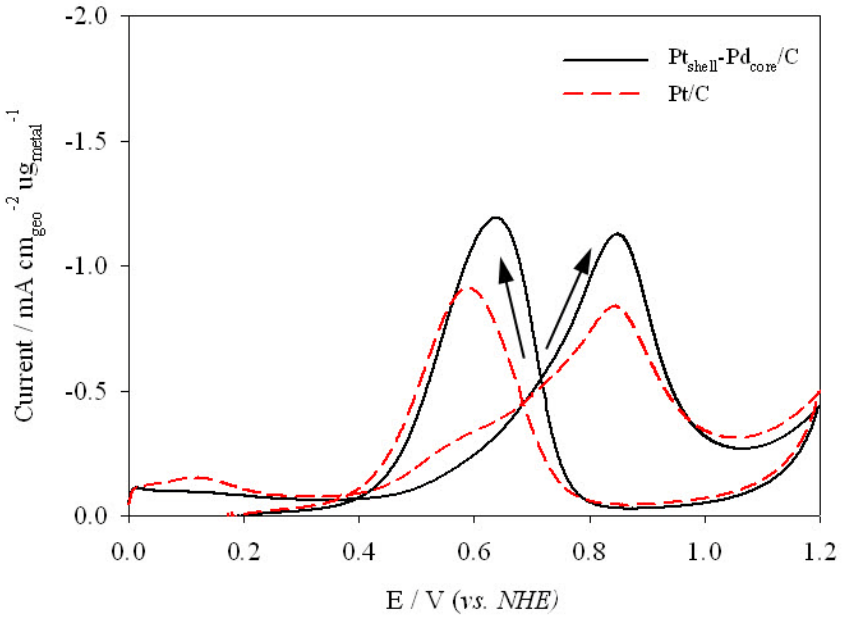

Fig. 4-1. CV results of Pt_{shell}-Pd_{core}/C (solid line, black) and Pt/C (dotted line, red) in 0.5 M H_2SO_4 + 0.5 M MeOH; sweep rate 50 mV/s at 293 K.

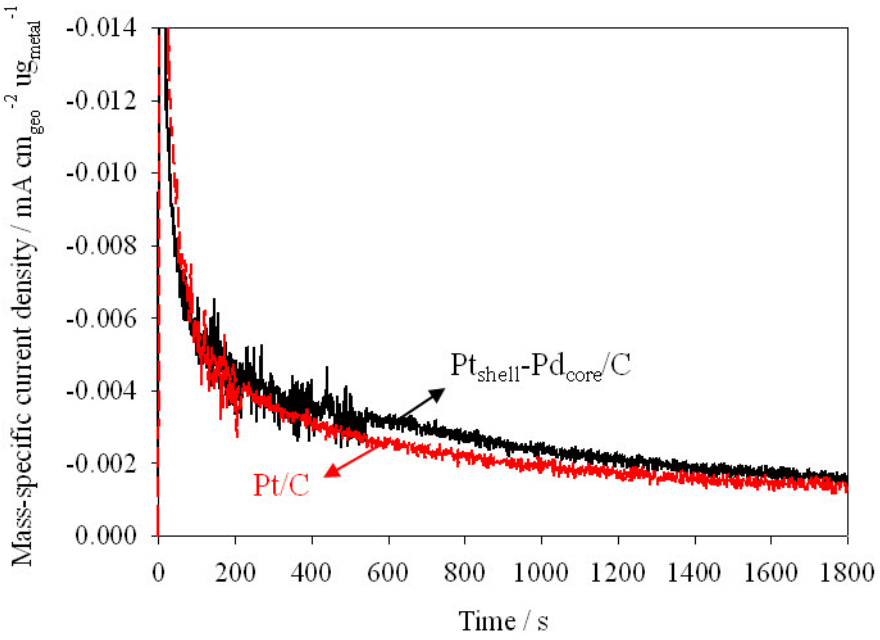

Fig. 4-2. Chronoamperommetry of Pt_{shell}-Pd_{core}/C (solid line, black) and Pt/C (dotted line, red) in 0.5 M H_2SO_4 + 0.5 M MeOH at 0.5 V (vs. NHE).

(a)

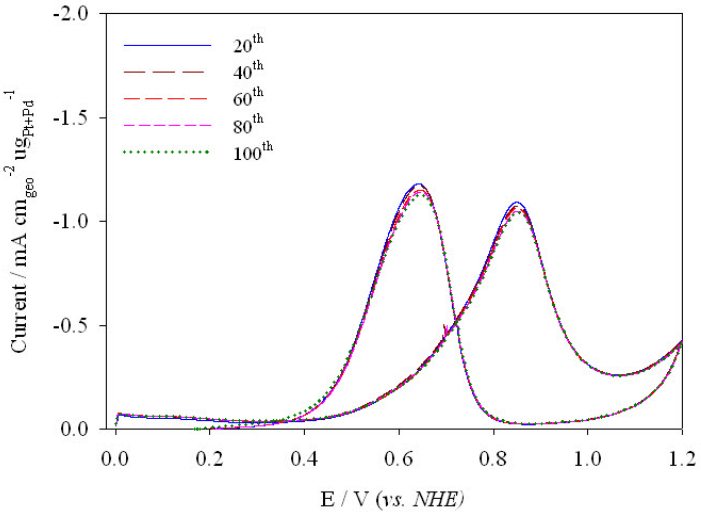

(b)

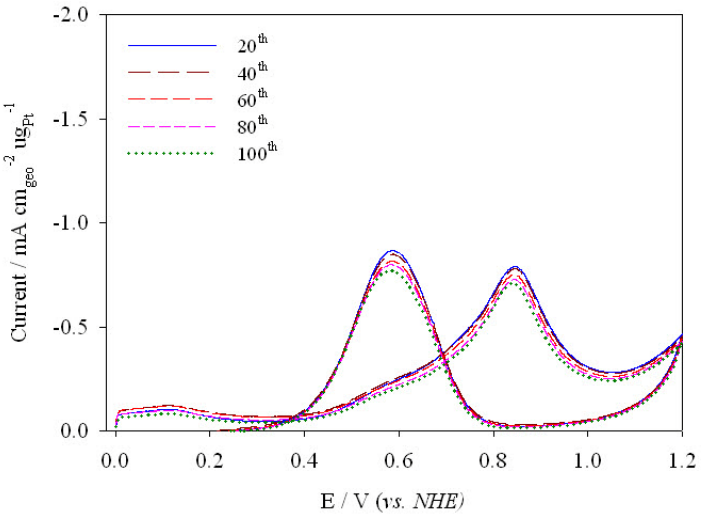

Fig. 4-3. Accumulated CV results up to 100th cycle of (a) Pt_{shell}-Pd_{core}/C and (b) Pt/C; sweep rate 50 mV/s at 293 K.

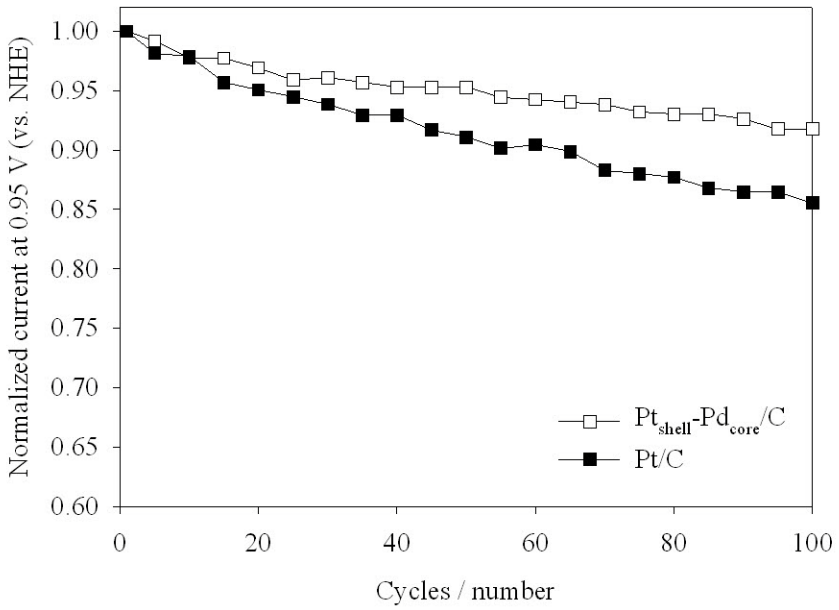

Fig. 4-4. Normalized peak current density of Pt_{shell}-Pd_{core}/C (vacant) and Pt/C (filled) obtained from Fig. 4-3.

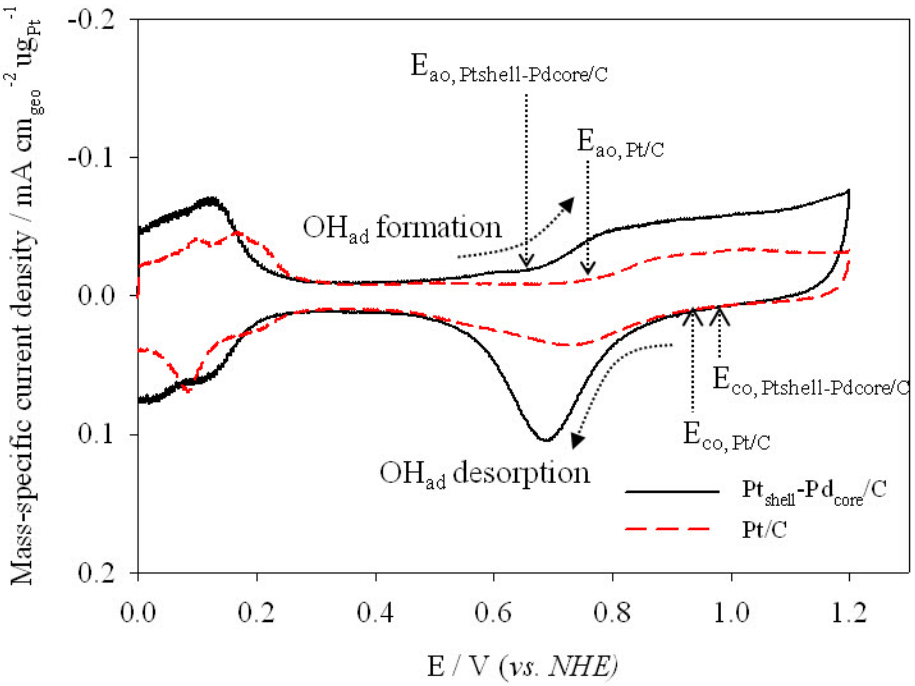

Fig. 4-5. CV results (Pt mass-specific current density as a function of potential) of Pt_{shell}-Pd_{core}/C (solid line, black) and Pt/C (dotted line, red); E_{ao} = on-set potential of OH_{ad} formation, E_{co} = on-set potential for OH_{ad} desorption.

(a)

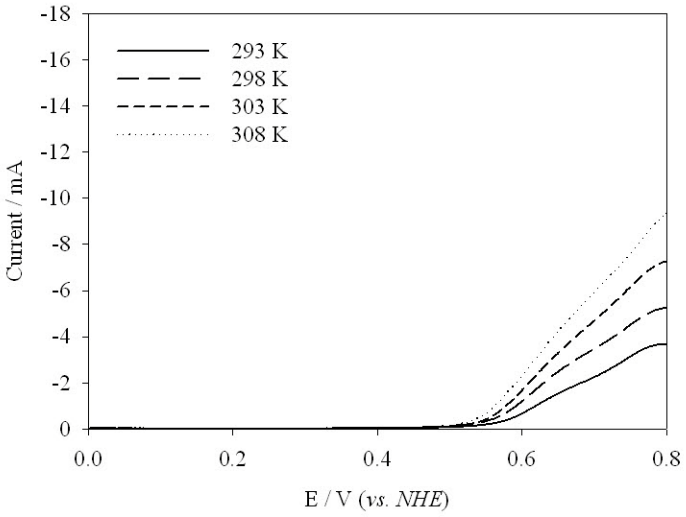

(b)

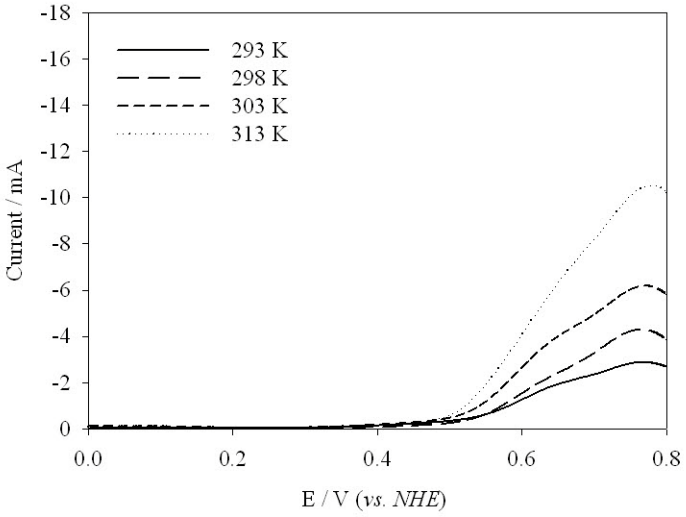

Fig. 4-6. Quasi-steady polarization by performing potential sweeping with 5 mV/s at different temperature; (a) Pt_{shell}-Pd_{core}/C (293 K ~ 308 K) and (b) Pt/C (293 K ~ 313 K).

(a)

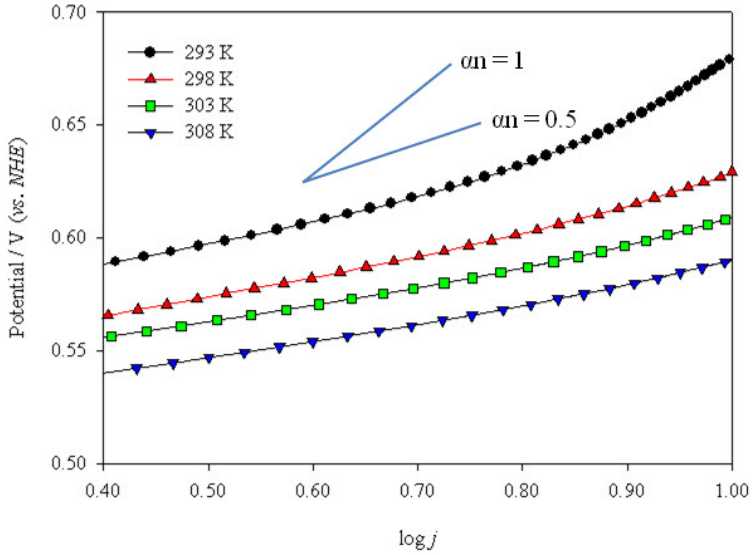

(b)

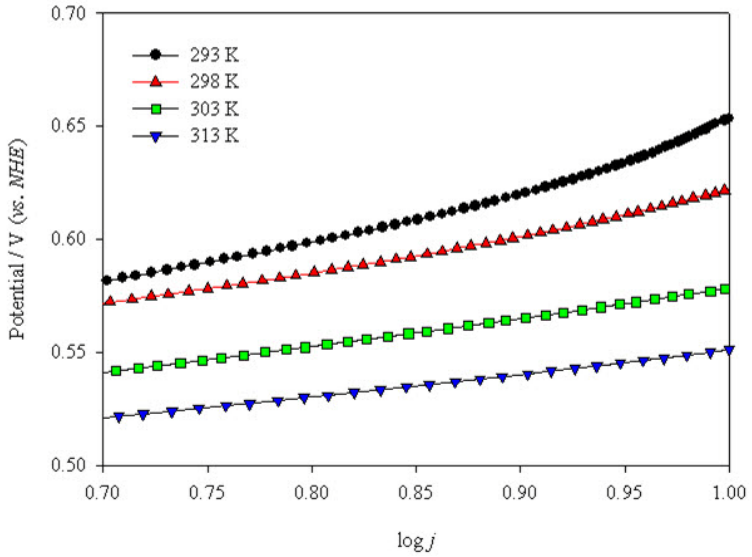

Fig.4-7. Tafel plots for MOR on (a) Pt_{shell}-Pd_{core}/C and (b) Pt/C in low potential region (0.56 V ~ 0.62 V) from different temperature (obtained from Fig. 4-6).

(a)

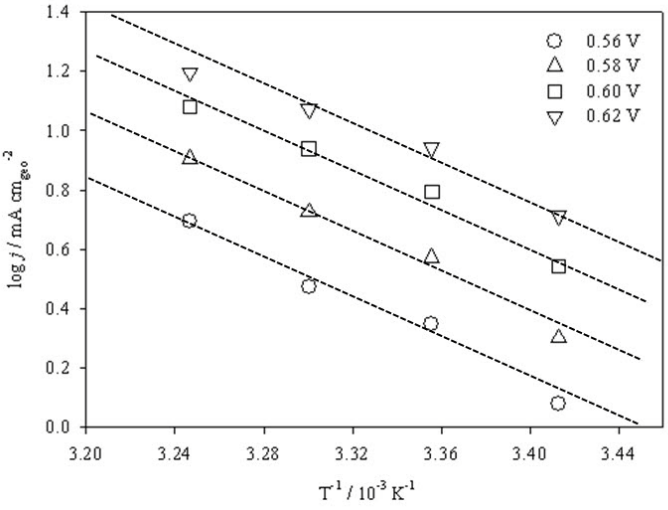

(b)

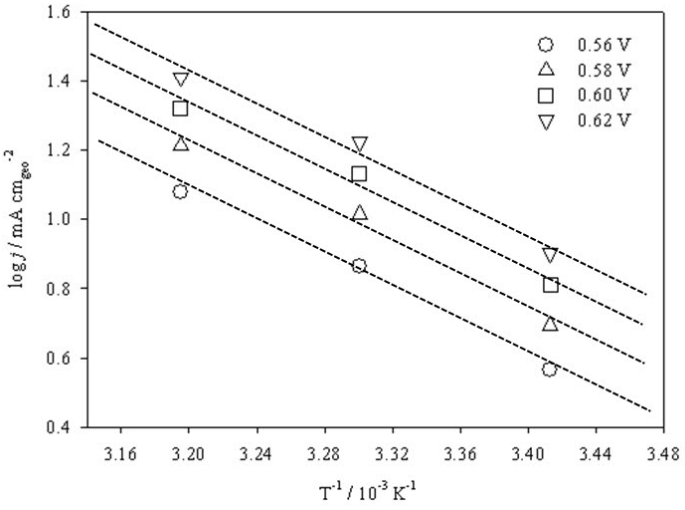

Fig. 4-8. Arrhenius plots for the current densities (log j vs. T^{-1}) of the MOR on (a) Pt_{shell}-Pd_{core}/C and (b) Pt/C in low potential region (0.56 V ~ 0.62 V).

(a)

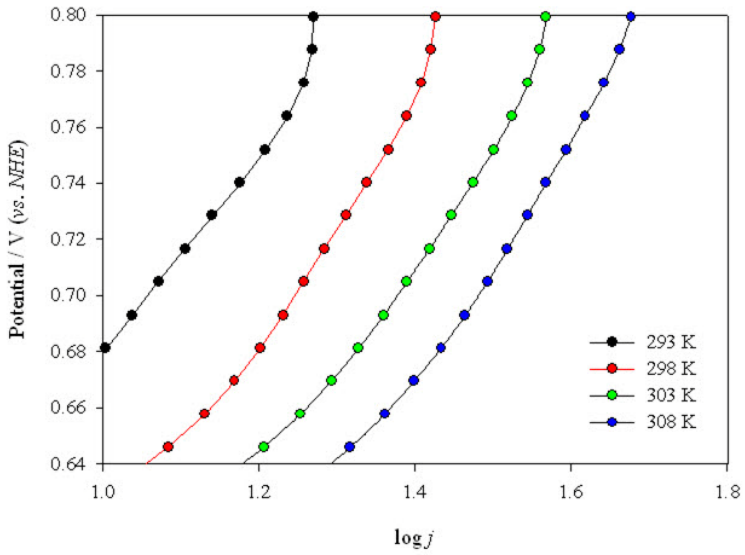

(b)

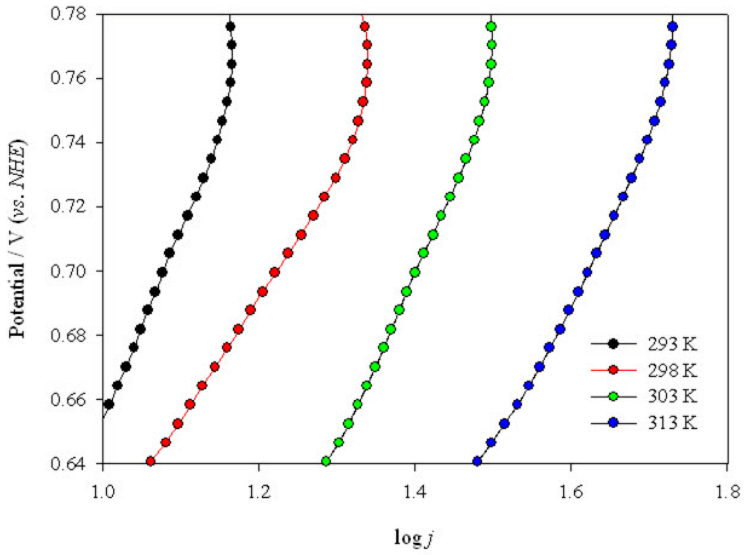

Fig. 4-9. Tafel plots for MOR on (a) Pt_{shell}-Pd_{core}/C and (b) Pt/C in high potential region (0.72 V ~ 0.78 V) from different temperature (obtained from Fig. 4-6).

(a)

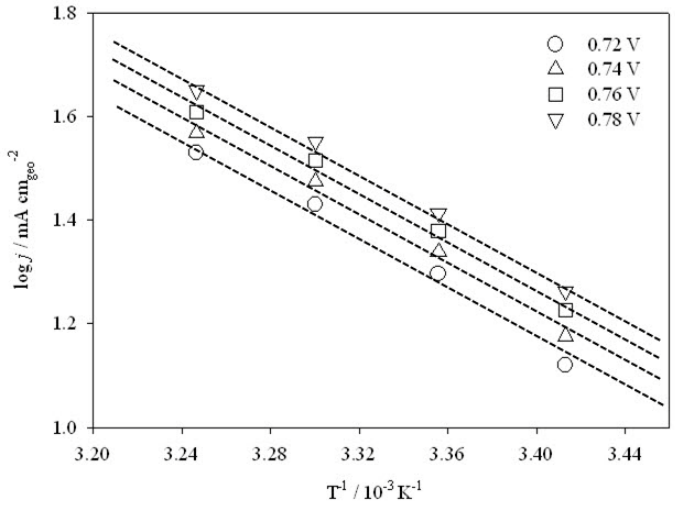

(b)

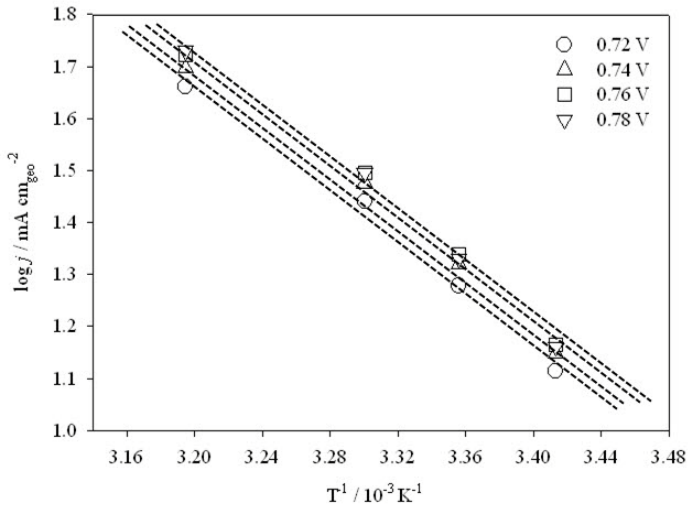

Fig. 4-10. Arrhenius plots for the current densities (log j vs. T^{-1}) of the MOR on (a) Pt_{shell}-Pd_{core}/C and (b) Pt/C in low potential region (0.72 V ~ 0.78 V).

4-1-2. Carbon Monoxide Stripping

The electrochemical oxidation of adsorbed CO on Pt_{shell}-Pd_{core}/C and Pt/C was performed by CO_{ad}-stripping experiment. It should be noted that the charge associated with double layer charging and metal oxide formation must be eliminated from the obtained CV, in order to calculate the charge contribution solely from CO_{ad} oxidation; i.e. using second cycle in the same experiment for the base line subtraction. The result of CO_{ad}-stripping of Pt_{shell}-Pd_{core}/C and Pt/C, and their comparison was given in Fig. 4.11 On-set potential for CO_{ad} desorption on Pt_{shell}-Pd_{core}/C was more negative than on Pt/C by 45 mV. Considering that the electro-oxidation of adsorbed CO was initiated by formation of OH_{ad} via water splitting on the catalyst surface, the result indicated that OH_{ad} was more readily formed on Pt_{shell}-Pd_{core}/C surface. The easy formation of OH_{ad} was supported by lower E_{app}. High oxidation current observed in Pt/C meant commercial Pt was more susceptible to adsorption of CO_{ad}, leading to CO_{ad}-poisoning and early deactivation compared to Pt_{shell}-Pd_{core}/C.

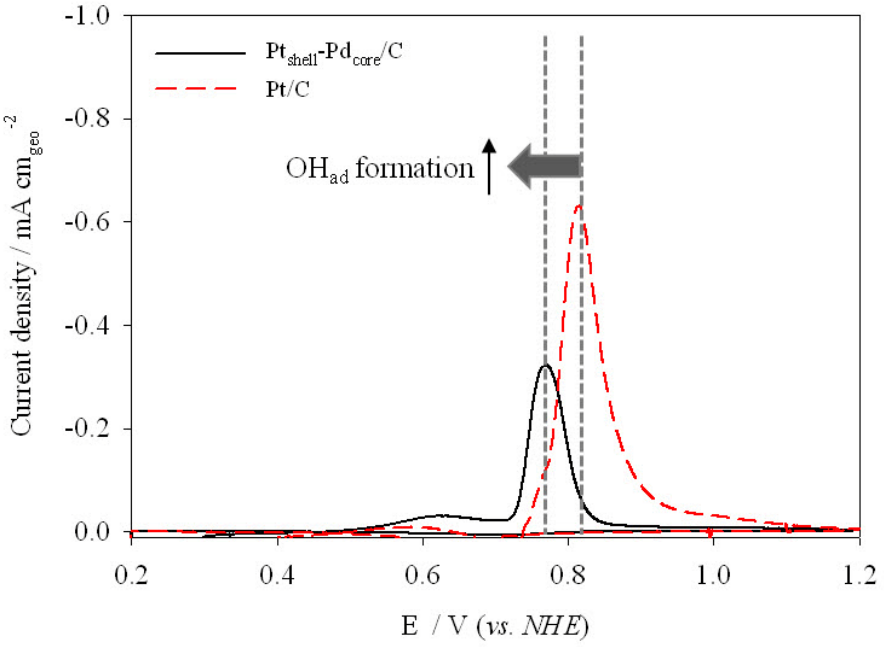

Fig. 4-11. CO_{ad}-stripping results of Pt_{shell}-Pd_{core}/C (solid line, black) and Pt/C (dotted line, red); sweep rate 10 mV/s at 293 K.

CHAPTER V

Pt-Deposited SiO_2/C Electro-Catalyst under Low Humidity

5-1. Preparation of Pt-Deposited SiO_2/C

The SiO_2 nanoparticles were synthesized by micro-emulsion method. As seen in FE-SEM image of Fig. 5-1(a), the SiO_2 nanoparticles were spherical and highly dispersed. The average diameter of the mono-dispersed SiO_2 nanoparticles was measured from the FE-SEM images, and it was 46 nm with a standard deviation of ±2 nm. TEM was also employed to analyze the SiO_2 nanoparticles as shown in Fig. 5-1(b). Direct Pt deposition was attempted by irradiating ultrasound to the bath, which contained Pt precursor and as-prepared SiO_2 nanoparticles. TEM image of Pt-SiO_2 was given in Fig. 5-1(c). The Pt nanoparticles were formed on the surface of SiO_2 as a result of ultrasound irradiation.

The mechanism of mono-metallic synthesis by ultrasound was proposed, which were water sonolysis and the subsequent radical formation [80,81,83]. Okitsu et al. worked on the preparation of Ag, Au, and Pt under ultrasound irradiation. They found four pathways were available. First, the water molecule dissociated into hydrogen radical (H•) and hydroxyl radical (OH•) by water sonolysis according to Eq. 5-A. Then, the radicals reacted with M cations to form metal particles, M^o via Eq. 5-B. Furthermore, the direct reaction of M cations with water in the interfacial region between the cavitation and liquid led to the formation of M^o as referred by

Eq. 5-C. In this experiment the reduction of Pt followed these two pathways. On the other hand, if there existed a protective agent, such as an alcohol, during sonolysis, the secondary radical R• would be formed via de-protonation of RH by OH• or H•. Then, R• contributeed to form M^o by another route (from Eq. 5-D to Eq. 5-E).

(Eq. 5-A) $H_2O \rightarrow H\bullet + OH\bullet$

(Eq. 5-B) $M^{n+} + nH\bullet \rightarrow (M^o) + nH^+$

(Eq. 5-C) $M^{n+} + nH_2O \rightarrow (M^o) + nOH\bullet + nH^+$

(Eq. 5-D) $RH + OH\bullet(H\bullet) \rightarrow R\bullet + H_2O\ (H_2)$

(Eq. 5-E) $M^{n+} + nR\bullet \rightarrow (M^o) + nH^+ + nR'$

The size of Pt nanoparticles was measured by manual counting (count number = 100) from the TEM image in Fig. 5-1(c), and the mean diameter of Pt nanoparticle was approximately 1.4 nm. The size distribution (± 0.22 nm) was narrow as it was supported by the particle size histogram in Fig. 5-1(d). The particle size was closely related to the amount of Pt ions and the amount of surfactant. As the concentration of Pt ions increased, the particle size became larger as seen in Fig. 5-1(e). However, extremely high concentration of Pt ions in the bath resulted in the homogenous formation of Pt nanoparticles (Fig. 5-1(f)).This indicated that the site for Pt formation on SiO_2 was no longer available when the concentration of Pt ions exceeded the critical value.

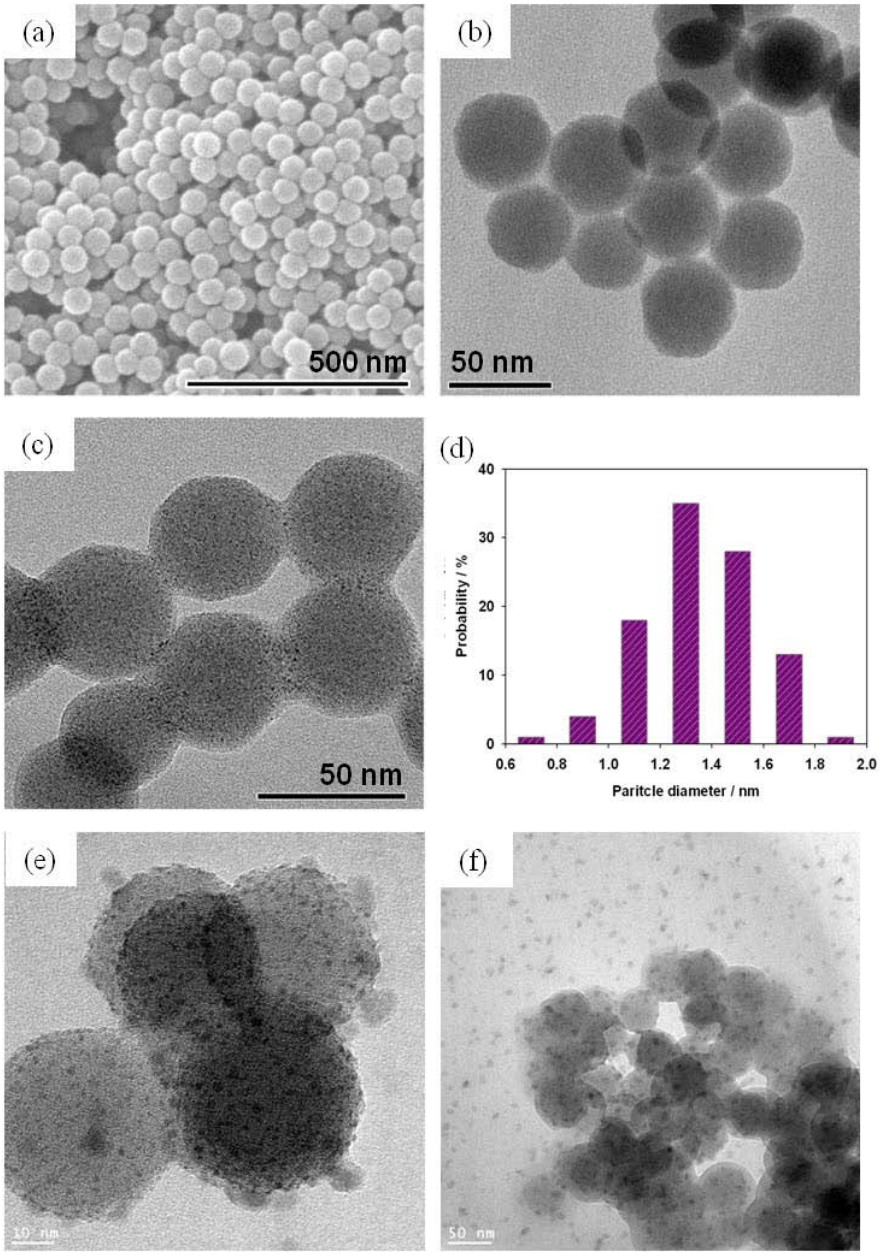

Fig. 5-1. (a) FE-SEM and (b) TEM images of SiO_2 nanoparticle, (c) TEM image of Pt-SiO_2 and (d) the histogram for Pt particle size distribution, and (e,f) TEM image of Pt-SiO_2 with high precursor concentration.

5-2. Characterization of Pt-Deposited SiO_2/C

The Pt nanoparticles on the SiO_2 surface was investigated by a HR-TEM analysis as shown in Fig. 5-2(a) ~ (c). The Pt nanoparticles seemed vivid by their contrast compared to the amorphous SiO_2. Moreover, the TEM image of Pt-SiO_2/C was displayed in 5-2(d). It was observed that Pt-SiO_2 nanoparticles were inter-connected by addition of conducting carbon. The deposition of Pt was assured by EDS analysis as shown in Fig. 5-3. The elemental mapping results proved that Pt was successfully loaded on SiO_2. One of the advantages of the sonochemical method was that it could uniformly assert the energy to the material. For this reason, the application of ultrasonic irradiation was extended to fabrication fuel cell material, such as carbon-supported metal catalyst and electrode. However, over the surface of carbon material, it was difficult to reduce metal ions uniformly due to its hydrophobic property, unless the surface was acidly pre-treated, thus having a lot of active sites for metal ion adsorption. Unlike carbon material, the Pt nanoparticles could be uniformly deposited on the surface of SiO_2, because SiO_2 possessed hydrophilic characteristics. In addition to that, it was revealed that the Pt nanoparticles possessed relatively small amount of surface oxide by XPS analysis, compared to commercial Pt/C catalyst. Therefore, the formation of Pt nanoparticle with high effective surface area and uniform dispersion was expected on SiO_2.

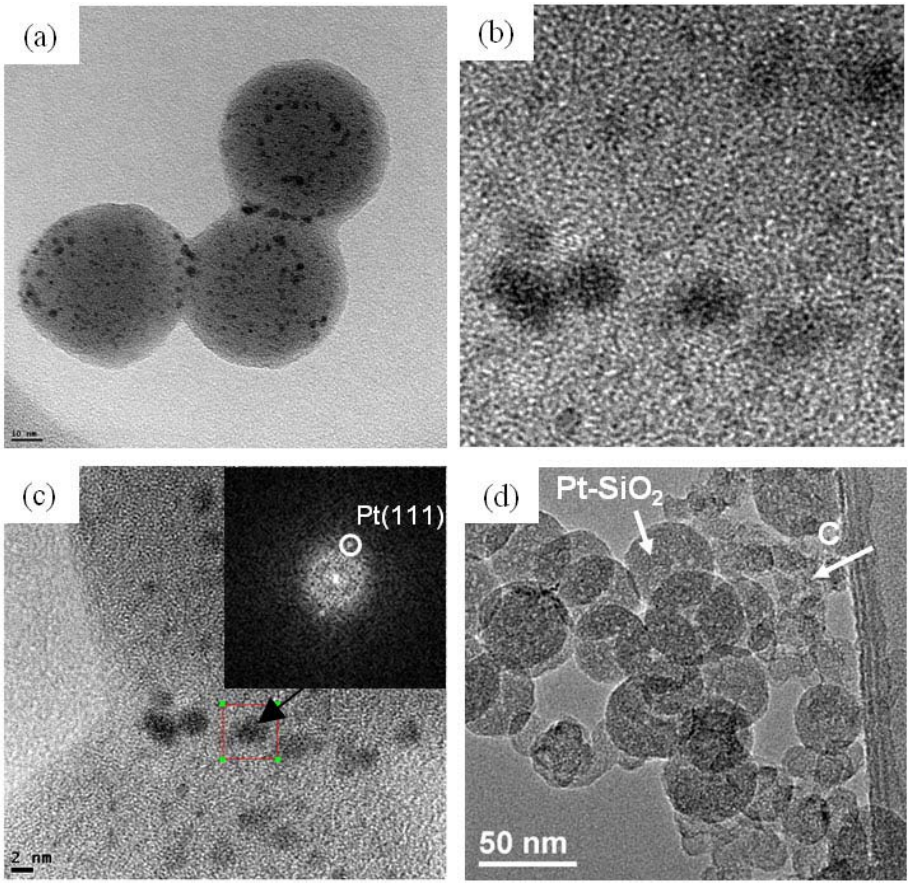

Fig. 5-2. (a) HR-TEM image of Pt-SiO_2, (b) Pt crystalline on SiO_2 by HR-TEM, (c) FFT of crystalline Pt, and (d) TEM image of Pt-SiO_2/C composite.

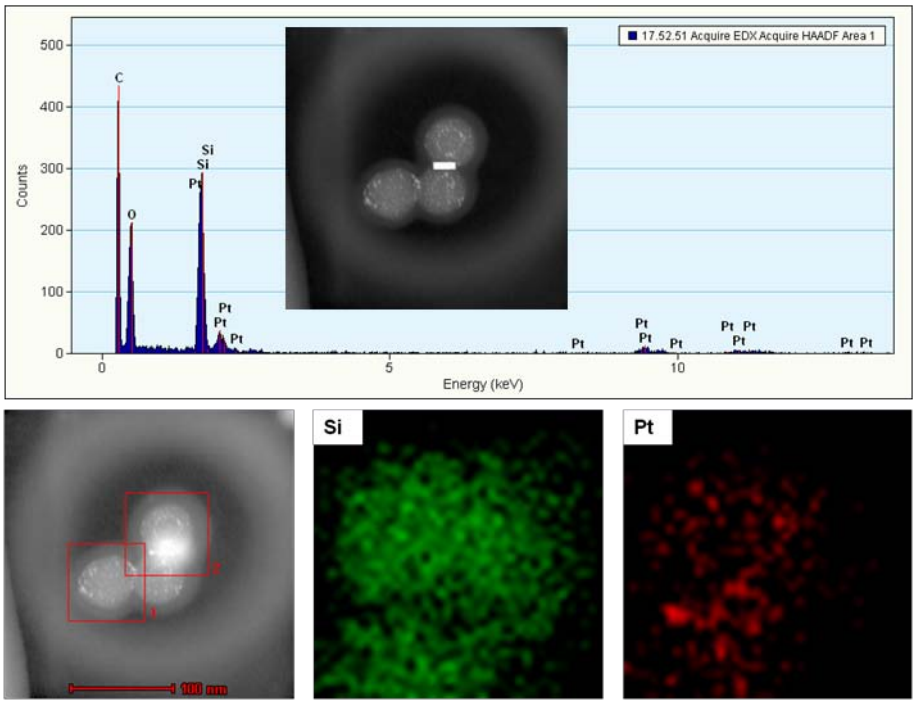

Fig. 5-3. EDS results of Pt-SiO_2 composite with elemental mapping of Si and Pt in Pt-SiO_2; square denoted with '2' indicated the selected region for analysis.

5-3. Electrochemical Performance of Pt-Deposited SiO_2/C

The electrochemical analysis was performed with rotating disk electrode. Ag/AgCl (3.5M, -0.205 V *vs*. NHE) was chosen as a reference electrode and Pt spring coil was used as a counter electrode. It was necessary to use carbon with Pt-SiO_2 composite, because the carbon served as a conducting agent. The catalyst layer only with Pt-SiO_2 was not catalytically active. Moreover, it was revealed, from the supplementary experiments, that the amount carbon affected the electrochemical activity of the composite catalyst. The potential sweep exhibited a cyclic voltammogram of Pt-SiO_2/C (Fig. 5-4). The oxidation of hydrogen that was adsorbed on Pt took place at E = 0.11 V ~ 0.3 V (vs. RHE). Pt oxide was formed as potential moved to 0.75 V. Through the cathodic sweep of potential, Pt oxide was then reduced, delivering reduction of molecular oxygen, which began at 0.95 V. At the end of polarization, H_{ad} was formed again. The electric double-layer was quite thicker than that shown from commercial Pt/C owing to the addition of SiO_2. The ECSA of Pt-SiO_2/C and commercial Pt/C were calculated to be 45.97 m^2/g and 43.85 m^2/g, respectively. From the result, it can be concluded that the Pt on the SiO_2 surface was catalytically active.

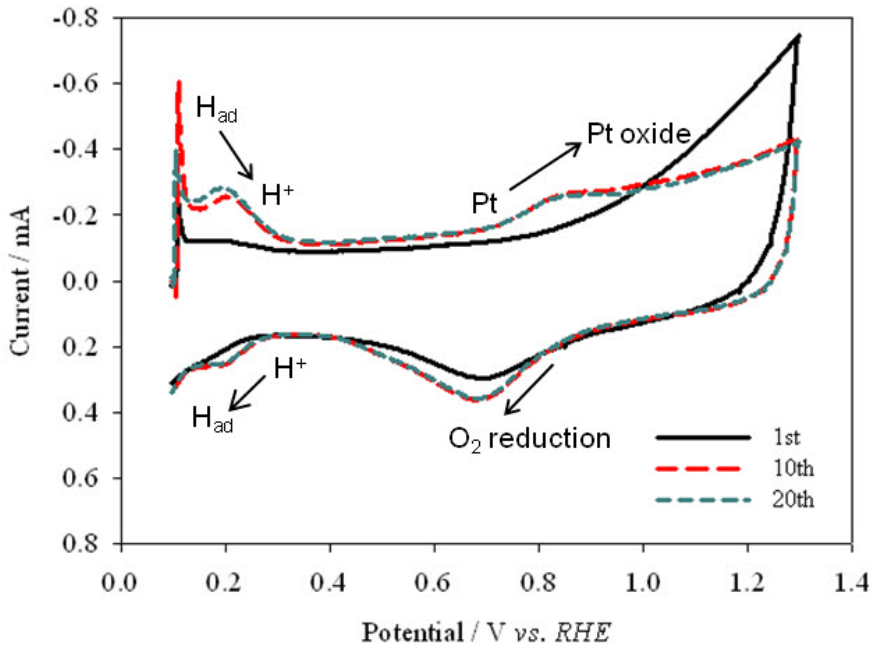

Fig. 5-4. CV result of Pt-SiO_2/C composite catalyst in 0.05 M H_2SO_4; sweep rate 100 mV/s at 293 K.

5-4. Single-Cell Experiment with Various Relative Humidity

Based on the experimental condition summarized in Table 5-1, the single-cell experiment for MEA-PSC and MEA-PC was conducted. The relative humidity was defined as a ratio of partial water vapor pressure to the total vapor pressure at given temperature. Since, water was the only liquid phase contributing the total vapor pressure for this case, the saturated vapor pressure of water at certain temperature represented the total vapor pressure. The saturated vapor pressure of water can be determined by Antoine Equation (Eq. 5-A). Therefore, we decided to equate the relative humidity, $\emptyset$ as a ratio of the saturated vapor pressure of water at temperature T_1 to the one at T_2 (Eq. 5-B), which meant the relative humidity was subjected to be altered by only controlling the humidifier temperature. For example, when the single-cell operated at 70^{o}C and the humidifier temperature was 70^{o}C, the system had a relative humidity of 100% because the saturated vapor pressure of water ($P_{H_2O,sat}$) was as high as the total vapor pressure that the system could have. The calculated relative humidity for the experimental condition was summarized in Table 5-2.

(Eq. 5-A) $log_{10}P_{H_2O,sat} = A - \frac{B}{T+C}$ where, A = 8.10765

B = 1750.286

C = 235

T = temperature, ^{o}C

(Eq. 5-B) $\emptyset = \frac{P_{H_2O,sat}\,(T1)}{P_{H_2O,sat}\,(T2)}$ where, T_1 = humidifier temperature

T_2 = cell temperature

The cell performances of MEA-PSC and MEA-PC were represented by the polarization curves and the power density curves (Fig. 5-5). The OCV, maximum power density and the power density at 0.6 V (0.6 V-power density) of MEA-PSC and MEA-PC were summarized with various RH in Table 5-3. It was observed that the performance of MEA-PC sharply decreased as RH changed from 100% to 39% (Fig. 5-5(a)). When the RH decreased to 39%, each parameter became 0.911 V and 0.183 W/cm^2. This corresponds to 30.9% of the initial performance with respect to 0.6 V-power density (0.591 W/cm^2). Unlike MEA-PC, the performance of MEA-PSC was slightly retarded as RH decreased (Fig. 5-5(b)). When RH was 39%, the cell could maintain 87.1% of initial 0.6 V-power density (from 0.263 to 0.229 W/cm^2). The rate of decrease in the performance of each MEA became larger as RH decreased down to 31%. Under RH of 31%, MEA-PC showed only 26.6% of initial 0.6 V-power density. On the other hand, it was not until RH became 31% that the performance of MEA-PCS started decreasing with a notable amount, however, still maintaining 60.8% of initial 0.6 V-power density. More surprisingly, the performance of MEA-PSC exceeded that of MEA-PC from RH of somewhere between 80% and 50%. The degraded cell performance of both MEAs according to reduced humidity was mainly caused by dehydration, which took place in anode. The dehydration of anode triggered decrease in proton conductivity; thus, the performance declined. Even if MEA-PSC lost around 40% of

its initial performance at RH of 31%, it was apparent that the MEA fabricated with Pt-SiO_2 showed better result under low-humidity condition. This will facilitate the operation of single or stacked fuel cell with less energy consumption, because the need for raising the humidifier temperature will be eliminated. The reason for the sustainable performance of MEA-PSC under low humidification was that SiO_2 in the catalyst layer impeded the dehydration of anode. The dehydration in anode is mainly caused by the movement of water from anode to cathode due to electro-osmosis. Because of hydrophilic characteristics of SiO_2 nanoparticle, the water supplied with even less-humidified reactant gas was captured by SiO_2. This helped the MEA in maintaining hydration level and keeping adequate proton conductivity even if the fuels were less humidified. The hydrophilicity of Pt-SiO_2 and Pt-SiO_2/C was confirmed by contact angle measurement (Fig. 5-6). The catalyst layer of Pt/C on glass carbon electrode had a contact angle of 129.6° (± 0.7°), while Pt-SiO_2/C had 114.4° (± 1.4°). Therefore, it can be concluded that the catalyst layer became hydrophilic and susceptible to absorb more water molecules as SiO_2 was involved.

Table 5-1. The Operating Condition for Single-Cell Experiment of MEAs

Operating Parameter	Conditions
Feed rate	(Anode) 100 ccm H_2 (Cathod) 200 ccm O_2
Humidifier temperature (cathode, °C)	70
Humidifier temperature (anode, °C)	70, 65, 55, 50, 45
Line temperature	5°C above humidifier temperature for each case
Cell temperature (°C)	70

Table 5-2. The Relative Humidity Calculation from the Saturated Vapor Pressure of Water at Given Temperature

T_1 / °C	$P_{H_2O,sat}$ (T_1) / mmHg	$P_{H_2O,sat}$ (70°C) / mmHg	∅ / %
70	233.8	233.8	100
65	187.6		80
55	118.1		50
50	92.53		39
45	71.88		31

Table 5-3. Cell Performance of MEA-PC and MEA-PSC for Various RHs

	MEA-PSC (Anode: Pt-SiO_2/C)			MEA-PC (Anode: Pt/C)		
RH / %	OCV	W_{max}[a]	$W_{0.6\ V}$[b]	OCV	W_{max}	$W_{0.6\ V}$
100	0.830	0.377	0.263	0.927	0.719	0.591
80	0.906	0.381	0.271	0.924	0.629	0.460
50	0.891	0.393	0.289	0.912	0.408	0.231
39	0.883	0.352	0.229	0.911	0.334	0.183
31	0.849	0.330	0.160	0.897	0.271	0.157

[a]W_{max}: maximum power density ($W \cdot cm^{-2}$)

[b]$W_{0.6\ V}$: power density when the voltage was 0.6 V ($W \cdot cm^{-2}$)

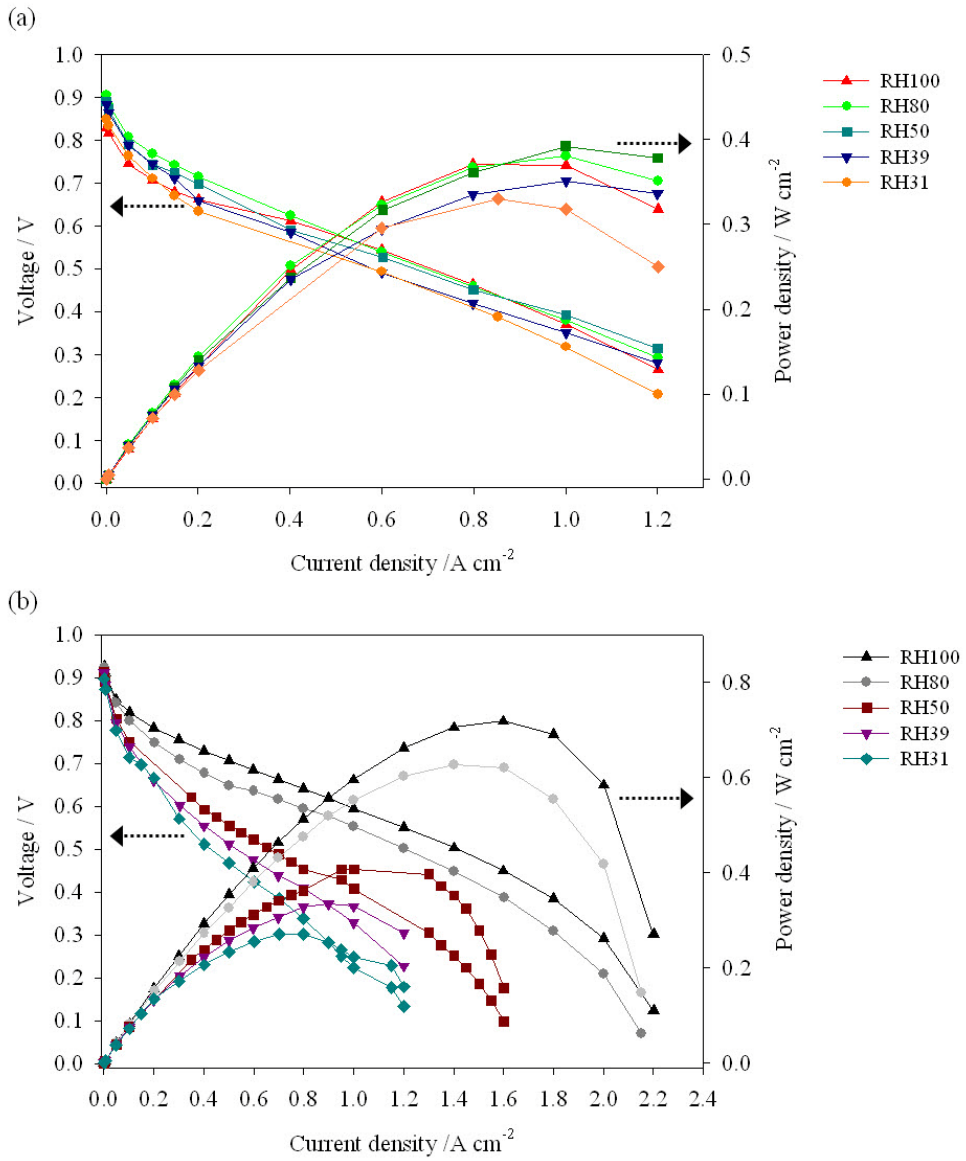

Fig. 5-5. Single-cell performance of (a) MEA-PSC and (b) MEA-PC: (▲) RH100, T_{humid} = 70 °C; (●) RH80, T_{humid} = 65 °C; (■) RH50, T_{humid} = 55 °C; (▼) RH39, T_{humid} = 50 °C; (◆) RH31, T_{humid} = 45 °C, T_{cell} = 70 °C for all data.

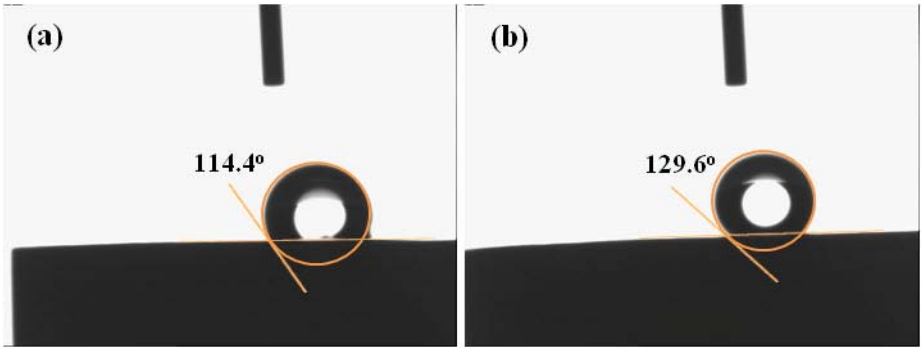

Fig. 5-6. Contact angle measurement of a droplet on the surface of (a) Pt-SiO_2/C and (b) Pt/C.

CHAPTER VI

Conclusions

The Pt_{shell}-Pd_{core}/C electro-catalyst for ORR was synthesized with a consecutive procedure; electroless deposition and galvanic displacement reaction. Cu ELD was applied to form Cu ad-layer on carbon-supported Pd catalyst, which was followed by displacement of Cu by Pt. Pt/Pd with shell/core structure was achieved through this method. The spectroscopic methods, such as XRD and XPS were used to characterize as-prepared Pt_{shell}-Pd_{core}/C catalyst during, and after the preparation. The feasibility of Cu ELD on Pd, the successful removal of Cu, and the deposition of Pt on Pd were assured by the characterization. ICP mass analysis showed that the catalyst contained 7% and 15% of Pt and Pd in atomic weight, respectively. The core-shell structure was confirmed by the intense analysis with HR-TEM and STEM-HAADF, equipped with EDS. The elemental mapping of Pt and Pd precisely visualized the core-shell configuration. The average particle size of Pt_{shell}-Pd_{core} was 3.8 nm ($\pm$0.8 nm) with quite narrow size distribution, and was highly dispersed on the carbon support. The RDE technique and the Tafel analysis in the mixed kinetic-diffusion control region, revealed that the first electron exchange reaction was the rate-determining step for ORR on both Pt_{shell}-Pd_{core}/C and Pt/C. The kinetic current was higher in Pt_{shell}-Pd_{core}/C than Pt/C, which meant the electron transfer was more facile on Pt_{shell}-Pd_{core}/C than on Pt/C. The increased kinetic current was ascribed to the superior kinetics of Pt-O hydrogenation, which was resulted from the up-shift of ε_d in Pt_{shell}-Pd_{core}/C. The calculation of

electron density of Pt in Pt_{shell}-Pd_{core}/C and XPS core-level binding energy shift, showed that Pt_{shell}-Pd_{core}/C had a high-lying ε_d by 0.27 eV, compared to Pt/C. Upon this state, the surface Pt bound OH less strongly, and thus OH could be readily desorbed. Pt_{shell}-Pd_{core}/C exhibited higher mass-specific activity Pt/C by a factor of 5, in terms of Pt mass. In conclusion, the Pt_{shell}-Pd_{core}/C electro-catalyst, prepared by the ELD of Cu and the successive displacement by Pt, was kinetically superior for ORR to the conventional Pt/C due to faster kinetics in the hydrogenation of oxygen-containing species. The method helped the synthesis of highly dispersed Pt-based electro-catalyst with small Pt content.

The electro-oxidation of MeOH was attempted by using as-prepared Pt_{shell}-Pd_{core}/C catalyst at room temperature. The electro-oxidation of MeOH on Pt_{shell}-Pd_{core}/C and Pt/C showed different behavior according to the reaction potential. The pseudo-Arrhenius plots for the current densities of the MOR on Pt_{shell}-Pd_{core}/C and Pt/C revealed almost linear correlation between log j and 1/T at all potentials, indicating that reactions on both catalysts were governed by same mechanism. The apparent activation energy (E_{app}) was calculated from the slope of these plots. In E = 0.56 V ~ 0.62 V, the E_a was approximately 62.97 kJ/mol on Pt_{shell}-Pd_{core}/C and 45.00 kJ/mol on Pt/C. Therefore, Pt_{shell}-Pd_{core}/C was less active in dissociating MeOH than Pt/C. At more positive potential region, (0.72 V ~ 0.78 V) where the water splitting and the combination reaction were dominant, E_{app} was reduced on Pt_{shell}-Pd_{core}/C (45.46 kJ/mol for Pt_{shell}-Pd_{core}/C and 48.61 kJ/mol for Pt/C). The decrease in E_{app} in this region indicated that the kinetic of the formation of OH_{ad} and the combination reaction were improved by Pt_{shell}-Pd_{core}/C. The

enhancement of MOR on Pt_{shell}-Pd_{core}/C was emphasized at potential over 0.7 V, because the RDS in MOR was not the adsorption of MeOH, but rather the electro-oxidation of adsorbed species. In summary, the enhanced stability of Pt_{shell}-Pd_{core}/C was critically influenced by the improved kinetics of OH_{ad} formation and the subsequent oxidation of CO_{ad} by OH_{ad} through the combination reaction. The electrochemical oxidation of adsorbed CO on Pt_{shell}-Pd_{core}/C and Pt/C was performed by CO_{ad}-stripping experiment. On-set potential for CO_{ad} desorption on Pt_{shell}-Pd_{core}/C was more negative than on Pt/C by 45 mV. The result indicated that OH_{ad} was more readily formed on Pt_{shell}-Pd_{core}/C surface than on Pt/C. High oxidation current observed in Pt/C meant commercial Pt was more susceptible to adsorption of CO, leading to CO_{ad}-poisoning and early deactivation compared to Pt_{shell}-Pd_{core}/C.

Pt-deposited SiO_2/C composite was synthesized via ultrasound irradiation method. By water sonolysis and subsequent radical formation (cavitation effect), Pt ions were reduced. TEM with EDS analysis showed that Pt was uniformly deposited on the surface of SiO_2. The electrochemical analysis confirmed the catalytic activity of such composite. The MEA was fabricated with the composite and tested with various relative humidity. The cell performances of MEA-PSC and MEA-PC were represented by the polarization curves and the power density curves. It was observed that the performance of MEA-PC sharply decreased as RH changed from 100% to 39%, showing 0.183 W/cm^2 of 0.6 V- power density. This corresponds to 30.9% of the initial performance with respect to 0.6 V-power density (0.591 W/cm^2). Unlike MEA-PC, the performance of MEA-PSC was slightly retarded as RH decreased. When RH was 39%, the

cell could maintain 87.1% of initial 0.6 V-power density. The degraded cell performance of both MEAs according to the reduced humidity was mainly caused by dehydration, which took place in the anode. It was apparent that the MEA fabricated with Pt-SiO_2 had an ability to maintain its performance even under low-humidity condition. The sustainable performance of MEA-PSC under low humidification was attributed to the hydrophilic SiO_2 in the catalyst layer, which impeded the dehydration of anode. The ultrasound irradiation enabled the direct deposition of highly disperse Pt nanoparticle on the SiO_2 without any kind of surface modification, and was thus beneficial in producing the materials in fuel cell catalysis.

CHAPTER VII

Future Work

■ Single-Cell Performance of Pt_{shell}-Pd_{core}/C Eelctro-Catalyst

In this study, the enhanced kinetic of ORR was not realized in single-cell experiment, which was the most disappointing outcome. One of the reasons of the discrepancy could be the effect from anodic reaction. In half-cell reaction, ORR proceeds in anodic reaction-free environment. Therefore, the kinetics of ORR could be investigated without any interference from anodic reaction. Unlike in half-cell reaction, the HOR occurs in single-cell configuration. HOR possesses activation over-potential as well, even if it is relatively small compared to that of ORR. It seemed that the HOR in the anodic side was not precisely controlled even though it was prepared the same manufacturing method for both MEA-Pt/C and MEA-Pt_{shell}-Pd_{core}/C. The second reason was the difference in the electrode structure. In half-cell reaction the surface of working electrode was smooth. For this reason the geometric area of the electrode was assumed to be equal to the active surface area. In other words, the geometric area of electrode surface in half-cell was confined. However, the electrode surface in single-cell was underestimated due to porous surface of gas diffusion layer. If the un-counted surface area had been considered, the overall performance of single-cell would have decreased. In conclusion, more precise and controlled preparation of

MEA is required in further study, to realize the enhanced catalytic activity of Pt_{shell}-Pd_{core}/C in single-cell experiment, as it was seen in half-cell experiment.

References

1. W. Vielstich, H.A. Gasteiger and A. Lamm, ‘Handbook of Fuel Cells – Fundamentals, Technology and Applications, vol.3: Fuel Cell Technology and Applications’, John Wiley & Sons, Ltd. West Sussex, England (2003).
2. K.V. Kordesch and G.R. Simader, “Environmental Impact of Fuel Cell Technology”, Chemical Reviews 95(1) (1995) 191.
3. L. Carrette, K.A. Friedrich, and U. Stimming, “Fuel Cells: Principles, Types, Fuels, and Applications”, ChemPhysChem 1, (2000) 162.
4. R.P. O’hayer, S-W. Cha, W. Colella and F.B. Prinz, ‘Fuel Cell Fundamentals’, John Wiley & Sons, Ltd. New York, NY, USA (2006).
5. LabMouse Reactions, Fuels (Energy Diagrams) (2008); **http://www.succeedingwithscience.com/labmouse/reactions/4704.php**
6. A Basic Overview of Fuel Cell Technology, Smithsonian Institution (2008); **http://americanhistory.si.edu/fuelcells/basics.htm**
7. K. Hayashi, M. Yokoo, Y. Yoshida and H. Arai, ‘Solid Oxide Fuel Cell Stack with High Electrical Efficiency’, Special Feature: NTT group R&D for reducing environmental load, NTT Technical Review, vol.7(10) (2009).
8. Y. Wang, K.S. Chen, J. Mishler, S.C. Cho, and X.C. Adroher, “A Review of Polymer Electrolyte Membrane Fuel Cells: Technology, Applications, and Need on Fundamental Research”, Applied Energy 88 (2011) 981.
9. J. Larminie and A. Dicks, ‘Fuel Cell System Explained’, John Wiley & Sons, Ltd. West Sussex, England (2000).
10. Green Econometrics, ‘Hydrogen Fuel Cells – energy conversion and storage’, Feb (2008).
11. T.R. Ralph, “Principles of Fuel Cells”, Platinum Metals Rev. 50(4) (2006) 200.
12. V. Mehta and J.S. Cooper, “Review and Analysis of PEM Fuel Cell Design and Manufacturing”, Journal of Power Sources 114 (2003) 32.
13. S. Litster and G.McLean, “PEM Fuel Cell Electrodes”. Journal of Power Sources 130 (2004) 61.
14. Fuel Cell 2000; **http://www.fuelcells.org/wp-content/uploads/2012/02/how-a-fuel-cell-**

works.jpg

15. K. Kinoshita, ‘Electrochemical Oxygen Technology’, John Wiley & Sons, Inc. New York, NY (1992).
16. A.J. Appleby, “Electrocatalysis of Aqueous Dioxygen Reduction”, Journal of Electroanalytical Chemistry 357(1-2) (1993) 117.
17. R.R. Adzic, “Recent Advanc es in the Kinetics of Oxygen Reduction”, Technical Report, Brookhaven National Lab, Upton, NY (1996).
18. D.R. Lide, ‘CRC Handbook of Chemistry and Physics’, CRC press, Inc. Boca Raton, MA (2000).
19. C. Berger, ‘Handbook of Fuel Cell Technology’, Prentice-Hall, Englewood Cliffs, NJ (1968).
20. A. Damjanovic, V. Brusic and J.O’M. Bockris, “Electrode Kinetics of Oxygen Reduction on Oxide-free Platinum Electrodes”, Electrochimica Acta 12(6) (1967) 615.
21. V.R. Stamenkovic, B.S. Mun, M. Arenz, K.J.J. Mayrhofer, C.A. Lucas, G. Wang, P.N. Ross and N.M. Markovic, “Trends in Electrocatalysis on Extended and Nanoscale Pt-bimetallic Alloy Surfaces”, Nature Materials 6 (2007) 241.
22. J.A. Rodriguez and D.W. Goodman, “The Nature of the Metal-Metal Bond in Bimetallic Surfaces”, Science 257 (1992) 897.
23. J.A. Rodriguez, R.A. Campbell, and D.W. Goodman, “Electronic Interactions in Bimetallic Systems: Core-Level Binding Energy Shifts”, Journal of Vacuum Science and Technology A 9(3) (1991) 1698.
24. J.A. Rodriguez, C.M. Truong, and, and D.W. Goodman, “Infrared Vibrational Studies of CO adsorption on Cu/Pt(111) and CuPt(111) Surfaces”, Journal of Chemical Physics 96(10) (1992) 7814.
25. J.A. Rodriguez, R.A. Campbell, and D.W. Goodman, “Electronic Interactions in Bimetallic Systems: An X-ray Photoelectron Spectroscopic Study”, Journal Physical Chemistry 94 (1990) 6936.
26. K-S. Lee, Y-H. Cho, T-Y. Jeon, S.J. Yoo, H-Y. Park, J.H. Jang, and Y-E. Sung, “Surface Structures and Electrochemical Activities of PtRu Overlayers on Ir Nanoparticles”, ACS Catalysis 2 (2012) 739.
27. L. Vitos, A.V. Ruban, H.L. Skriver, and J. Kollar, “The Surface Energy of Metals”, Surface

Science 411 (1998) 186.

28. K.J.J. Mayrhofer, V. Juhart, K. Hartl, M. Hanzlik, and M. Arenz, “Adsorbate-Induced Surface Segregation for Core-Shell Nanocatalysts”, Angewandte Chemie International Edition 48 (2009) 3529.
29. Y.G. Ma and P.B. Balbuena, “Pt Surface Segregation in Bimetallic Pt_3M Alloys: A Density Functional Theory Study”, Surface Science 602 (2008) 107.
30. G.E. Ramirez-Caballero and P.B. Balbuena, “Surface Segregation of Core Atoms in Core-Shell Structure”, Chemical Physics Letters 456 (2008) 64.
31. E. Christoffersen, P. Stolze, and J.K. Norskov, “Monte Carlo Simulations of Adsorption-Induced Segregation”, Surface Science 505 (2002) 200.
32. A. Christensen, A. Ruban, P. Stoltze, K.W. Jacobsen, H.L. Skriver, J.K. Norskov, and F. Besenbacher, “Phase Diagrams for Surface Alloys”, Physical Review B 56 (1997) 5822.
33. M. Schmid, W. Hofer, P. Varga, P. Stoltze, K.W. Jacobsen, and J.K. Norskov, “Surface Stress, Surface Elasticity, and the Size Effect in Surface Segregation”, Physical Review B 51 (1995) 10937.
34. A. Ruban, H.L. Skriver, and J.K. Norskov, “Surface Segregation Energies in Transition-Metal Alloys”, Physical Review B 59 (1999) 15990.
35. G. Wang, M.A. Van Hove, P.N. Ross, and M.I. Baskes, “Monte Carlo Simulations of Segregation in Pt-Re Catalyst Nanoparticles Journal of Chemical Physics 121 (2004) 5410.
36. G. Wang, M.A. Van Hove, P.N. Ross, and M.I. Baskes, “Monte Carlo Simulations of Segregation in Pt-Ni Catalyst Nanoparticles”, Journal of Chemical Physics 122 (2005) 24706.
37. V.R. Stamenkovic, T.J. Schmidt, P.N. Ross, and N.M. Markovic, “Surface Segregation Effects in Electrocatalysis: Kinetics of Oxygen Reduction Reaction on Polycrystalline Pt3Ni Alloy Surfaces”, Journal of Electroanalytical Chemistry 554-555 (2003) 191.
38. V.R. Stamekovic, T.J. Schmidt, P.N. Ross, and N.M Markovic, “Surface Composition Effects in Electrocatalysis: Kinetics of Oxygen Reduction on Well-Defined Pt_3Ni and Pt_3Co Alloy Surfaces”, Journal of Physical Chemistry B 106 (2002) 11970.
39. V.R Stamenkovic, B.S. Mun, K.J.J. Mayrhofer, P.N. Ross, and N.M. Markovic, “Effect of Surface Composition on Electronic Structure, Stability, and Eletctrocatalytic Properties of Pt-Transition Metal Alloys: Pt-Skin versus Pt-Skeleton Surfaces”, Journal of American

Chemical Society 128 (2006) 8813.

40. S. Koh, J. Leisch, M.F. Toney, and P. Strasser, “Structure-Acitivty-Stability Relationship of Pt-Co Alloy Electrocatlaysts in Gas-Diffusion Electrode Layers”, Journal of Physical Chemistry C 111 (2007) 3744.
41. H.A. Gasteiger, S.S. Kocha, B. Sompalli, and F.T. Wagner, “Activity Benchmark and Requirements for Pt, Pt-Alloy, and non-Pt Oxygen Reduction Catalysts for PEMFCs”, Applied Catalysis B: Environmental 56 (2005) 9.
42. R. Srivastava, P. Mani, N. Hahn, and P. Strasser, “Efficient Oxygen Reduction Fuel Cell Electrocatalysis on Voltammetrically Dealloyed Pt-Cu-Co Nanoparticles”, Angewandte Chemie International Edition 46 (2007) 8988.
43. S. Chen, P.J. Ferreira, W.C. Sheng, N. Yabuuchi, L.F. Allard, and Y. Shao-Horn, “Enhanced Activity for Oxygen Reduction Reaction on “Pt3Co” Nanoparticles: Direct Evidence of Percolated and Sandwich-Segregation Structure”, Journal of American Chemical Society 130 (2008) 13818.
44. J. Zhang, Y. Mo, M.B. Vukmirovic, R. Klie, K. Sasaki, and R.R. Adzic, “Platinum Monolayer Electrocatalysts for O_2 Reduction: Pt Monolayer on Pd(111) and on Carbon-Supported Pd Nanoparticles”, Journal of Physical Chemistry B 108 (2004) 10955.
45. K. Sasaki, Y. Mo, J.X. Wang, M. Balasubramanian, F. Uribe, J. McBreen, and R.R. Adzic, “Pt submonolayers on Metal Nanoparticles-Novel Electrocatalysts for H_2 Oxidation and O_2 Reduction”, Eelctrochimica Acta 48 (2003) 3841.
46. J. Zhang, M.B. Vukmirovic, Y. Xu, M. Mavrikakis, and R.R. Adzic, “Controlling the Catalytic Activity of Platinum-Monolayer Electrocatalysts for Oxygen Reduction with Different Substrates”, Angewandte Chemie Internation Edition 44 (2005) 2132.
47. J. Zhang, F.H.B. Lima, M.H. Shao, K. Sasaki, J.X. Wang, J. Hanson, and R.R. Adzic, “Platinum Monolayer on Nonnoble Metal-Noble Metal Core-Shell Nanoparticle Electrocatalysts for O_2 Reduction”, Journal of Physical Chemistry B 109 (2005) 22701.
48. M.H. Shao, K. Sasaki, N.S. Marinkovic, L. Zhang, and R.R. Adzic, “Synthesis and Characterization of Platinum Monolayer Oxygen-Reduction Electrocatalysts with Co-Pd Core-Shell Nanoparticle Supports”, Electrochemical Communications 9 (2007) 2848.
49. M.B. Vukmirovic, J. Zhang, K. Sasaki, A.U. Nilekar, F. Uribe, M. Mavrikakis, and R.R. Adzic, “Platinum Monolayer Electrocatalysts for Oxygen Reduction”, Electrochimica Acta

52 (2007) 2257.

50. Y. Cai, and R.R. Adzic, 'Advances in Physical Chemistry', Review Article, Hindawi Publishing Corporation (2011).
51. K. Sasaki, H. Naohara, Y.M. Choi, Y. Cai, W-F. Chen, P. Liu, and R.R. Adzic, "Highly Stable Pt Monolayer on PdAu Nanoparticle Electrocatalysts for the Oxygen Reduction Reaction", Nature Communications, in press.
52. H.I. Karan, K. Sasaki, K. Kuttiyiel, C.A. Farberow, M. Mavrikakis, and R.R. Adzic, "Catalytic Activity of Platinum Monolayer on Iridium and Rhenium Alloy Nanoparticles for the Oxygen Reduction Reaction", ACS Catalysis 2 (2012) 817.
53. K.A. Kuttiyiel, K. Sasaki, Y.M. Choi, D. Su, P. Liu, and R.R. Adzic, "Bimetallic IrNi Core Platinum Monolayer Shell Electrocatalysts for the Oxygen Reduction Reaction", Energy and Environmental Science 5 (2012) 5297.
54. S.T. Bliznakov, M.B. Vukmirovic, L. Yang, E.A. Sutter, and R.R. Adzic, "Pt Monolayer on Electrodeposited Pd Nanostructures: Advanced Cathode Catalyst for PEM Fuel Cells". Journal of Electrochemical Society 159(9) (2012) F501.
55. A. Ruban, B. Hammer, P. Stoltze, H.L. Skriver, and J.K. Norskov, "Surface Electronic Structure and Reactivity of Transition and Noble Metals", Journal of Molecular Catalysis A: Chemical 115 (1997) 421.
56. B. Hammer, J.K. Norskov, "Why Gold is the Noblest of All the Metals", Nature 376 (1995) 238.
57. B. Hammer, J.K. Norskov, "Electronic Factors Determining the Reactivity of Metal Surface", Surface Science 343 (1995) 211.
58. B. Hammer, Y. Morikawa, and J.K. Norskov, "CO Chemisorption at Metal Surfaces and Overlayers", Physical Review Letters 76(12) (1996) 2141.
59. J. Greeley, J.K. Norskov, and M. Mavrikakis, "Electronic Structure and Catalysis on Metal Surfaces", Annual Review of Physical Chemistry 53 (2002) 319.
60. J.R. Kitchin, J.K. Norskov, M.A. Barteau, and J.G. Chen, "Modification of the Surface Electronic and Chemical Properties of Pt(111) by Subsurface 3d Transition Metals", Journal of Chemical Physics 120(21) (2004) 10240.
61. B. Hammer and J.K. Norskov, "Theoretical Surface Science and Catalysis-Calculations and Concepts", Advances in Catalysis 45 (2000) 71.

62. J. Greeley and M. Mavrikakis, “Alloy Catalysts Designed from First Principles”, Nature Materials 3 (2004) 810.
63. D.G. Pettifor, “Bonding and Structure of Molecules and Solids”, Oxford University Press Inc., New York, USA (1995).
64. B.I. Lundqvist, O. Gunnarsson, H. Hjelmberg, and J.K. Norskov, “Theoretical Description of Molecule-Metal Interaction and Surface Reactions”, Surface Sciences 89 (1979) 196.
65. J. Greeley, I.E.L. Stephens, A.S. Bondarenko, T.P. Johansson, H.A. Hansen, T.F. Jaramillo, J. Rossmeisl, I. Chorkendorf, and J.K. Norskov, “Alloys of Platinum and Early Transition Metals as Oxygen Reduction Reaction Electrocatalysts”, Nature Chemistry 1 (2009) 552.
66. F.H.B. Lima, J. Zhang, M.H. Sao, K. Sasaki, M.B. Vukmirovic, E.A. Ticianelli, and R.R. Adzic, “Catalytic Activity-d-Band Center Correlation for the O_2 Reduction on Platinum in Alkaline Solutions”, Journal of Physical Chemistry C 111 (2007) 404.
67. M. Shao, P. Liu, J. Zhang, and R.R. Adzic, “Origin of Enhanced Activity in Palladium Alloy Electrocatalysts for Oxygen Reduction Reacton”, Journal of Physical Chemistry B 111(24) (2007) 6772.
68. H.C. Koo, Ph.D graduation thesis, “Study on the Initial Steps in Ag Electroless and Electrodeposition” (2008)
69. M. Paunovic, “Electrochemical Aspects of Electroless Deposition of Metals”, Plating 55 (1968) 1161.
70. P. Bindra and J. Tweedie, “Mechanisms of Electroless Metal Plating”, Journal of Electrochemical Society 130 (1983) 1112.
71. S. Yagi, ‘Potential-pH Diagrams for Oxidation-State Control or Nanoparticles Synthesized via Chemical Reduction’ from ‘Thermodynamics – Physical Chemistry of Aqueous Systems’ by Dr. J.C. Moreno, InTech (2011).
72. K.D. Beard, M.T. Schaal, J.W. Van Zee, and J.R. Monnier, “Preparation of Highly Dispersed PEM Fuel cell Catalysts using Electroless Deposition Methods”, Applied Catalysis B: Environmental 72 (2007) 262.
73. M.T. Schaal, A.C. Pickerell, C.T. Williams, and J.R. Monnier, “Characterization and Evaluation of Ag-Pt/SiO_2 Catalysts Prepared by Electroless Deposition”, Journal of Catalysis 254 (2008) 131.
74. K.D. Beard, D. Borrelli, A.M. Cramer, D.A. Blom, J.W. Van Zee, and J.R. Monnier,

"Preparation and Structural Analysis of Carbon-Supported Co Core/Pt Shell Electrocatalysts Using Electroless Deposition Methods", ACS Nano 3(9) (2009) 2841.

75. J. Rebelli, M. Detwiler, S. Ma, C.T. Williams, and J.R. Monnier, "Synthesis and Characterization of Au-Pd/SiO_2 Bimetallic Catalysts Prepared by Electroless Deposition", Journal of Catalysis 270 (2010) 224
76. M. Ohashi, K.D. Beard, S. Ma, D.A. Blom, J. St-Pierre, J.W. Van Zee, and J.R. Monnier, "Electrochemical and Structural Characterization of Carbon-Supported Pt-Pd Bimetallic Electrocatalysts Prepared by Electroless Deposition", Electrochimica Acta 55 (2010) 7376.
77. T.J. Mason, J.P. Lorimer, 'Sonochemistry: Theory, Applications and Uses of Ultrasound in Chemistry, Ellis Horwood Ltd., Chichester, UK (1988).
78. K.S. Suslick, 'Ultrasound: Its Chemical, Physical, and Biological Effects, VCH Publishers, New York, NY (1988).
79. B.G. Pollet, International Journal of Hydrogen Energy 35 (2010) 11986.
80. Y. Nagata, Y. Watananabe, S. Fujita, T. Dohmaru, and S. Taniguchi, "Formation of Colloidal Silver in Water by Ultrasonic Irradiation", Journal of the Chemical Society, Chemical Communications (1992) 1620.
81. K. Okitsu, Y. Mizukoshi, H. Bandow, Y. Maeda, T. Yamamoto, and Y. Nagata, "Formation of Noble Metal Particles by Ultrasonic Irradiation", Ultrasonics Sonochemistry 3 (1996) S249.
82. Y. Mizukoshi, R. Oshima, Y. Maeda, and Y. Nagata, "Preparation of Platinum Nanoparticles by Sonochemical Reduction of the Pt(II) ion", Langmuir 15 (1999) 2733.
83. J. Kim, J-E. Park, T. Momma, and T. Osaka, "Synthesis of Pd-Sn Nanoparticles by Ultrasonic Irradiation and Their Electrocatalytic Activity for Oxygen Reduction", Electrochimica Acta 54 (2009) 3412.
84. C.L. Bianchi, E. Gotti, L. Toscano, and V. Ragaini, "Preparation of Pd/C Catalysts via Ultrasound: A Study of the Metal Distribution", Ultrasonics Sonochemistry 4 (1997) 317.
85. D. Nagao, Y. Shimazaki, S. Saeki, Y. Kobayashi, and M. Konono, "Effect of Ultrasonic Irradiation on Carbon-Supported Pt-Ru Nanoparticles Prepared at High Metal Concentration", Colloids and Surfaces A: Physicochem. Eng. Aspects 302 (2007) 623.
86. B. Wang, "Recent Development of Non-Platinum Catalysts for Oxygen Reduction Reaction", Journal of Power Sources 152 (2005) 1.

87. H. Meng, and P.K. Shen, “Novel Pt-free Catalyst for Oxygen Electroreduction”, Electrochemical Communications 8 (2006) 588.
88. Y. Shao, J. Liu, Y. Wang, and Y. Lin, “Novel Catalyst Support Materials for PEM Fuel Cells: Current Status and Future Prospects”, Journal of Material Chemistry 19 (2009) 46.
89. S. Shanmugam, and A. Gedanken, “Synthesis and Electrochemical Oxygen Reduction of Platinum Nanoparticles Supported on Mesoporous TiO_2”, Journal of Physical Chemistry C 113 (2009) 18707.
90. B.G. Pollet, “A Novel Method for Preparing PEMFC Electrodes by the Ultrasonic and Sonoelectrochemical Techniques”, Electrochemical Communications 11 (2009) 1445.
91. Y. Huang, X. Zhou, J. Liao, C. Liu, T. Lu, and W. Xing, “Preparation of Pd/C Catalyst for Formic Acid Oxidation using a Novel Colloid Method”, Electrochemical Communications 10 (2008) 621.
92. K.G Lee, R. Wi, T.J. Park, S.H. Yoon, J. Lee, S.J. Lee, and D.H. Kim, “Synthesis and Characterization of Gold-Deposited Red, Green, and Blue Fluorescent Silica Nanoparticles for Biosensor Application”, Chemical Communications 46 (2010) 6374.
93. Wikimedia Commons; **http://commons.wikimedia.org/wiki/File:Cu-pourbaix-diagram.Svg**
94. G.E. Ramirez-Caballero, Y. Ma, R. Callejas-Tovar, and P.B. Balbuena, “Surface Segregation and Stability of Core-Shell Alloy Catalysts for Oxygen Reduction in Acid Medium”, Physical Chemistry Chemical Physics 12 (2010) 2209.
95. A. Bard, and L.R. Faulkner, ‘Electrochemical Method: Fundamentals and Application’, 2nd Ed., John Wiley & Sons, Inc. Hoboken, NJ, USA (2001).
96. J.B. Fernandas, “Electrocatalysis”; **203.199.213.48/1121/1/Electrocatalysi1.pdf**
97. J. Perez, E.R. Gonzalez, E.A. Ticianelli, “Oxygen Electrocatalysis on Thin Porous Coating Rotating Platinum Electrode”, Electrochimica Acta 44 (1998) 1329.
98. E.V. Spinace, A.O. Neto, and M. Linardi, “Electro-Oxidation of Methanol and Ethanol Using PtRu/C Electrocatalysts Prepared by Spontaneous Deposition of Platinum on Carbon-Supported Ruthenium Nanoparticles”, Journal of Power Sources 129 (2004) 121.
99. S.G. Lemos, R.T.S. Oliveira, M.C. Santos, P.A.P. Nascente, L.O.S. Bulhoes, and E.C. Pereira, “Electrocatalysis of Methanol, Ethanol and Formic Acid using a Ru/Pt Metallic Bilayer”, Journal of Power Sources 163 (2007) 695.

100. J-J. Jow, S-W. Yang, H-R. Chen, M-S. Wu, T-R. Ling, and T-Y. Wei, “Co-Electrodeposition of Pt-Ru Electrocatalysts in Electrolytes with Varying Compositions by A Double-Potential Pulse Method for the Oxidation of MeOH and CO”, International Journal of Hydrogen Energy 34 (2009) 665.
101. N. Jha, A.L.M. Reddy, M.M. Shaijumon, N. Rajalakshmi, and S. Ramaprabhu, “Pt-Ru/multi-Walled Carbon Nanotubes as Electrocatalysts for Direct Methanol Fuel Cell”, International Journal of Hydrogen Energy 33 (2008) 427.
102. D.M. Han, Z.P. Guo, R. Zeng, C.J. Kim, Y.Z. Meng, and H.K. Liu, “Multiwalled Carbon Nanotube-Supported Pt/Sn and Pt/Sn/PMo12 Electrocatalysts for Methanol Electro-Oxidation”, International Journal of Hydrogen Energy 34 (3009) 2426.
103. T. Frelink, W. Visscher, and J.A.R. Van Veen, “The Effect of Sn on Pt/C Catalysts for the Methanol Electro-Oxidation”, Electrochimica Acta 39(11/12) (1994) 1871.
104. P. Ferrin, A.U. Nilekar, J. Greeley, M. Mavrikakis, and J. Rossemeisl, “Reactivity Descriptors for Direct Methanol Fuel Cell Anode Catalysts”, Surface Science 602 (2008) 3424.
105. H. Wang, C. Xu, F. Cheng, M. Zhang, S. Wang, and S.P. Jiang, “Pd/Pt Core-Shell Nanowire Arrays as Highly Effective Electrocatalysts for Methanol Electrooxidation in Direct Methanol Fuel Cells”, Electrochemistry Communications 10 (2008) 1575.
106. F. Kadirgan, B. Beden, J.M. Leger, and C. Lamy, “Synergistic Effect in the Electrocatalytic Oxidation of Methanol on Platinum + Palladium Alloy Electrodes”, Journal of Electroanalytical Chemistry 125 (1981) 89.
107. D.F.A. Koch, D.A.J. Rand, and R. Woods, “Binary Electrocatalysts for Organic Oxidations”, Journal of Electroanalytical Chemistry 70 (1976) 73.
108. L.C. Ordonez, P. Roquero, P.J. Sebastian, and J. Ramirez, “CO Oxidation on Carbon-Supported PtMo Electrocatalysts: Effect of the Platinum Particle Size”, International Journal of Hydrogen Energy 32 (2007) 3147
109. K. Machida, M. Enyo, “In-Situ X-ray Diffraction Study of Hydrogen Entry into Pd and Pd-Au Alloy Electrodes during Atomic HCHO Oxidation”, Journal of Electrochemical Society 134(6) (1987)1472.
110. E. Christoffersen, P. Liu, A. Ruban, H.L. Skriver, and J.K. Norskov, “Anode Materials for Low-Temperature Fuel Cells: A Density Functional Theory Study”, Journal of Catalysis

199 (2001) 123.

111. O. Yepez and B.R. Scharifker, “Oxidation of CO on Hydrogen-Loaded Palladium”, Journal of Applied Electrochemistry 29 (1999) 1185.

112. G-Q. Lu, A. Crown, and A. Wieckowski, “Formic Acid Decomposition on Polycrystalline Platinum and Palladized Platinum Electrode”, Journal of Physical Chemistry B 103 (1999) 9700.

113. T. Iwasita, “Electrocatalysis of Methanol Oxidation”, Electrochimica Acta 47 (2002) 3663.

114. Y. Ishikawa, M-S. Liao, and C.R. Cabrera, “Oxidation of Methanol on Platinum, Ruthenium, and Mixed Pt-M Metals (M=Ru, Sn): A Theoretical Study”, Surface Science 463 (2000) 66.

115. S.Lj. Gojkovic, T.R. Vidakovic, and D.R. Durovic, “Kinetic Study of Methanol Oxidation on Carbon-Supported PtRu Electrocatalyst”, Electrochimica Acta 48 (2003) 3607.

116. P.A. Christensen, A. Hamnett, and G.L. Troughton, “The Role of Morphology in the Methanol Electro-Oxidation Reaction”, Journal of Electroanalytical Chemistry 362 (1993) 207.

117. G. Garcia and M.T.M. Koper, “Stripping Voltammetry for Carbon Monoxide Oxidation on Stepped Platinum Single-Crystal Electrodes in Alkaline Solution”, Physical Chemistry and Chemical Physic 10 (2008) 3802.

118. H.A. Gasteiger, N. Markovic, P.N. Ross, and E.J. Cairns, “Temperature-Dependent Methanol Electro-Oxidation on Well-Characterized Pt-Ru Alloys”, Journal of Electrochemical Society 141(7) (1994) 1795.

119. T.J. Schmidt, H.A. Gasteiger, and R.J. Behm, “Methanol Electrooxidation on a Colloidal PtRu-Alloy Fuel-Cell Catalyst”, Electrochemistry Communications 1 (1999) 1.

120. F. Kadirgan, S. Beyhan, and T. Atilan, “Preparation and Characterization of Nano-Sized Pt-Pd/C Catalysts and Comparison of Their Electro-Activity toward Methanol and Ethanol Oxidation”, International Journal of Hydrogen Energy 34 (2009) 4312.

121. S. Shanmugan, B. Viswanathan, and T.K. Varadarajan, “Preparation of Nobel Metal Supported Carbon Electrodes using Photochemically Reduced Heteropolyanions in Composite Films”, Journal of Molecular Catalysis A: Chemical 241 (2005) 52.

122. P. Katikawong, T. Ratana, and W. Veerasai, “Temperature Dependence Studies on the

Electro-oxidation of Aliphatic Alcohols with Modified Platinum Electrodes", Journal of Chemical Science 121(3) (2009) 329.

Appendix A. Major Symbols

Symbol	Meaning	Units
E	potential	V
E^0	standard potential	V
C_o^*	concentration of O in bulk	mol cm^{-3}
C_R^*	concentration of R in bulk	mol cm^{-3}
n	number of electrons involved in an electrode reaction	
R	gas constant	J mol^{-1} K^{-1}
F	Faraday constant	96485 C
j	current density	A cm^{-2}
j_o	exchange current density	A cm^{-2}
α_a	anodic transfer coefficient	
α_c	cathodic transfer coefficient	
η	over-potential	V

η_{act}	activation over-potential	V
η_{mt}	mass transfer over-potential	V
η_{ohm}	ohmic over-potential	V
T	temperature	K
i	current	A
i_k	kinetic current	A
$i_{l,c}$	limiting cathodic current	A
ω	angular frequency	s^{-1}
D	diffusion coefficient	$cm^2\ s^{-1}$
ν	kinematic viscosity	$cm^2\ s^{-1}$
$P_{H_2O,sat}$	saturated vapor pressure of water	mmHg

Appendix B. Study on Li-ion Secondary Batteries

Fading Mechanisms of Carbon-Coated Disproportionated Si/SiO_x Negative Electrode ($Si/SiO_x/C$) in Li-ion Secondary Batteries: Dynamics and Component Analysis by TEM.

This article addresses the fading mechanisms observed in carbon-coated and disproportionated $Si/SiO_x/C$ negative electrode for Li-ion secondary batteries. A combined characterization revealed that Si/SiO_x consisted of multiple nano-sized domains of amorphous Si and SiO_x, with some crystalline Si. The initial discharge capacity of $Si/SiO_x/C$ was 1380 mAh g^{-1}, however, it decreased to 578 mAh g^{-1} at the 90^{th} cycle. The electrode exhibited two different fading modes; local fading and global fading. Through intensive TEM analysis, it was concluded that both fading modes were closely related to the structural change in $Si/SiO_x/C$ during alloying/de-alloying. Local fading was induced by the contact loss between active material and conducting carbon, and the limited buffering effect of lithium silicates. Global fading was attributed to the crumbling of Si/SiO_x, which limited further alloying, leading to ever decreasing discharge capacity. Both fading modes were thoroughly investigated and monitored by qualitative and quantitative STEM-EDS analysis.

1. Introduction

Amongst known negative electrode materials in Li-ion sec-ondary batteries (LIBs), Si possesses a maximum Li^+ uptake. The theoretical mass-specific capacity of Si is 4200 mAh g^{-1} ($Li_{4.4}Si$), which is much greater than the 372 mAh g^{-1} provided by graphite negative electrode [1–3]. Furthermore, Si is inexpensive, and non-hazardous, in that a lithiated Si is safer than a lithiated graphite electrode. For those reasons, Si has been regarded as a promising negative electrode material for high capacitive Li-ion secondary batteries [4,5]. However, the practical use of Si electrode is still limited, owing to its poor cycling, which is caused by both (1) cracking/crumbling of Si, and (2) electrical loss, by a massive volume change during alloying/de-alloying [6,7]. Therefore, there have been numerous studies on minimizing crumbling, and decreasing the volume expansion of Si-based negative electrode materials: (i) structural modifications, such as decreasing the size of the Si [8–11], or synthesizing nano-structured Si electrode [12,13], (ii) potential control, to avoid formation of crystalline Li–Si alloy, (iii) use of binder, for better bonding between active material and conduct-ing carbon [8,14], (iv) use of Si oxide, which is electrochemically active in terms of Li^+ insertion/extraction, but also has less specific volume expansion than crystalline Si [15–18], (v) incorporating Si with inactive oxide materials, as a buffer to accommodate volume expansion [19,20], and/or with conducting carbon [8,21,22]. In particular, the latter two approaches were aimed at minimizing the mechanical stress derived by the extreme volume expansion of active Si, thus preventing the deterioration of the electrode. To this end, the negative electrode of SiO with

carbon in the form of composite (SiO/C) has been introduced, to improve the overall electrochemical performance of the negative electrode for LIB [23,24]. However, through charge–discharge (C–D) experiment, even the performance of the SiO/C electrode faded, to some extent, which depended on the rate of Li^+ reaction and the types of electrolyte. It was believed that the fading observed in SiO/C was closely related to the intrinsic structural property of SiO. Even though the microscopic structure of SiO was not yet completely understood, two models have been previously proposed; the random-bonding (RB) model [25], and the random-mixture (RM) model [26]. Of these, the latter one was known from the previous study to reflect the real structure of SiO. In this study, a combination of analytic techniques, which included TEM, STEM with EDS, and FE-SEM, was used to investigate the fading mechanisms of carbon-coated and disproportionated $Si/SiO_x/C$ negative electrode. By doing so, the fundamental reason for electrode fading could be determined.

2. Experimental

The $Si/SiO_x/C$ negative electrode (thickness = 27 ㎛, on Cu foil) was supplied by Samsung SDI Co. Ltd. Carbon was deposited on the surface of Si/SiO_x by chemical vapor deposition (CVD), in order to increase the conductivity of the electrode. Specifically, methane was supplied, and was thermally decomposed. In addition, polyimide binder was added into the Si/SiO_x, and its portion was 10% in mass. The $Si/SiO_x/C$ powder was pressed onto Cu foil (18

㎛ of thickness), and dried. A 2032-type coin cell was employed to conduct the electrochemical C–D experiment. Si/SiO_x/C electrode (1.1 cm in diameter) was used as a working electrode, and lithium foil (Cyprus Co.) was used as a counter and reference electrode. Polypropylene–polyethylene–polypropylene (PP–PE–PP, Celgard^{TM}) tri-copolymer was used as a separator. 1.3 M $LiPF_6$ dissolved in a co-solvent of ethylene carbonate (EC), fluoroethylene carbonate (FEC), and diethylene carbonate (DEC) (EC:FEC:DEC = 1:2:7 in vol%) was used for the electrolyte. All components were assembled in an Ar-filled glove box. The coin cells were cycled with a battery cycler (Toyo Co.), and the upper and lower cut-off potential were 1.4 V and 5 mV, respectively (vs. Li^+/Li). The cycle protocol was given as follows: 0.05C (0.15 mA) for formation, 0.1C (0.3 mA) for pre-cycling, and 0.5C (1.5 mA) for further cycling. In order to have maximum discharge capacity, a constant potential step was employed for alloying in the formation step (10h), together with further cycling (current cut-off, to 0.15 mA). For characterization of the electrode, highly advanced TEM (Technai, F20) was used. The accelerating voltage of the microscope was 200 kV, and was suited for TEM imaging (～930kx), STEM imaging (～230Mx), and nano-material analysis. The point and line resolution were 0.25 nm and 0.102 nm, respectively. The elemental analysis, such as line scanning and elemental mapping, was performed in STEM mode with EDS. All samples were fabricated by focused-ion beam (FIB), in order to have a cross-sectional image prior to TEM analysis. Additional thinning was adopted to reduce thickness of the electrode, if needed. The surface morphology, according to different cycle stages, was characterized with FE-SEM (JSM-6701F).

3. Result and Discussion

3.1. Characterization of $Si/SiO_x/C$

The SiO powder was prepared by condensing the vapor formed when pure Si and pure quartz reacted in a high vacuum and at high temperature ($Si + SiO_2 \rightarrow 2Si$). However, solid SiO was thermodynamically $u_n$stable at high temperature, therefore it disproportionated into Si and Si sub-oxides (i.e. SiO_x, such as Si_2O_3, SiO_2) right after being formed at 1000–1400 ◦C ($2SiO \rightarrow Si + SiO_2$ or SiO_x) [27–29]. Furthermore, a small portion of crystalline Si was mixed in the SiO_x, because amorphous Si was crystallized during preparation at high temperature. For the above reasons, the electrode was denoted as Si/SiO_x in this study. Since the conductivity of Si/SiO_x was relatively low, a conducting carbon layer was formed on the surface of the Si/SiO_x by means of CVD. The cross-sectional TEM image of $Si/SiO_x/C$ is given in Fig. 1(a). The thickness of carbon layer was not constant, and ranged from 86 to 135 nm. The small angle electron diffraction (SAED) pattern of bulk $S/iSiO_x/C$ electrode (inset of Fig. 1(a)) shows the multiple rings, which were assigned to crystalline SiC (JCPDS file no. 29-1129). Crystalline SiC was developed, because the crystalline Si reacted with C at high temperature. Meanwhile, the disproportionation of SiO was characterized by HR-TEM, EDS, and XRD. Through HR-TEM analysis, it was observed that the electrode consisted of multiple nano-domains, with size

ranging from 10 to 20 nm. However, the nano-domains had different contrast, indicating that they had different compositions. By EDS analysis, it was known that the lighter domain had higher Si/O, while the darker domain had a lower Si/O ratio. Based on the results, the Si/SiO_x/C contained mixed-domains of Si and SiO_x, which were derived from the disproportionation reaction of SiO. This result corresponded to what was previously observed from other research groups [27–29]. In addition, some crystalline Si was also found through HR-TEM and diffraction analysis, as expected (Fig. 1(b)). The FFT diffraction pattern of the selected region of the electrode was fitted to Si(111) (d(111) = 0.314 nm; JCPDS file no. 27-1402). If magnified further, it was observed that crystalline Si was dispersed in the SiO_x matrix as seen in Fig. 1(c) and (d). The formation of Si crystalline was due to the high temperature applied during the preparation of the electrode, as discussed previously.

3.2. Cycling Performance of Si/SiO_x/C

The electrochemical performance Si/SiO_x/C in EC:DEC-based electrolyte is shown in Fig. 2(a). The initial specific discharge capacity was approximately 1380 mAh g^{-1}. The electrode maintained its capacity until the 20^{th} cycle, still exhibiting 1362 mAh g^{-1}. The initial coulombic efficiency (ICE) was 94.7%, which reflected the considerable amount of irreversible capacity, mostly due to the charge consumption in the reduction of electrolyte, and the formation of solid electrolyte interface (SEI). Normally, the electrode tends to have relatively low coulombic

efficiency in the first cycle, since SEI is believed to be formed through the first lithiation. Then, the efficiency is improved within the following few cycles, as the electrode becomes activated. For Si/SiO_x, however, it took 10 cycles to reach 99% of coulombic efficiency. The extended cycle number for stabilized efficiency could be explained by the following two reasons: (1) the morphological change of Si/SiO_x, and (2) the continuous electrolyte decomposition. As regards a specific explanation, a crumbing of the electrode and a cracking started from the beginning of the C–D process. The surface cracking induced an enlarged surface area of the electrode, which led to facile Li^+ transport. The enhanced mass transport of Li^+ improved the kinetics of alloying/de-alloying, which ultimately drove an increase of efficiency. The surface cracking of Si/SiO_x and the increased surface roughness were monitored by FE-SEM analysis (Fig. 3). On the other hand, SEI could be continuously formed on the newly exposed surface of electrode, as a result of the cracking. This would negate the enhanced Li^+ transport effect; however, the contribution from the latter prevailed over that from the former. Consequently, by those two competing effects, we could have stable efficiency at the 10^{th} cycle. After the 10^{th} cycle, the electrochemical performance of Si/SiO_x faded in terms of both specific capacity and efficiency. The specific charge and discharge capacity started decreasing beyond the 10^{th} cycle, and the specific discharge capacity reached 578 mAh g^{-1} at the 90^{th} cycle. The efficiency, however, decreased sharply at the 29^{th} cycle, showing 98.2%, and then recovered when the cycle number exceeded the 40^{th}. This atypical phenomenon, called hump behavior, was entirely different from what had been observed in previous studies dealing with either Si, or any type of negative

electrode material. Moreover, the hump kept appearing through the repeated experiments. Normally, the efficiency tends to increase, once the electrode is activated. The hump observed here in the midst of the C–D experiment was closely related to the change in the electrode structure during alloying/de-alloying. Until the 10^{th} cycle, both Si and SiO_x maintained a close contact to con-ducting carbon, so that inserted Li^+ could fully react with Si by alloying, and could be readily withdrawn by de-alloying. However, a large volume expansion accompanied the C–D process, thus some individual Si and SiO_x started losing contact with the conducting carbon or with themselves, especially when the electrode was de-alloyed. Upon this situation, some of the inserted Li^+ could not be released during de-alloying, and thus the efficiency of $Si/SiO_x/C$ became decreased (from the 10^{th} to the 29^{th} cycle). This type of fading was considered as a local mode, since it was associated with individual active material [20]. In conclusion, the hump behavior was induced by this local fading. As already noted, the C–D result showed the overall decrease in specific discharge capacity from the 10^{th} cycle. Unlike the local fading, the reason for the overall decrease was caused rather by the entire collapse of the electrode; i.e. crumbling of Si/SiO_x, and the exfoliation of the entire electrode. This fading mode could be referred to as a global fading, which was generally observed in Li-alloy metal negative electrode material, including Sn or Si. It was noted that from the 10^{th} to the 29^{th} cycle, the coulombic efficiency decreased along with the discharge capacity. This meant that the electrode experienced both global and local fading in the cycle span. After the 29^{th} cycle, however, the electrode exhibited global fading, accompanied with consistent and relatively high coulombic

efficiency (>99%). In other words, the electrode had only a global fading mode after the 29th cycle. This could be explained by the limited alloying in the exfoliated electrode. As the electrode disconnected, Li^+ could only diffuse into electrically connected Si/SiO_x. In other words, the crumbed Si/SiO_x, which was inactive or dead, could not contribute to the discharge capacity. Furthermore, the local contact of residual active material with conducting carbon was maintained. Therefore, once Li^+ ions were intercalated into the connected Si/SiO_x, they could be easily released during de-alloying, leading to high efficiency. The local fading and global fading are described with schematic diagrams in Fig. 4. From the 10th to the 29th cycle, both fading modes took place, as seen in Fig. 4(b). After the 29th cycle, only the electrode experienced global fading, as shown in Fig. 4(c). These two fading modes were intensively studied again with qualitative analysis of TEM, in the later section. It seems that the degree of fading was closely related to the amount of stress applied to the electrode during the C–D process. In order to investigate the effect of stress on the fading, the C-rate was changed. A higher C-rate would bring more stress to the electrode, while a lower C-rate would alleviate the stress. As was expected, the electrode cycled with higher C-rate exhibited a hump at an earlier state of cycling, and it degraded much faster. On the other hand, the electrode discharged and charged with a lower C-rate did not have a hump and its discharge capacity decreased by a much lower rate (Fig. 2(b)). It could be concluded that both fading modes were affected by structural deformation that was driven by alloying/de-alloying, which is inevitable to some extent. The electrochemical result of the C–D process was reviewed with differential capacity plots

according to cycles (Fig. 5). The improved kinetics of alloying/de-alloying was once more supported by the increased specific discharge and charge capacities ($1^{st} < 2^{nd} < 5^{th} < 10^{th}$) shown in Fig. 5(a). This was evidenced by the increasing peak intensity where the alloying process started (0.25 V vs. Li/Li^+, Fig. 4(b)). In terms of polarization, it was observed that the degree of polarization from the 1^{st} to the 29^{th} cycle did not change much. On the contrary, the polarization notably changed from the 29^{th} to the 50^{th} cycle, indicating that the sys-tem possessed high internal resistance. This was caused by the exfoliation of electrode, which referred to the global fading of the electrode.

3.3. STEM Analysis with EDS Results

The cross-sectional TEM images of $Si/SiO_x/C$ according to the number of cycles are given in Fig. 6. All samples were prepared by FIB, and made thin enough by further thinning, if necessary. It was observed that the outer surface was covered by SEI, after the formation step. The thickness of SEI layer kept increasing, as the electrode experienced the C–D process (formation < pre-cycling < 10^{th} < 29^{th} < 50^{th}). The main reason for the above result was a cracking of the electrode, which resulted in continuous reduction of the electrolyte. Both local and global fading phenomena were further investigated by STEM analysis as promised (Fig. 7(a)–(f)). From the formation step (Fig. 7(b)) to the 10^{th} cycle (Fig. 7(d)), Si/SiO_x in the bulk phase and the surface area were in close contact with the conducting carbon. Even though SEI

was formed in between the bulk phase and the surface, the thickness was too small to generate high resistance. Above the 29th cycle (Fig. 7(e)), how-ever, only the outmost surface layer contained a very small amount of Si, and there was a thick SEI layer between the bulk and the surface. This Si compound looked to be electrically isolated, and could no longer reversibly take part in the alloying/de-alloying process; this was local fading. As the crumbling of Si/SiO_x proceeded, the portion of the isolated Si/SiO_x increased over cycling, and this was the major cause of the ever-decreasing specific discharge capacity of Si/SiO_x/C; this was global fading. In other words, the local and global fading started at some point after the 10th cycle, and continued thereafter, which was exactly same in the cycle performance (Fig. 2(a)). After the 50th cycle (Fig. 7(f)), only electrically-connected Si/SiO_x contributed to the overall discharge capacity, and was included in calculating efficiency; this was the global fading mode only. The local fading could be investigated from another perspective, which was the inconsistent buffering role of lithium silicate. It was already reported that when SiO powder reacted with Li^+, Li_2O or/and various types of lithium silicates, such as $Li_2Si_2O_5$, Li_2SiO_3, and Li_4SiO_4 were formed. Through ^{29}Si NMR and ^7Li NMR analysis, the kinetics of Li^+ uptake of SiO_x is known to be different from those of Si, that is, SiO_x irreversibly would become lithium silicates, prior to Si. Then, the lithium silicates would act as a buffer against volume expansion [30]. However, the sustainable buffering role of these lithium silicates could be questionable, if the electrode experienced alloying/de-alloying over time. In STEM mode, quantitative as well as qualitative analyses on the cycled Si/SiO_x/C electrode were possible by EDS. The STEM-EDS result was presented in

Table 1. By combining those complementary results, it was possible to detect the compositions of electrode, and trace them with the scanned line (the red line in the STEM image). Herein, the compositional analysis was performed by laying stress, especially on Si and O with their atomic ratio, in order to confirm the validity of the buffering effect over cycling. The obtained EDS spectra can be divided into a single spectrum for each element of interest (S, O, C, and F, P if necessary). The scanning direction started from inside to outside, i.e. from the bulk to the surface layer for all electrodes. Prior to conducting quan-titative analysis, assumptions were made: (1) the O contribution from SEI and lithium oxide could be eliminated, (2) SEI mainly consisted of carbonate-based material, (3) no O was incorporated from the atmosphere. In region I (6th pt. from bulk) of the pristine Si/SiO_x/C, the atomic ratio of O to Si (x in SiO_x) was measured to be 0.92, because of the disproportionate Si and SiO_2. At the margin of the bulk electrode, C content instantly increased, implying the existence of C coating (region II, 32^{nd} pt. from bulk). The C layer contained a small amount of Si and O, meaning that some Si/SiO_x domains were dispersed and mixed in the layer. The atomic ratio in region II was changed to 1.91, which indicated that the SiO_x domain occupied a higher portion than the Si domain. The slight increase of Si content around 300 nm was from the detector, which was negligible. After the formation step, the de-alloyed Si/SiO_x/C electrode was analyzed, as seen in Fig. 7(b). It was presumed that both the Si/SiO_x and the carbon layer would participate in the Li^+ alloying reaction. Therefore, the surface composition must have changed. In the very near side of the electrode (region III, 3^{rd} pt. from bulk), x was changed from 0.92 to 1.38. The increased atomic

percentage of O was due to the formation of O-containing species, lithium silicates. Other than lithium silicates, lithium carbonate could also be formed as the electrolyte decomposed. However, considering that the C content was very low, it was conclusive that the lithium silicate was the major reason for the increased O content. Since only a small amount of SiO_x was turned to lithium silicates in the formation step, the x value was relatively small. In region IV (13^{th} pt. from bulk), considerable amounts of C, O, F, and P were contained. This was SEI, which was newly formed as a result of reduction of electrolyte, and decomposition of Li salt. By the way, the O/C ratio was high near the bulk electrode within the SEI. It implied that lithium carbonate or alkyl carbonate was preferentially formed, prior to other organic species. In region V (29^{th} pt. from bulk), the content of Si and O abruptly increased (x = 4.25). Even if the con-tribution from lithium oxide and carbonaceous compound were eliminated by correction, O was more abundant than Si (x = 3.01). This was attributed to the lithium silicate derived from the SiO_x domain, which was initially dispersed in the carbon layer, as in region II. This phenomenon was also seen after the pre-cycling stage (Fig. 7(c)), and the 10th cycle (Fig. 7(d)). For example, the x value was 1.32 in region VI (2^{nd} pt. from bulk), while it was 4.11 in region VIII (30^{th} pt. from bulk), after correction. The tendency was continued until the 10^{th} cycle, which meant that the formation of lithium silicate was rather continuous in the $Si/SiO_x/C$ negative electrode. This was supported by the differential capacity plot in Fig. 5(b), where the peak at 0.25 V (formation of lithium silicate) appeared until the 10^{th} cycle. It was noted that lithium silicate was pushed away to the outmost surface, after it was formed. It has been reported that the distinct alloyed-Si and

lithium silicate phase were observed through TEM analysis, when SiO powder was alloyed. Furthermore, the alloyed-Si domains were segregated from the lithium silicates phase, and surrounded by them; this was buffering effect [30]. Based on the results, it was concluded that similar buffering took place during the C–D process in the $Si/SiO_x/C$, which allocated lithium silicate in the marginal area of the electrode. Even when the electrode reached the 29^{th} cycle, the tendency was still observed. The value x in region XII (3^{rd} pt. from bulk) and in region XIV (39^{th} pt. from bulk) were 1.08 and 2.59, respectively. However, it should be noted that the total atomic percentage of lithium silicate in region XIV was drastically decreased, compared with that from the corresponding position at the 10^{th} cycle (region XI, 35^{th} pt. from bulk); from 60.59 at% to 38.07 at%. This indicated that the amount of lithium silicates decreased for some reason, and could not fulfill its role as a buffer anymore. This must have led to instant volume expansion, and a considerable amount of charge should be consumed, to make additional SEI. This was the reason why such a severe capacity change was accompanied with a hump appearance at the 29^{th} cycle; this was global fading with local fading. This was more emphasized when compared with the result from the 50^{th} cycle. The x was 1.71 in region XVII (44th pt. from bulk), however, the total amount of lithium silicate increased to 85.01 at%. This indicated that a sufficient amount of lithium silicates remained at the 50^{th} cycle, so that the local structure could be maintained. Therefore, it was certain that the limited buffering effect was one of the causes of the local fading.

4. Conclusions

Carbon-coated and disproportionated $Si/SiO_x/C$ was characterized by XRD, TEM, STEM, and SEM. The electrode exhibited a structure of nano-sized amorphous Si domains that were uniformly dispersed in an amorphous SiO_x matrix. Some crystalline Si was developed, because the electrode was prepared at a high temperature condition. $Si/SiO_x/C$ exhibited a gradual increase in the total discharge capacity and coulombic efficiency before the 10^{th} cycle. This was regarded as an activation step, which was balanced by an increased kinetics of Li^+ alloying, and a subsequent formation of SEI. $Si/SiO_x/C$ started losing its performance after the 10^{th} cycle, showing different fading behaviors. Until the 29^{th} cycle, both local and global fading modes were observed. A large volume expansion, driven by the limited buffering effect of lithium silicates and the electric disconnect of Si/SiO_x with conducting carbon, caused the local fading; and a severe crumbling of Si/SiO_x generated global fading. After the 29^{th} cycle, however, only global fading appeared. In this stage, already-crumbled active material was not included in calculating coulombic efficiency. Therefore, the electrode could maintain high efficiency.

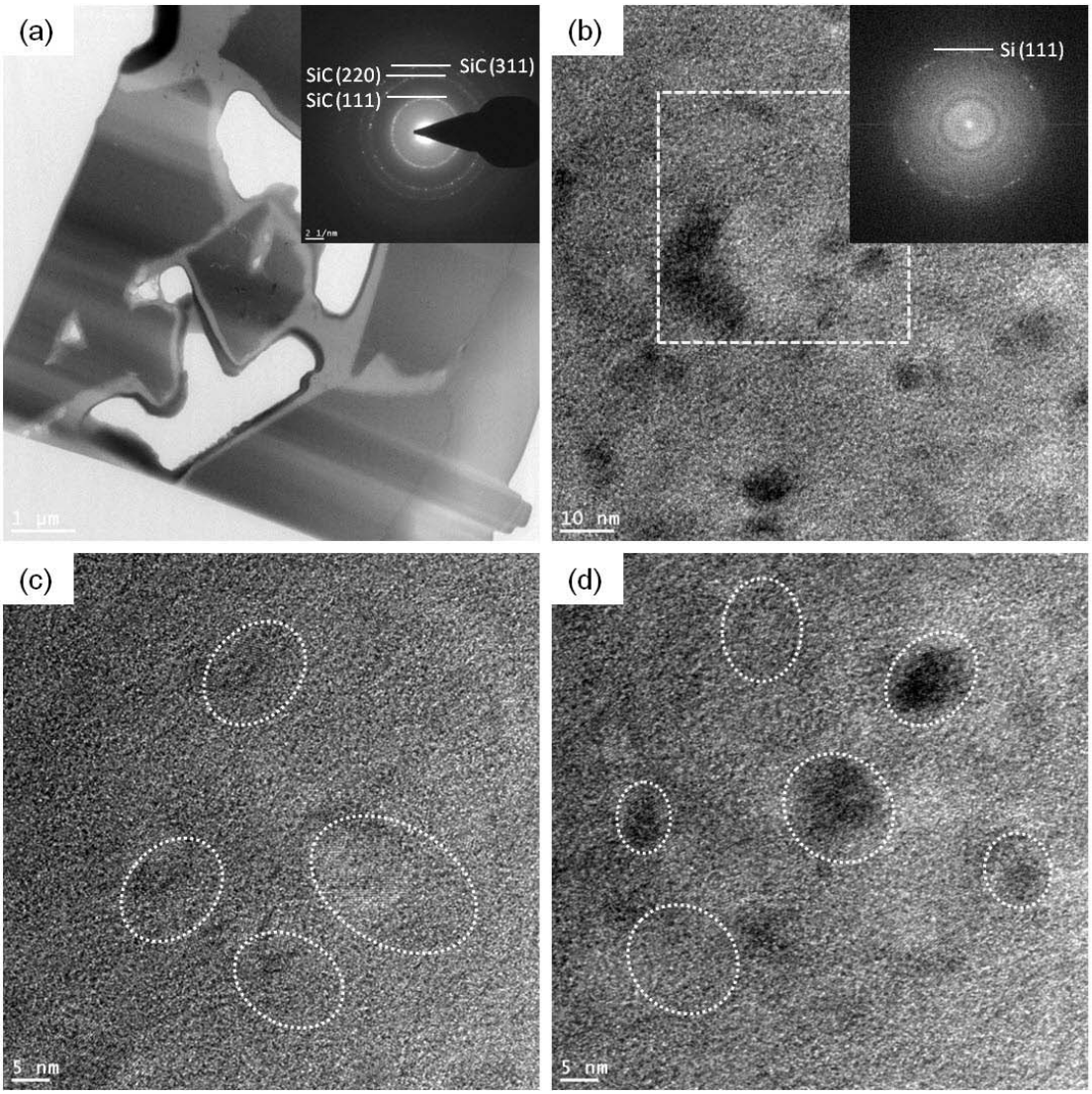

Figure 1. (a) TEM image of pristine Si/SiO_x/C with SAED pattern (inset), (b) HR-TEM of Si crystalline in SiO_x matrix with its FFT pattern (inset) and of (c-d) Si domain dispersed in SiO_x matrix.

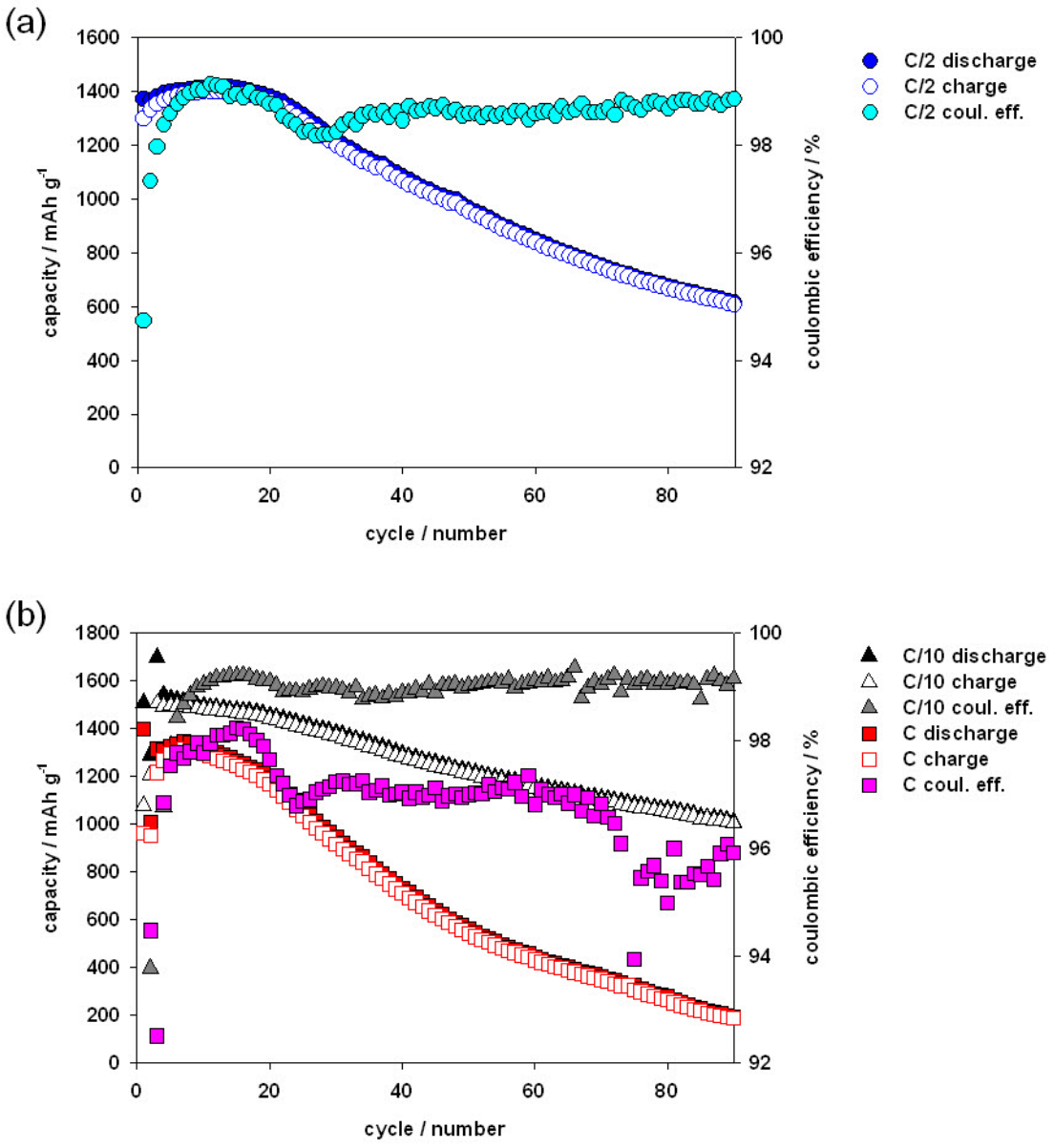

Figure 2. (a) Discharge/charge capacity of $Si/SiO_x/C$ with coulombic efficiency when alloyed/de-alloyed with C/2, and (b) C/10, and C.

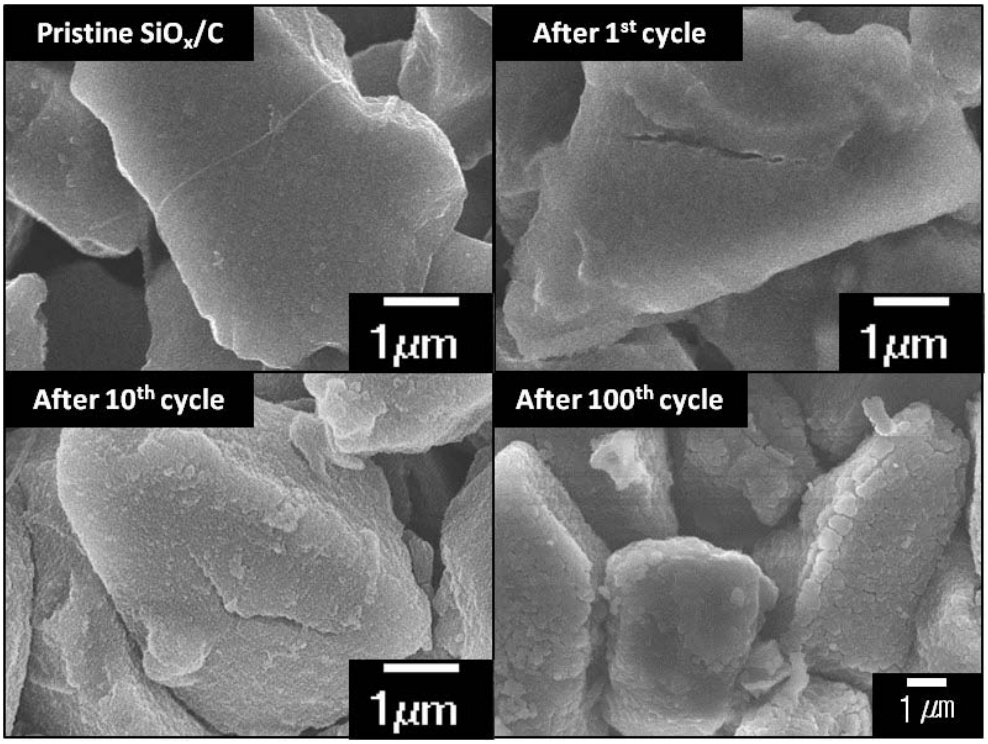

Figure 3. FE-SEM images of surface of $Si/SiO_x/C$ electrode according to cycle number (pristine, 1^{st}, 10^{th}, 100^{th}).

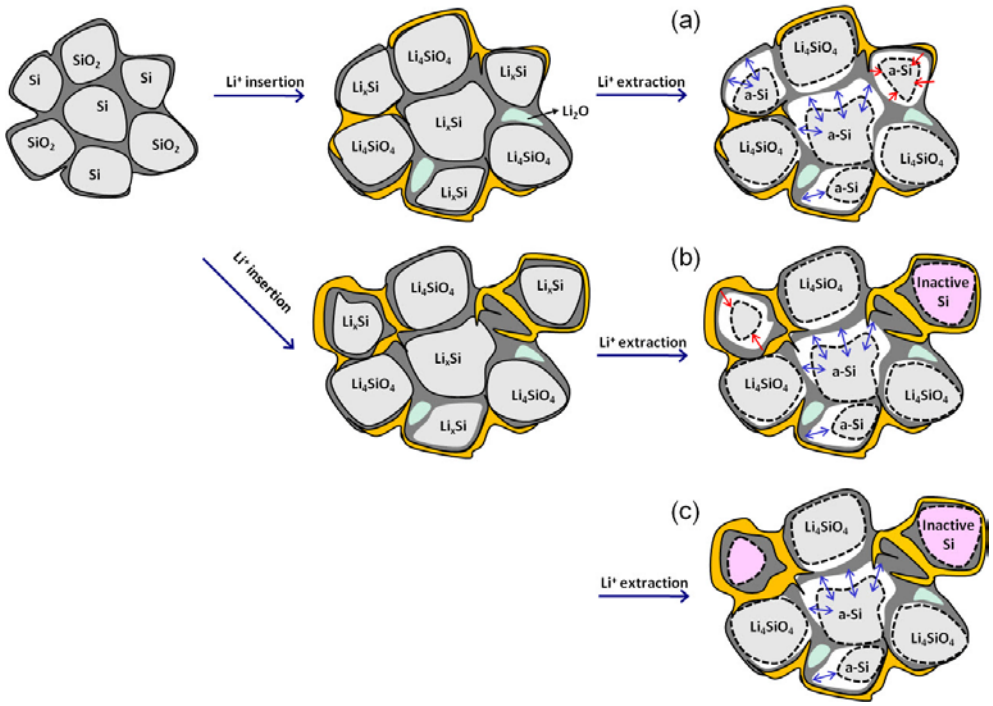

Figure 4. Description of (a) a local fading mode, (b) a global fading with local fading, and (c) global fading mode only.

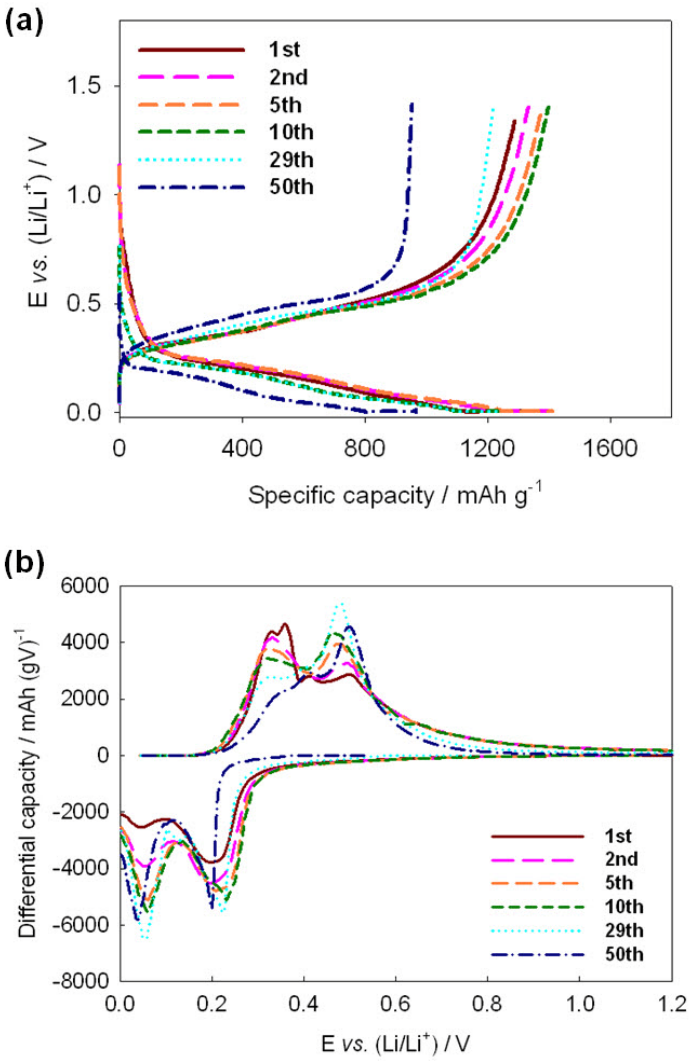

Figure 5. (a) Potential profiles and (b) differential capacity plots of $Si/SiO_x/C$ cycled from 1st to 50th.

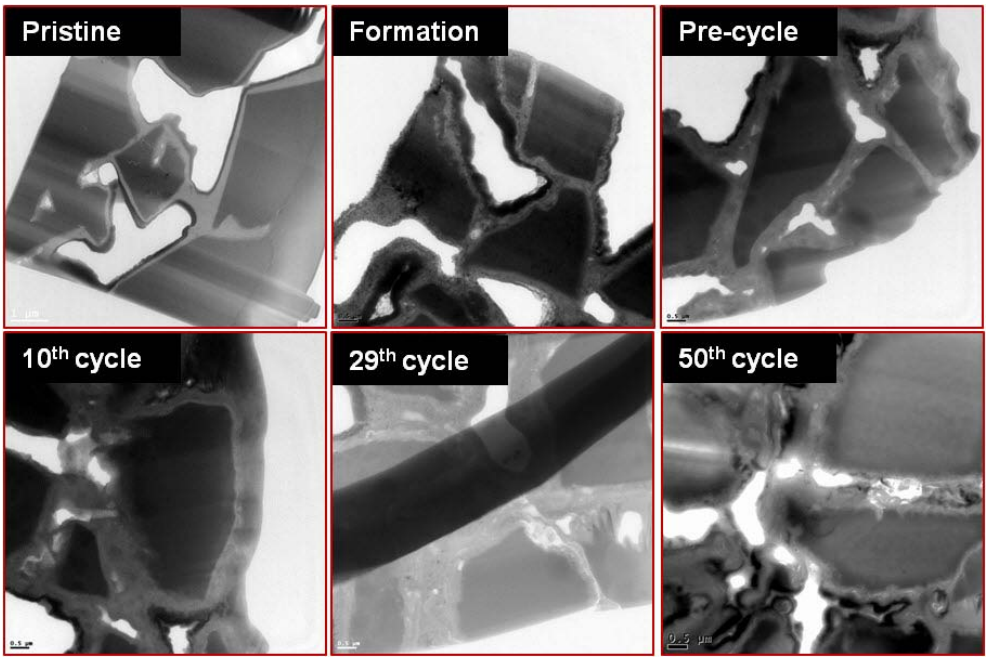

Figure 6. TEM images of $Si/SiO_x/C$ with different cycle stage (pristine, formation, pre-cycling, 10^{th}, 29^{th}, 50^{th}); all electrodes were prepared by FIB.

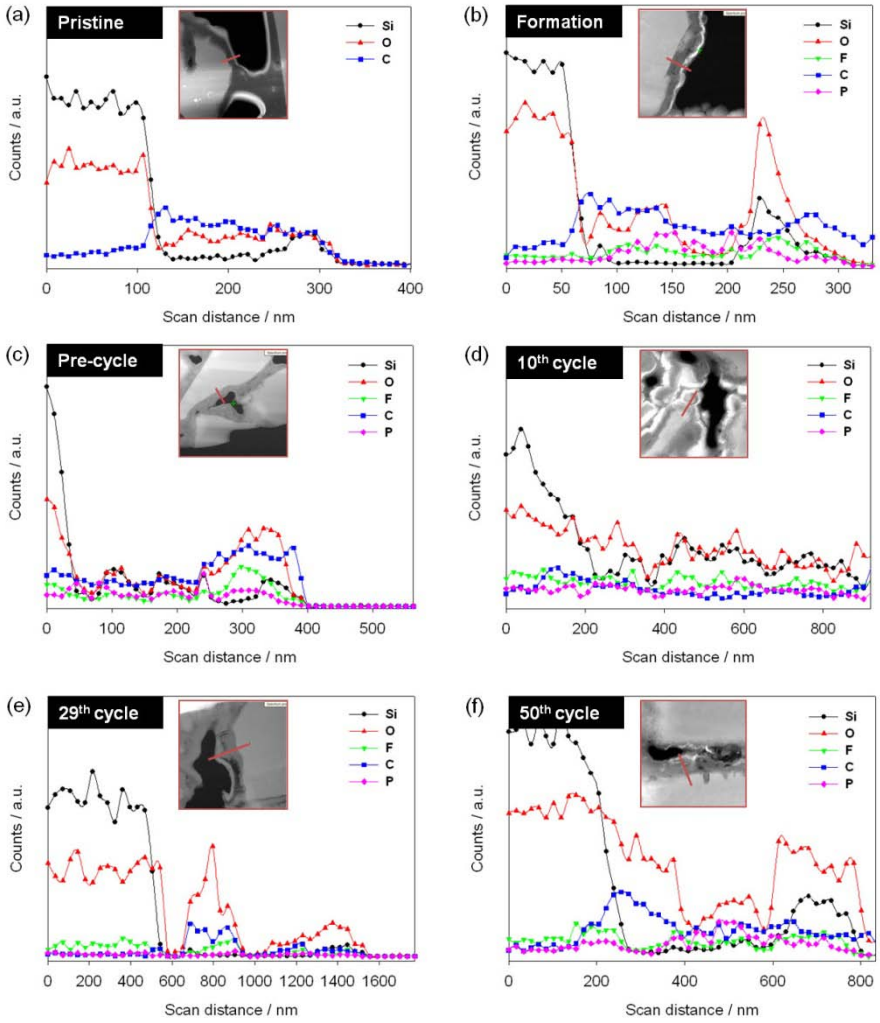

Figure 7. Qualitative and quantitative analysis of Si/SiO_x/C by STEM-EDX with image (inset); (a) pristine, (b) after formation, (c) after pre-cycling, (d) 10^{th} cycle, (e) 29^{th} cycle, and (f) 50^{th} cycle.

Table 1. Quantitative and qualitative analysis results by STEM-EDX.

	Pristine		Formation			Pre-cycling		
Element/Region	I	II	III	IV	V	VI	VII	VIII
Si (K) / at%	52.16	7.13	40.86	1.66	17.05	40.57	22.92	3.64
O (K) / at%	47.84	15.58	56.61	68.04	68.66	53.68	56.76	14.95
C (K) / at%	0.00	77.29	1.52	16.25	5.39	3.04	12.21	80.76
F (K) / at%	-	-	1.01	9.83	7.78	2.07	4.99	0.37
P (K) / at%	-	-	0.00	4.22	1.12	0.64	5.12	0.28

	10^{th} cycle			29^{th} cycle			50^{th} cycle		
Element/Region	IX	X	XI	XII	XIII	XIV	XV	XVI	XVII
Si (K) / at%	59.79	31.95	40.65	47.93	0.14	10.60	56.94	5.65	31.42
O (K) / at%	35.56	53.53	48.05	52.07	62.71	72.89	42.79	42.80	64.31
C (K) / at%	4.27	13.22	9.37	0.00	35.47	14.87	0.00	36.06	3.57
F (K) / at%	0.00	0.00	0.00	0.00	1.68	1.64	0.27	7.66	0.00
P (K) / at%	0.38	1.30	1.93	0.00	0.00	0.00	0.00	7.83	0.70

References

[1] C.J. Wen, R.A. Huggins, Journal of Solid State Chemistry 37 (1981) 271.

[2] J.O. Besenhard, J. Yang, M. Winter, Journal of Power Sources 68 (1997) 87.

[3] S. Bourderau, T. Brousse, D.M. Schleich, Journal of Power Sources 81–82 (1999) 233.

[4] J.P. Maranchi, A.F. Hepp, P.N. Kumta, Electrochemical and Solid State Letters 6 (9) (2003) A198.

[5] M. Uehara, U. Suzuki, T. Tamura, K. Sekine, T. Takamura, Journal of Power Sources 146 (2005) 441.

[6] S. Park, J.H. Ryu, S.M. Oh, Journal of the Electrochemical Society 158 (5) (2011) A498.

[7] B.A. Boukamp, G.C. Lesh, R.A. Huggins, Journal of the Electrochemical Society 128 (4) (1981) 725.

[8] H. Ma, F. Cheng, J. Chen, J. Zhao, C. Li, Z. Tao, J. Liang, Advanced Materials 19 (2007) 4067.

[9] H. Li, X. Huang, L. Chen, Z. Wu, Y. Liang, Electrochemical and Solid State Letters 2 (11) (1999) 547.

[10] N. Ding, J. Xu, Y. Yao, G. Wegner, I. Lieberwirth, C. Chen, Journal of Power Sources 192 (2009) 644.

[11] H. Kim, M. Seo, M.-H. Park, J. Cho, Angewandte Chemie International Edition 49 (2010) 2146.

[12] C.K. Chan, H. Peng, G. Liu, K. McIlwarth, X.F. Zhang, R.A. Huggins, Y. Cui, Nature Nanotechnology 3 (2008) 31.

[13] H. Kim, B. Han, J. Choo, J. Cho, Angewandte Chemie International Edition 47 (2008) 10151.

[14] D. Mazouni, B. Lestriez, L. Roue, D. Guyomard, Electrochemical and Solid State Letters 12 (11) (2009) A215.

[15] J. Yang, Y. Takeda, N. Imanishi, C. Capiglia, J.Y. Xie, O. Yamamoto, Solid State Ionics 152–153 (2002) 125.

[16] M. Miyachi, H. Yamamoto, H. Kawai, Y. Ohta, M. Shirakata, Journal of the Electrochemical Society 152 (10) (2005) A2089.

[17] M. Miyachi, H. Yamamotor, H. Kawai, Journal of the Electrochemical Society 154 (4) (2007) A376.

[18] C.-H. Doh, C.-W. Park, H.-M. Shin, D.-H. Kim, Y.-D. Chung, S.-I. Moon, B.-S. Jin, H.-S. Kim, A. Veluchamy, Journal of Power Sources 179 (2008) 367.

[19] I.-S. Kim, G.E. Blomgren, P.N. Kumta, Electrochemical and Solid State Letters 6 (8) (2003) A157.

[20] J.P. Maranchi, A.F. Hepp, A.G. Evans, N.T. Nuhfer, P.N. Kumta, Journal of the Electrochemical Society 153 (6) (2006) A1246.

[21] W.-R. Liu, J.-H. Wang, H.-C. Wu, D.-T. Shieh, M.-H. Yang, N.-L. Wu, Journal of the Electrochemical Society 152 (9) (2005) A1719.

[22] T. Zhang, L. Fu, J. Gao, L. Yang, Y. Wu, H. Wu, Pure and Applied Chemistry 78 (10) (2006) 1889.

[23] W.-R. Liu, Y.-C. Yen, H.-C. Wu, M. Winter, N.-L. Wu, Journal of Applied Electrochemistry 39 (2009) 1643.

[24] Y.-S. Hu, R. Demir-Cakan, M.-M. Titirici, J.-O. Muller, R. Schlogl, M. Antonietti, J. Maier, Angewandte Chemie International Edition 47 (2008) 1645.

[25] R.J. Temkin, Journal of Non-Crystalline Solids 17 (1975) 215.

[26] A. Hohl, T. Wieder, P.A. van Aken, T.E. Weirich, G. Denninger, M. Vidal, S. Oswald, C. Deneke, J. Mayer, H. Fuss, Journal of Non-Crystalline Solids 320 (2003) 255.

[27] J.-H. Kim, H.-J. Sohn, H. Kim, G. Jeong, W. Choi, Journal of Power Sources 170 (2007) 456.

[28] W. Hertl, W.W. Pultz, Journal of the American Ceramic Society 50 (7) (1967) 378.

[29] C.-M. Park, W. Choi, Y. Hwa, J.-H. Kim, G. Jeong, H.-J. Sohn, Journal of Materials Chemistry 20 (2010) 4854.

[30] T. Kim, S. Park, S.M. Oh, Journal of the Electrochemical Society 154 (2) (2007) A1112.

국문 초록

고분자 전해질 막 연료 전지에서 산소 환원 반응의 비가역성에 기인한 높은 과전압은 전지 성능을 저해하는 요인으로 지적되고 있다. 산소 환원의 반응 속도를 높이기 위해 일련의 무전해 도금법과 전류치환법을 사용하여 Pt_{shell}-Pd_{core}/C 전기화학 촉매를 제작하였다. 전도성 탄소에 담지된 Pd촉매 표면에 Cu 중간층을 형성하기 위한 방법으로 Cu 무전해 도금을 선택하였으며, 이후 전착된 Cu를 Pt로 치환하였다. XRD, XPS와 같은 분광학 분석법을 사용하여 합성된 Pt_{shell}-Pd_{core}/C 촉매를 분석하였다. 유도 플라즈마 질량 분석을 이용하여 합성된 촉매는 7 wt%의 Pt과 15 wt%의 Pd을 포함하고 있는 것으로 나타났다. 고분해능 투과전자현미경과 고각환상암시야상 검출기 및 X선 분광 분석기가 연동된 주사투과전자현미경을 사용하여 Pd와 Pt의 코어-쉘 구조를 밝혀냈다. 3전극-셀 전기화학 실험을 통해 Pt_{shell}-Pd_{core}/C 촉매 표면에서 4전자 산소 환원 반응이 일어남을 확인하였고, 측정된 반응 전류는 Pt/C 촉매보다 큰 것으로 나타났다. 위와 같은 산소 환원 반응 속도의 향상은 Pt_{shell}-Pd_{core}/C 촉매의 Pt 표면층이 흡착물과 이루는 결합 특성과 밀접하게 관련되어 있다. Pt_{shell}-Pd_{core}/C의 Pt 표면층의 d-band의 상태밀도는 흡착물의 결합 시에 페르미 준위에 더 가까운 방향으로 옮겨지며 그 옮김 정도는 상용 Pt/C보다 더 크게 나타났다. XPS 분석을 통해 Pt_{shell}-Pd_{core}/C의 d-band 전자 밀도 평균 즉, ε_d이 상용 Pt/C보다 0.27 eV 큰 것으로 계산되었다. 높게 위치한 ε_d는 좀 덜 강한 OH흡착을 의미하며 결과적으로 이는 Pt 촉매 표면에서 Pt와 결합해 있는 산소 포함

물질(Pt-O)이 수소화되어 촉매 표면에서 쉽게 떨어져나갈 수 있음을 뜻한다. 덧붙여 촉매가 포함하고 있는 금속의 질량을 기준으로 표현된 활성도는 Pt_{shell}-Pd_{core}/C 촉매가 Pt/C에 비해서 5배 이상 높은 것으로 확인되었다. 무전해 도금을 사용한 촉매 합성법을 통해 소량의 Pt을 포함한 고분산 전기화학 촉매의 제작 촉매의 제작을 가능하였음을 알 수 있다.

고분자 전해질 막 연료 전지의 한 부류인 직접 메탄올 연료 전지에서는 CO_{ad} 피독에 저항성을 갖으며 안정적인 구동을 돕는 연료극 촉매의 제작이 요구되고 있다. 이러한 의미에서 합성한 Pt_{shell}-Pd_{core}/C 촉매를 메탄올 산화 반응에 적용하였다. Pt_{shell}-Pd_{core}/C와 상용 Pt/C촉매 모두 메탄올 산화 반응에 반응성을 나타냈으나, 반응 전압에 따라 서로 다른 거동을 보임을 확인하였다. 아레니우스 곡선으로부터 얻어진 겉보기 활성화 에너지 측정을 통해 Pt_{shell}-Pd_{core}/C와 상용 Pt/C 표면에서의 메탄올 산화 반응의 속도 특성을 비교하였다. 메탄올의 분해흡착이 일어나는 저전압 영역에서는 Pt_{shell}-Pd_{core}/C가 Pt/C보다 큰 겉보기 활성화 에너지를 갖는 것으로 나타났다. 이러한 결과는 Pt_{shell}-Pd_{core}/C가 상용 Pt/C보다 메탄올 분해 특성이 낮음을 의미한다. 반면, 고전압 영역에서는 Pt_{shell}-Pd_{core}/C의 겉보기 활성화 에너지가 상용 Pt/C보다 작은 것으로 계산되었다. 고전압 영역에서의 활성화 에너지의 감소는 수전해에 따른 OH_{ad}의 형성과 CO_{ad}과의 화합반응이 Pt_{shell}-Pd_{core}/C 표면 위에서 향상되었음을 의미한다. 이러한 OH_{ad} 형성 반응의 속도 증가는 메탄올 산화 반응에 더 큰 영향을 끼치는데, 이는 메탄올 산화 반응에 있어서의 속도 결정 단계가 메탄올의 흡착이 아닌 표면 흡착물의 산화 반응이기 때문이다. CO_{ad}-제거 실험을

통해 Pt_{shell}-Pd_{core}/C 촉매 표면 위에서 CO_{ad} 흡착물의 전기화학적 산화 반응을 확인하였다. 실험을 통해 Pt_{shell}-Pd_{core}/C 촉매 표면 위에서의 CO_{ad} 탈착 반응의 시작 전압이 Pt/C 촉매 보다 낮은 것으로 나타났으며, 이는 Pt_{shell}-Pd_{core}/C에서 수월하게 형성된 OH_{ad}에 의해 CO_{ad} 탈착 반응이 촉진되었음을 의미한다. 측정된 전류 밀도로부터 상용 Pt/C 촉매는 CO_{ad} 흡착에 취약하며, 따라서 Pt_{shell}-Pd_{core}/C 촉매에 비해 CO_{ad}에 의한 피독 및 촉매의 불활성화가 쉽게 진행된다는 것을 유추할 수 있다.

연료 전지 전기화학 촉매의 제작에 초음파 방법을 사용하였다. 초음파 주사를 통해 아무런 표면 처리 없이 실리카 표면 위에 Pt을 직접 전착시킬 수 있었다. 위의 방법으로 적은 크기 오차를 갖는 Pt 나노 입자를 형성할 수 있었다. 제작한 복합체를 전도성 탄소와 혼합하여 고분자 전해질 막 연료 전지의 연료극 촉매로 사용하였다. 상대습도를 변화시키며 단위 연료 전지 실험을 진행하였을 때, Pt-SiO_2/C 촉매를 사용한 막 전극 접합체가 수분이 부족한 조건에서도 안정적인 성능을 나타내는 것에 비해 상용 Pt/C를 사용한 막 전극 집합체의 경우, 상대습도가 감소함에 따라 성능이 급격히 감소하였다. 이는 Pt-SiO_2/C을 이용한 막 전극 집합체의 촉매층에 포함된 친수성 SiO_2이 낮은 습도 조건에서도 습도를 유지하는데 역할을 해주었기 때문이다.

주요어: Pt-based electro-catalyst, electroless deposition, ultrasound, silica, oxygen reduction, methanol electro-oxidation, low humidity

학번: 2009-30251

CURRICULUM VITAE

Insoo Choi

Electronics Processing Research Laboratory,
School of Chemical and Biological Engineering
Seoul National University, Seoul 151-744, Republic of Korea

Personal Information

Name: Insoo Choi
Phone: +82-2-880-8940

Gender: Male
Fax: +82-2-888-7295

Date of Birth: July 17, 1983
E-mail: summus7@snu.ac.kr

Place of Birth: Seoul, Republic of Korea
Nationality: Korean

Office: Room 907, Building 302, College of Engineering, Seoul National University,
599 Gwanangno, Gwanak-gu, Seoul 151 744, Republic of Korea

Education

Doctor of Philosophy (March 2009 ~ February 2013)
School of Chemical and Biological Engineering, Seoul National University
Advisor: Prof. Jae Jeong Kim

Master of Science (March 2007 ~ February 2009)
School of Chemical and Biological Engineering, Seoul National University
Advisor: Prof. Jae Jeong Kim

Bachelor of Science (March 2002 ~ February 2007)
School of Chemical and Biological Engineering, Seoul National University

Academic Activities

2007.3 ~ present Research Assistant for Prof. Jae Jeong Kim

2007.3 ~ 2007.6	Lecture Assistant: Physical Chemistry 1
2007.2	Elementary Education Program of Semiconductor Processing in Inter-university Semiconductor Research Center (ISRC)
2007.3 ~ present	Aligner operation (EV620, ISRC) (MA 6-II, ISRC)
2007.3 ~ present	Wafer bonder (EV501, ISRC)
2009.9 ~ present	Atomic Force Microscope (XE-150, Park Systems)
2012.6 ~ present	Transmission Electron Microscope (JEM-2100)

Professional Activities

2008.5 ~ 2009.4 & 2011.5 ~ 2012.4	Student Member, The Electrochemical Society, USA
2007.4 ~ present	Student Member, Korean Institute of Chemical Engineers
2008.4 ~ present	Student Member, The Korean Electrochemical Society

Accomplishment

- International Journal –

Published

1. Insoo Choi, Min Jeong Lee, Seung M. Oh, Jae Jeong Kim, "Fading Mechanisms of Carbon-coated and Disproportionated Si/SiO_x Negative Electrode (Si/SiO_x/C) in Li-ion Secondary Battery: Dynamics and Component Analysis by TEM", *Electrochimica Acta* 85, 369-376 (2012)
2. Sang Hyun Ahn, Seung Jun Hwang, Sung Jong Yoo, Insoo Choi, Hyoung-Juhn Kim, Jong Hyun Jang, Suk Woo Nam, Tae-Hoon Lim, Taeho Lim, Soo-Kil Kim, and Jae Jeong Kim, "Electrodeposited Ni dendrites with high activity and durability for hydrogen evolution reaction in alkaline water electrolysis", *J. Mater. Chem.* 22, 15153-15159 (2012)
3. Insoo Choi, Kyoung G. Lee, Sang Hyun Ahn, Do Hyun Kim, Oh Joong Kwon, Jae Jeong Kim, "Sonochemical synthesis of Pt-deposited SiO_2 nanocomposite and its catalytic application for polymer electrolyte membrane fuel cell under low humidity

conditions", *Catal. Commun.* 21, 86-90 (2012)

4. Sang Hyun Ahn, Insoo Choi, Oh Joong Kwon, Jae Jeong Kim, "One-step co-electrodeposition of Pt-Ru electrocatalysts on carbon paper for direct methanol fuel cell", *Chem. Eng. J*. 181-182, 276-280 (2012)
5. Sang Hyun Ahn, Insoo Choi, Oh Joong Kwon, Taeho Lim, Jae Jeong Kim, "Electrochemical preparation of Pt-based catalysts on carbon paper treated with Sn sensitization and Pd activation", *Int. J. Hydrogen Energ.* 37, 41-50 (2012)
6. Insoo Choi, Sang Hyun Ahn, Jae Jeong, Kim, Oh Joong Kwon, "Preparation of Pt_{shell}-Pd_{core} nanoparticles with electroless deposition of copper for polymer electrolyte membrane fuel cell", *Appl. Catal. B:Environ*. 102, 608-613 (2011)
7. Oh Joong Kwon, Moo Sung Kang, Sang Hyun Ahn, Insoo Choi, Kang Uk Lee, Jee Hoon Jeong, In-Su Han, Jae Chun Yang, Jae Jeong Kim, "Development of flow field design of polymer electrolyte membrane fuel cell using in-situ impedance spectroscopy", *Int. J. Hydrogen Energ.* 36(16), 9799-9804 (2011)
8. Sang Hyun Ahn, Oh Joong Kwon, Soo-Kil Kim, Insoo Choi, Jae Jeong Kim, "Electrochemical preparation of Pt-based ternary alloy catalyst for direct methanol fuel cell anode", *Int. J. Hydrogen Energ.* 35(24), 13309-13316 (2010)
9. Sang Hyun Ahn, Oh Joong Kwon, Insoo Choi, Jae Jeong Kim, "Synergetic effect of combined use of Cu–ZnO–Al_2O_3 and Pt–Al_2O_3 for the steam reforming of methanol", *Catal. Commun.* 10, 2018–2022 (2009)

In preparation

10. Insoo Choi, Sang Hyun Ahn, Oh Joong Kwon, Jae Jeong Kim, "Synthesis of active and stable Pt_{shell}-Pd_{core}/C catalyst for electro-oxidation of methanol" (2013)

Published Transactions

11. Sang Hyun Ahn, Insoo Choi, Oh Joong Kwon, Taeho Lim, and Jae Jeong Kim, "Electrochemical preparation of Pt-based catalyst on carbon paper treated by Sn sensitization and Pd activation", ECS transaction, 41(1), 1105-1108 (2011)
12. Insoo Choi, Taeho Lim, Sang Hyun Ahn, Oh Joong Kwon, Jae Jeong Kim, "Synthesis of Pt-based electrocatalysts with core-shell structure through electrochemical reduction for oxygen reduction in PEMFC", ECS transaction, 41(1), 1051-1054 (2011)
13. Oh Joong Kwon, Sang Hyun Ahn, Insoo Choi, and Jae Jeong Kim, "The

characterization of Co-Ru-Pt ternary catalyst prepared by electrochemical process", ECS transaction 25(1), 1315-1318 (2009)

14. Insoo Choi, Oh Joong Kwon, and Jae Jeong Kim, "Preparation of Pt_{shell}-Pd_{core} catalyst and its application for polymer membrane fuel cell", ECS transaction, 16(2) 1105-1110 (2008)

- Conference –

Domestic

1. Insoo Choi, Jae Jeong Kim, "Fading mechanisms of carbon-coated and disproportionated Si/SiO_x anode (Si/SiO_x/C) in Li-ion secondary battery" (poster presentation), *2012 Green Technology Forum*, 2012
2. Jae Seung Yoo, Insoo Choi, Jae Jeong Kim, Oh Joong Kwon, "Rational synthesis of Pt shell from nano-sized SiO2 template and its catalytic activity for oxygen reduction reaction" (poster presentation), *The Korean Electrochemical Society spring meeting*, 2012
3. Insoo Choi, Min Jeong, Lee, Jae Jeong, Kim, "Fading mechanisms of carbon-coated and disproportionated Si/SiO_x anode (Si/SiO_x/C) in Li-ion secondary battery" (poster presentation), *The Korean Electrochemical Society spring meeting*, 2012 **(designated as an excellent poster)**
4. Sang Hyun Ahn, Seung Jun Hwang, Insoo Choi, Sung Jong Yoo, Hyung Jun Kim, Tae Hoon Lim, Soo-Kil, Kim, Jae Jeong Kim, "Morphological effect of electrdeposited Ni catalyst for hydrogen production by water electrolysis" (poster presentation), *The Korean Electrochemical Society fall meeting*, 2011 **(designated as an excellent poster)**
5. Sang Hyun Ahn, Seung Jun Hwang, Sung Jong Yoo, Insoo Choi, Hyung Jun Kim, Seok Woo Nam, Tae Hoon Lim, Soo-Kil Kim, Jae Jeong Kim, "Electrodeposited Ni Dendrites with High Activity and Durability for Hydrogen Evolution Reaction in Alkaline Water Electrolysis" (poster presentation), *Fuel Cells Symposium*, 2011
6. Sang Hyun Ahn, Insoo Choi, Oh Joong Kwon, Taeho Lim, Jae Jeong Kim, "The electrochemical preparation of Pt-based catalyst on carbon paper treated by Sn sensitization and Pd activation" (oral presentation), *The Korean Institute of Chemical Engineers fall meeting*, 2011

7. Insoo Choi, Sang Hyun Ahn, Oh Joong Kwon, Jae Jeong Kim, “Preparation of Pt-based electrocatalysts via electrochemical or sonochemical reduction process for polymer electrolyte membrane fuel cell” (oral presentation), *The Korean Institute of Chemical Engineers fall meeting*, 2011
8. Insoo Choi, Sang Hyun Ahn, Oh Joong Kwon, Jae Jeong Kim, “Preparation of Pt_{shell}-Pd_{core} catalyst with electroless deposition of Cu for oxygen reduction reaction in PEMFC” (oral presentation), *The Korean Electrochemical Society spring meeting*, 2011
9. Sang Hyun Ahn, Insoo Choi, Oh Joong Kwon, Kang Uk Lee, Jae Jeong, Kim, “Development of a silicon-based compact fuel processor for liquefied natural gas (LNG)” (oral presentation), *The Korea Society For Energy Engineering fall meeting*, 2010
10. Insoo Choi, Ji Yoon Kwon, Seung Mo Oh, Jae Jeong Kim, “The study on surface chemistry of Si thin-film anode for Li-ion secondary battery with FEC involved as a co-solvent” (poster presentation), *The Korean Electrochemical Society spring meeting*, 2010
11. Insoo Choi, Oh Joong Kwon, Jae Jeong, Kim, “Preparation of Pt_{shell}-Pd_{core}/C nanoparticle and its application for polymer electrolyte membrane fuel cell” (oral presentation), *Korean Institute of Chemical Engineers fall meeting*, 2009
12. Sang Hyun Ahn, Oh Joong Kwon, Soo-Kil Kim, Insoo Choi, Jae Jeong Kim, “The electrochemical preparation of CoPtRu catalyst having enhanced carbon monoxide tolerance” (oral presentation), *Korean Institute of Chemical Engineers fall meeting*, 2009
13. Insoo Choi, Oh Joong Kwon, Jae Jeong Kim, “Preparation of Pt_{shell}-Pd_{core} nanoparticle and its application for oxygen reduction reaction” (poster presentation), *Korean Institute of Chemical Engineers spring meeting*, 2008 **(designated as an excellent poster)**

International

14. Soo-Kil Kim, Sang Hyun Ahn, Insoo Choi, Seung Jun Hwang, Hyoung-Juhn Kim, Jae Jeong Kim, Tae-Hoon Lim, Taeho Lim, Suk Woo Nam, Sung Jong Yoo, “High activity Ni dendrite catalysts for alkaline water electrolysis prepared by electrodeposition”

(poster presentation), *10th Spring meeting of ISE*, Perth, Australia, 17th April, 2012

15. Taeho Lim, Kwang Hwan Kim, Insoo Choi, Jae Jeong Kim, Oh Joong Kwon, "Direct Cu electrodeposition on Ta substrate" (poster presentation), *IUMRS-ICA*, 2012
16. Man Su Kim, Insoo Choi, Jae Jeong Kim, Jae Seung Yoo, Oh Joong Kwon, "Synthesis of carbon-supported Pt@Pd catalyst by adopting chemical reduction method on highly-dispersed Pd colloid" (poster presentation), *International Conference on Advanced Electromaterials*, 2011 **(designated as an excellent poster)**
17. Sang Hyun Ahn, Insoo Choi, Oh Joong Kwon, Taeho Lim, Jae Jeong Kim, "Electrochemical preparation of Pt-based catalyst on carbon paper treated by Sn sensitization and Pd activation" (oral presentation), The *220th* Meeting of ECS, 2011
18. Insoo Choi, Taeho Lim, Sang Hyun Ahn, Oh Joong Kwon, Jae Jeong Kim, "Synthesis of Pt-based electrocatalysts with core-shell structure through electrochemical reduction for oxygen reduction in PEMFC" (oral presentation), *The 220th Meeting of ECS*, 2011
19. Oh Joong Kwon, Sang Hyun Ahn, Insoo Choi, Jae Jeong Kim, "The characterization of Pt-Ru-Co ternary catalyst prepared by electrochemical process" (oral presentation), *216th Meeting of ECS*, 2009
20. Insoo Choi, Oh Joong Kwon and Jae Jeong Kim, "Preparation of Pt_{shell}-Pd_{core} of catalysts and its application for polymer electrolyte membrane fuel cell" (oral presentation), *214th Meeting of ECS*, 2008
21. Insoo Choi, Oh Joong Kwon and Jae Jeong Kim, "Preparation of Pt_{shell}-Pd_{core} of catalyst and its application for oxygen reduction reaction" (poster presentation), *The 3rd annual Korea-USA joint symposium on hydrogen & fuel cell technologies*, 2008

- Collaboration with Industries –

1. The study on the solid electrolyte interface of Si-embedded anode in Li-ion secondary battery (Samsung SDI, 2009.2 ~2011.7)

- Honors and Awards –

1. Full scholarship from Song-Won Scholarship Foundation, 2002.3 ~ 2009.2
2. A letter of appreciation awarded by *Un-Chan Chung, the president of Seoul National University*, 2006

3. Award for excellent poster presentation in energy & environment, *Korean Institute of Chemical Engineers, in spring meeting*, 2008
4. Award for excellent poster presentation, *Research Center for Energy Conversion and Storage workshop*, 2008
5. Award for excellent poster presentation in batteries, *The Korean Electrochemical Society, in spring meeting*, 2012

- Certificates –

1. The certificate of ISRC
2. Test of English Proficiency developed by Seoul National University (TEPS)
3. Oral Proficiency Interview-Computer (OPIC)